이학박사학위논문

Microscale Flow, Gas-Phase Chemistry, and Dispersion in Urban Areas

도시 지역의 미규모 흐름, 기체상 화학 및 분산

2014년 8월

서울대학교 대학원

지구환경과학부

곽 경 환

Microscale Flow, Gas-Phase Chemistry, and Dispersion in Urban Areas

도시 지역의 미규모 흐름, 기체상 화학 및 분산

지도교수 백 종 진

이 논문을 이학박사 학위논문으로 제출함

2014년 4월

서울대학교 대학원

지구환경과학부

곽 경 환

곽경환의 이학박사 학위논문을 인준함

2014년 6월

위 원 장 _____ (인)

부 위원장 _____ (인)

위 원 _____ (인)

위 원 _____ (인)

위 원 _____ (인)

Microscale Flow, Gas-Phase Chemistry, and Dispersion in Urban Areas

By
Kyung-Hwan Kwak

A Dissertation Submitted to the Faculty of the Graduate School of Seoul National University in Partial Fulfillment of the Requirements for the Degree of Doctor of Philosophy

August 2014

Advisory Committee:
Professor Rokjin J. Park, Chair
Professor Jong-Jin Baik, Advisor
Professor Soontae Kim
Doctor Young-San Park
Professor Do-Yong Kim

Abstract

Flow, gas-phase chemistry, and dispersion in urban areas are predominantly microscale, which are directly modulated by artificial topography and land cover at surfaces. Because these features are connected to each other, an investigation in a single framework is necessary. This study develops a computational fluid dynamics (CFD) model coupled with essential physical and chemical components. At first, an urban surface and radiation model are incorporated into the CFD model to investigate the diurnal variation of flow in a street canyon with an aspect ratio of 1. In one-day simulations with various ambient wind speeds, two flow regimes are identified by vortex configuration in a street canyon. Flow regime I is characterized by a primary vortex, and flow regime II is characterized by two counter-rotating vortices. For weak ambient winds, the dependency of surface sensible heat flux on the ambient wind speed is found to play an essential role in determining the relationship between canyon wind speed and ambient wind speed. Secondly, the carbon bond mechanism Ⅳ (CBM–Ⅳ) is included in the CFD model to investigate reactive pollutant dispersion in and above a street canyon with an aspect ratio of 1. In simulations with 14 emission scenarios, dispersion types are classified into NO-type, NO_2-type, and O_3-type dispersion. The VOC-to-NO_x emission ratio is found to be an

important factor in determining the transition of dispersion type. In this transition process, OH plays a key role through a radical chain including HO_2, RO, and RO_2. The examination of O_3 sensitivity shows that the O_3 concentration is negatively correlated with the NO_x emission level and weakly correlated with the VOC emission level. Therefore, the street canyon is a negatively NO_x-sensitive regime. In a street canyon with a canyon aspect ratio of 2, there is a contrast between different regions in the street canyon, showing O_3 chemical production in an upper region and O_3 chemical loss in a lower region. Thirdly, the urban surface and radiation model along with the CBM–Ⅳ are incorporated into the CFD model to investigate the diurnal variation of NO_x and O_3 exchange between a street canyon and the overlying air. The temporal and spatial distribution of NO_x removal and O_3 entrainment across the roof level of street canyon totally depends on flow regime. While the turbulent process is generally the dominant mechanism of NO_x removal and O_3 entrainment, the mean process can be responsible for the mechanism when the upwind building wall is strongly heated in the afternoon. The calculated NO_x and O_3 exchange velocities depends not only on flow regime but also photochemistry. Finally, urban air quality simulations using the CFD model coupled with mesoscale meteorological (WRF) and chemistry-transport (CMAQ) models are performed in a high-rise building area. The simulated NO_2 and O_3 concentrations are evaluated with data measured

at a roadside air quality monitoring station, showing significant improvements compared to those in the CMAQ simulation. The large spatial variabilities of the NO_2 and O_3 concentrations in the high-rise building area are attributed to the heterogeneities of building geometry and mobile emission. As a consequence, the integrated urban air quality modeling system is a leading-edge numerical approach that embraces multiscale influences on air quality in urban areas.

Keywords: reactive pollutant dispersion, NO_x-VOC-O_3 chemistry, computational fluid dynamics model, urban area, street canyon, pollutant emission

Student Number: 2007-20376

Contents

List of Figures

List of Tables

1 Introduction

1.1 Review of previous studies

1.1.1 Microscale flow in urban areas

As the number of people living in urban areas increases, nature of urban surface and urban boundary layer continuously changes. Changes in topographical factors mainly due to building construction and thermal factors due to land surface covered by artificial matters largely affect flow characteristics in urban areas. Phenomena affected by these kinds of factors usually have relatively small scales. A term, microscale, represents horizontal scales smaller than about 3 km and time scales shorter than about 1 hour, vertically covering urban canopy layer and overlying atmosphere (i.e., doubled building height) in urban areas (Stull, 1988; Grimmond, 2006).

An urban street canyon that is comprised of two buildings and a street between them is a basic geometry in urban areas. Many researches have studied microscale flow characteristics in urban street canyons. Oke (1988) classified flow patterns into three regimes that are isolated roughness, wake interference, and skimming flow regimes in a street canyon based on a canyon aspect ratio

(H/W; H is the building height and W is the street width). In addition to canyon aspect ratio, other important factors such as building configuration and ambient wind speed and direction have been considered for computational fluid dynamics (CFD) model simulations to investigate street canyon flow under isothermal conditions (Li et al., 2006 and its references).

Recently, more attention has been paid to the impact of thermal forcing on street canyon flow. Field measurements (Nakamura and Oke 1988; Louka et al. 2002; Eliasson et al. 2006; Offerle et al. 2007; Idczak et al. 2007), laboratory experiments (Uehara et al. 2000; Kovar-Panskus et al. 2002), and two-dimensional numerical experiments (Sini et al. 1996; Kim and Baik 1999, 2001; Xie et al. 2005; Cheng et al. 2009) were performed to examine the effects of solar heating on street canyon flow. Sini et al. (1996) found that when H/W is 0.89, the downwind building-wall heating divides a primary vortex into two counter-rotating vortices, whereas the ground or the upwind building-wall heating enhances vortex circulation in a street canyon. Kim and Baik (1999) demonstrated that two or three vortices can be formed in a street canyon depending on the differential surface heating (no heating, upwind building-wall heating, street-canyon bottom heating, and downwind building-wall heating) and canyon aspect ratio. Kim and Baik (2001) classified street canyon flow into five flow regimes in terms of canyon aspect ratio and the degree of street-canyon

bottom heating. Kovar-Panskus et al. (2002) performed a wind-tunnel study with $H/W = 1$ to examine how the windward-facing wall heating changes the in-canyon flow pattern. The study showed that as the Froude number (Fr) decreases below 1, a primary vortex weakens and relatively stagnant flow appears in a lower region. Xie et al. (2005) quantified the relative contributions of mechanical and thermal forcings to flow features in the case with $H/W = 1$ using Gr/Re^2, where Gr is the Grashof number and Re is the Reynolds number. Numerical experiments have shown that when the bottom surface is heated, the street canyon flow pattern in three dimensions is different from that in two dimensions (Tsai et al. 2005; Baik et al. 2007; Kang et al. 2008). In three dimensions, a primary vortex in a street canyon meanders in the along-canyon direction as well as in the cross-canyon direction. In most numerical studies, the surface heating, which was represented by a temperature difference between surfaces and adjacent air, was prescribed as a constant value with time. A few studies incorporated radiation and heat transfer processes into numerical models to examine steady-state flow in the vicinity of buildings (Chen et al. 2004; Hadavand et al. 2008).

1.1.2 Microscale dispersion in urban areas

Air pollution in urban areas is a serious environmental problem. Particularly, urban dwellers living in buildings, commuting by car on streets, and walking on sidewalks breathe the air where pollutant sources (i.e., vehicle) are closely located at. Therefore, microscale dispersion is an important issue to know the effects of pollutant emitted from vehicles on health.

Several intensive field campaigns such as Joint Urban 2003 in Oklahoma City, USA and DAPPLE (Dispersion of air pollution and its penetration into the local environment) project in London, UK have been conducted (Allwine et al., 2004; Arnold et al., 2004). These measurement data have been analyzed and used to compare with wind-tunnel results (Klein et al., 2011; Carpentieri et al., 2012) and numerical model results (Flaherty et al., 2007; Hanna and Baja, 2009; Xie and Castro, 2009).

Dispersion characteristics in an urban street canyon have been investigated using CFD models (Vardoulakis et al., 2003 and its references). Similar to flow characteristics, canyon aspect ratio (Baik and Kim, 1999; Cai et al, 2008; Cheng et al., 2008), building configuration (Yassin et al., 2008; Huang et al., 2009), wind speed (Huang et al., 2000; Chan et al., 2002) and direction (Kim and Baik, 2004) are intensively investigated as crucial factors affecting dispersion characteristics in street canyons.

In Reynolds-averaged Navier–Stokes equations (RANS) model simulation under isothermal conditions, pollutant removal at the roof level occurs by means of turbulent flux rather than mean flux, which is dependent on inflow turbulent kinetic energy, wind speed, and canyon aspect ratio (Baik and Kim, 2002). Other numerical studies using large-eddy simulations (LES) model that can reproduce unsteady and intermittent flows also calculated pollutant exchange rates at the roof level (Liu et al., 2005; Cheng et al., 2008). Cheng et al. (2008) compared LES model results with RANS model results and concluded that two model results are similar to each other on average.

Thermal forcing due to solar heating on urban surfaces modifies dispersion characteristics as well as flow characteristics in street canyons. Modified flow patterns change pollutant concentrations. Heating on an upwind building wall or a street bottom decreases pollutant concentration, whereas heating on a downwind building wall increases pollutant concentration (Sini et al., 1996). As the heating intensity increases, pollutant removal by means of mean flux becomes dominant compared to that by means of turbulent flux, resulting in decrease of pollutant concentration (Kang et al., 2008; Cheng et al., 2009).

1.1.3 Microscale gas-phase chemistry in urban areas

Atmospheric pollutants in urban areas are emitted from various types of sources and transported by urban flows. Simultaneously, primary pollutants are chemically reacted with other species such as hydroxyl radicals (OH), hydroperoxy radicals (HO_2), organic peroxy radicals (RO_2), and ozone (O_3) in the atmosphere. Not only primary pollutants such as NO_x ($NO + NO_2$) and volatile organic compounds (VOCs) from mobile sources but also secondary pollutants such as O_3 cause public health problems for urban dwellers.

There are a few numerical modeling studies that consider several chemical reactions to investigate the dispersion of reactive pollutants near a vehicular exhaust tailpipe (Chan et al., 2001) and in street canyons (Baker et al., 2004; Baik et al., 2007; Grawe et al., 2007; Kang et al., 2008). An investigation of NO_x dispersion using the Monte Carlo method showed that the oxidation reduction of NO and thus the formation and accumulation of NO_2 in a vehicular exhaust plume are important at the initial dispersion process near a tailpipe (Chan et al., 2001). Baker et al. (2004) examined the dispersion of NO, NO_2, and O_3 in a street canyon using a LES model that includes simple photochemistry among the reactive pollutants. Baik et al. (2007) developed a RANS model coupled with the simple photochemistry of $NO–NO_2–O_3$ and used this model to examine the temperature-dependent dispersion of the reactive pollutants in a street canyon. Baker et al. (2004) and Baik et al. (2007) found that a chemically

unstable region exists near the roof level. The dispersion of reactive pollutants in a street canyon is known to be affected by shadowing (Grawe et al., 2007) and surface heating (Kang et al., 2008).

In addition to the simple photochemistry, some VOCs and their reactions have recently been included in numerical models used to calculate the concentrations of various reactive pollutants in street canyons (Liu and Leung, 2008; Garmory et al., 2009). Liu and Leung (2008) examined O_3 formation in street canyons using a chemistry box model. Using the field Monte Carlo method, Garmory et al. (2009) showed that some radical species in the carbon bond mechanism Ⅳ (CBM–Ⅳ) deviate significantly from the chemical equilibrium at the roof-top level.

1.2 Numerical models

1.2.1 Computational fluid dynamics (CFD) model

The CFD model used in this study is the RANS model with the renormalization group (RNG) k–ε turbulence closure scheme (Kim and Baik, 2004; Baik et al., 2007). The governing equations are the momentum equation, the mass continuity equation, the thermodynamic energy equation, the transport

equation for passive scalar, and the equations of turbulent kinetic energy and its dissipation rate.

$$\frac{\partial U_i}{\partial t} + U_j \frac{\partial U_i}{\partial x_j} = -\frac{1}{\rho_0}\frac{\partial P^*}{\partial x_i} + \delta_{i3} g \frac{T^*}{T_0} + \nu \frac{\partial^2 U_i}{\partial x_j \partial x_j} - \frac{\partial}{\partial x_j}(\overline{u_i u_j}) \tag{1.1}$$

$$\frac{\partial U_j}{\partial x_j} = 0 \tag{1.2}$$

$$\frac{\partial T}{\partial t} + U_j \frac{\partial T}{\partial x_j} = \kappa \frac{\partial^2 T}{\partial x_j \partial x_j} - \frac{\partial}{\partial x_j}(\overline{T' u_j}) + S_{\mathrm{h}} \tag{1.3}$$

$$\frac{\partial C}{\partial t} + U_j \frac{\partial C}{\partial x_j} = D \frac{\partial^2 C}{\partial x_j \partial x_j} - \frac{\partial}{\partial x_j}(\overline{c u_j}) + S_{\mathrm{c}} \tag{1.4}$$

$$\frac{\partial k}{\partial t} + U_j \frac{\partial k}{\partial x_j} = -\overline{u_i u_j}\frac{\partial U_i}{\partial x_j} + \frac{\delta_{3j} g}{T_0}\overline{T' u_j} + \frac{\partial}{\partial x_j}\left(\frac{K_{\mathrm{m}}}{\sigma_k}\frac{\partial k}{\partial x_j}\right) - \varepsilon \tag{1.5}$$

$$\frac{\partial \varepsilon}{\partial t} + U_j \frac{\partial \varepsilon}{\partial x_j} = -C_{\varepsilon 1}\frac{\varepsilon}{k}\overline{u_i u_j}\frac{\partial U_i}{\partial x_j} + C_{\varepsilon 1}\frac{\varepsilon}{k}\frac{\delta_{3j} g}{T_0}\overline{T' u_j} + \frac{\partial}{\partial x_j}\left(\frac{K_{\mathrm{m}}}{\sigma_\varepsilon}\frac{\partial \varepsilon}{\partial x_j}\right) - C_{\varepsilon 2}\frac{\varepsilon^2}{k} - R \tag{1.6}$$

where U_i is the ith mean velocity component, T the mean temperature, C the mean concentration of scalar, k the turbulent kinetic energy, ε the dissipation rate of turbulent kinetic energy, u_i the fluctuation from U_i, T' the fluctuation from T, P^* the deviation of pressure from its reference value, T^* the deviation of

temperature from its reference value ($= T - T_0$), ρ_0 the air density, δ_{ij} the Kronecker delta, g the gravitational acceleration, ν the kinematic viscosity of air, D the molecular diffusivity of scalar, K_m the eddy viscosity of momentum and κ the thermal diffusivity of air. S_h and S_c denote the source or sink terms of heat and scalar. The parameterizations of Reynolds stress and turbulent heat flux, the expressions of K_m and R, and the empirical constants in the RNG k–ε turbulence closure scheme are given in the references cited above.

1.3 Objectives of this study

The fundamental aim of this study is to understand microscale flow, gas-phase chemistry, and dispersion in urban areas by means of numerical modeling. The first stage is a development of CFD model that includes an urban surface and radiation model. The urban surface and radiation model that is a part of an urban canopy model is used to calculate the surface temperatures of roof, walls, and road prognostically. Using the developed CFD model, the diurnal variation of street canyon flow is investigated (Section 2 and 3).

The next stage is coupling a CFD model with a complex chemical mechanism. The CBM–Ⅳ is selected as a complex chemical mechanism at this

stage. The CBM–Ⅳ that includes both NO_x and VOC chemistry is useful for studying not only mesoscale regional chemistry but also microscale urban chemistry (Kim et al., 2008; Garmory et al., 2009). Using the CFD model coupled with CBM–Ⅳ, reactive pollutant dispersion in and above a street canyon is examined. In addition to dispersion types, the O_3 sensitivity to the NO_x and VOC emission levels is also examined (Section 4 and 5). As an extension of study, the reactive pollutant dispersion is examined in a street canyon with different aspect ratios. In the deep street canyon, O_3 chemical characteristics that sensitive to these environmental conditions in the lower and upper regions of the street canyon are analyzed (Section 6). Also, the coupled model along with the urban surface and radiation model can simulate diurnal variation of reactive pollutants in a street canyon. Incorporating these components into the CFD model, the NO_x removal and O_3 entrainment mechanisms are investigated (Section 7).

Finally, we address the above issues in a real urban area. To extend a study area from an idealized street canyon to a real urban area, an integrated urban air quality modeling system coupling the CFD model with both mesoscale meteorological and chemistry-transport models is developed. Using the simulation results in a real urban area, local influences of urban surface characteristics on urban air quality are discussed (Section 8).

2 Two-Way Coupling Urban Surface and Radiation Model with CFD Model

2.1 Urban surface and radiation model

For this study, the urban surface and radiation model that is a part of the urban canopy model developed by Ryu et al. (2011) is incorporated into the CFD model developed by Kim and Baik (2004) and Baik et al. (2007). Surface and substrate temperatures are obtained by the heat diffusion equation and the heat conduction equation, which are expressed as

$$C_i \frac{\partial T_i}{\partial t} = -\frac{\partial F_i}{\partial z_p}, \tag{2.1}$$

$$F_i = -k_i \frac{\partial T_i}{\partial z_p}, \tag{2.2}$$

where T_i is the temperature, F_i is the conductive heat flux, C_i is the volumetric heat capacity, k_i is the thermal conductivity, and z_p is the coordinate in the direction perpendicular to the surface. The subscript *i* indicates each surface.

The surface boundary condition of Eq. 2.1 is given by surface energy balance equation, which is expressed as

$$F_i = S_i^{\uparrow\downarrow} + L_i^{\uparrow\downarrow} - H_i, \tag{2.3}$$

where $S_i^{\uparrow\downarrow}$, $L_i^{\uparrow\downarrow}$, and H_i are the net shortwave radiation, the net longwave radiation, and the sensible heat flux for each surface *i*, respectively. For given time (in local standard time, LST) and location (in longitude and latitude), the direct (S_{dir}) and diffuse (S_{diff}) components of downward shortwave radiation at the reference height are estimated following the method of Panão et al. (2007)

$$S_{\text{dir}} = K_{\perp} \cos\phi_z, \tag{2.4}$$

$$S_{\text{diff}} = G - S_{\text{dir}}, \tag{2.5}$$

where $K_{\perp}$ and G are the normal and global direct irradiances, respectively. Here, the solar zenith angle ϕ_z is used to quantify S_{dir} and G. Downward longwave radiation (L_{atm}) is estimated following the methods of Swinbank (1963) and Lee and Park (2008)

$$L_{\text{atm}} = 9.4 \times 10^{-6} \sigma T_{\text{atm}}{}^{6}, \tag{2.6}$$

where σ is the Stefan-Boltzmann constant. Note that L_{atm} in Eq. 2.6 is only a function of the atmospheric temperature (T_{atm}).

Sky radiation consists of direct and diffuse shortwave radiation and longwave radiation. A method of partitioning the sky radiation into net shortwave/longwave radiation at each surface is the same as that of Ryu et al. (2011). Unlike diffuse shortwave radiation and longwave radiation that are isotropic, direct shortwave radiation has a single direction, differentiating a sunlit surface from a shaded surface. In definition, a sunlit surface receives non-zero direct shortwave radiation somewhere at the surface, whereas a shaded surface receives no direct shortwave radiation anywhere at the surface. A sunlit surface in a street canyon is determined by solar azimuth angle, canyon orientation, solar zenith angle, and canyon aspect ratio. Radiation incident into the canyon is

allowed to reflect upon the walls and road three times for shortwave radiation and one time for longwave radiation. The final reflected radiation is totally absorbed by each surface to conserve total radiative energy.

2.2 Treatment of sensible heat flux

Following the method of Versteeg and Malalasekera (1995), surface sensible heat flux (h_i) at a grid point is calculated using the wall function in the CFD model

$$h_i = -\rho C_p C_\mu^{\frac{1}{4}} k_a^{\frac{1}{2}} \frac{T_a - T_i}{T^+}, \tag{2.7}$$

where ρ is the air density, C_p is the specific heat of air at constant pressure, k_a and T_a are the turbulent kinetic energy and the air temperature at the nearest grid point to the surface, respectively, and T^+ is the universal temperature distribution for near-surface turbulent flows. C_μ (= 0.0845) is a constant. The universal temperature distribution requires roughness length parameters. Harman and Belcher (2006) suggested that the roughness length parameter for momentum is 10 times larger than that for heat. Following their suggestion, we

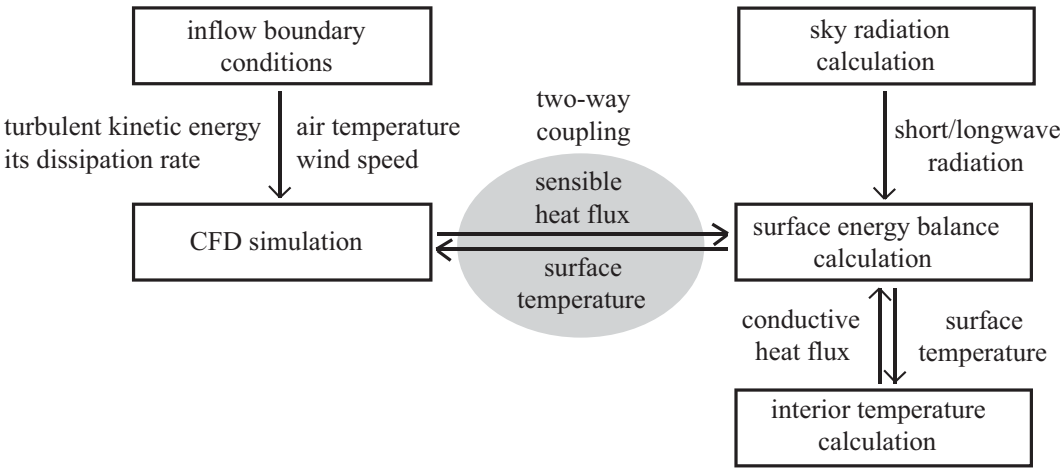

Figure 2.1. Flow chart of two-way coupling between the urban surface and radiation model and the CFD model.

use 0.05 m and 0.005 m as roughness length values for momentum and heat, respectively

2.3 Coupling strategy

Figure 2.1 shows the flow chart of two-way coupling between the urban surface and radiation model and the CFD model. The urban surface and radiation model predicts surface and substrate temperatures of roof, walls, and road. The predicted surface temperatures are used as a thermal boundary condition for the CFD model. The CFD model calculates sensible heat fluxes from the roof, walls, and road using a wall function. Since the surface temperature and sensible heat flux are regarded as representative values for a surface in the surface energy balance equation, sensible heat fluxes calculated at individual grid points in the CFD model are averaged over the surface.

2.4 Validation

The RANS model was validated using the wind-tunnel experiment dataset (Baik et al. 2007). Another part of the coupled CFD model, the urban surface and radiation model, is validated using the field measurement dataset from Guerville, France (1.44°E, 48.56°N) on 28 July 2004 (Idczak et al. 2007;

Idczak et al. 2010). The 1:5 scale street canyon has an aspect ratio of 2.48 with a width of 2.1 m and a NE-SW orientation (54° from due north). Observed shortwave radiation, longwave radiation, and ambient air temperature are used as meteorological forcings for the CFD model. Wind speed and direction at the inflow boundary are set to 2 m s^{-1} and south-easterly (75° from the canyon axis), respectively, which are similar to those measured at the top of a 10 m mast in the daytime. The values of physical properties of surface materials from Idczak et al. (2010) are used.

Figure 2.2 shows the simulated and observed surface temperatures of the northern wall, southern wall, and ground for the day. The CFD model well simulates two peaks of the surface temperatures of two opposite walls; a primary peak is caused by direct shortwave radiation and a secondary peak is caused by reflected shortwave radiation from the opposite wall. The wall temperatures are slightly underestimated, whereas the ground temperature is overestimated in the late afternoon. The maximum difference between the observed and simulated surface temperatures are 2.3°C (1610 LST) at the northern wall, 4.5°C (1140 LST) at the southern wall, and 3.2°C (1740 LST) at the ground. In general, however, the diurnal variations of simulated surface temperatures are in good agreement with those of observed ones. This indicates that the urban surface and radiation model is appropriate to be coupled with the RANS model for an

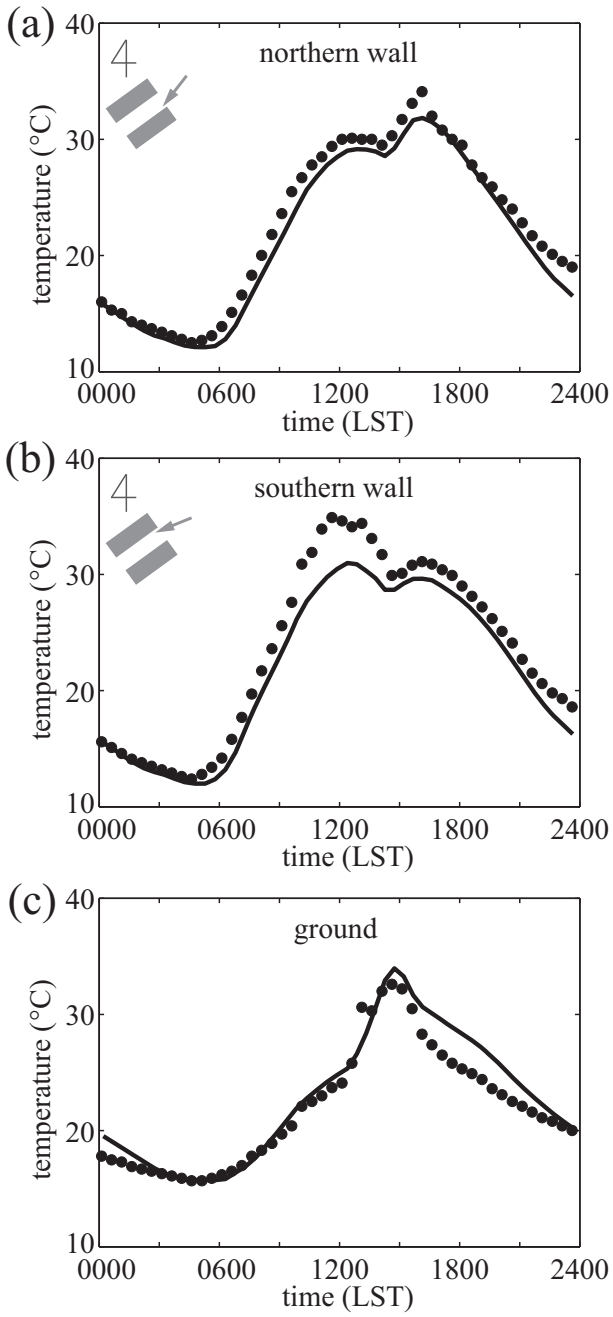

Figure 2.2. Diurnal variations of observed (mark) and simulated (line) surface temperatures of (a) northern wall, (b) southern wall, and (c) ground.

investigation of the diurnal variation of street canyon flow with realistically varying surface temperatures.

Surface temperature directly interacts with surface sensible heat flux that is calculated using a wall function in the CFD model. In Eq. 2.7, T_a and T^+ are associated with an interval of grid nearest to a surface. To test whether the grid intervals of 0.3 m in this section and 0.5 m in section 4 are reasonable choices, we performed simulations with different grid intervals and compared simulated surface temperatures to observed ones in the 1:5 scale street canyon. In these simulations, the interval of grid nearest to a surface is varied with 0.05, 0.1, 0.15, 0.2, 0.3, 0.5, 0.7, 0.9, and 1.0 m while other grid intervals in a computational domain are the same as those in the validation case. It was found that simulated surface temperatures (also simulated sensible heat fluxes) with the grid intervals of 0.15, 0.2, 0.3, 0.5, 0.7, and 0.9 m are very similar one another and well matched with observed ones. Therefore, it is appropriate to use a wall function with the grid intervals of 0.3 m and 0.5 m for calculating surface temperature and sensible heat flux.

3 Diurnal Variation of Street Canyon Flow

3.1 Experimental setup

Figure 3.1 depicts the computational domain and building configuration. Buildings and a street canyon are aligned in the *y*-direction (north-south direction) and infinitely long. Both the building height and street canyon width are 20 m, giving a canyon aspect ratio of 1. The domain size is 40 m in the *x*-direction (east-west direction), 50 m in the *y*-direction, and 60.1 m in the *z*-direction. The grid interval is 0.5 m in the *x*-direction and 1 m in the *y*-direction. In the vertical, the grid interval is 0.5 m up to z = 32 m and then gradually increases with an expansion ratio of 1.1. The CFD model is integrated for 24 h with a time step of 0.1 s. The easterly ambient (inflow) wind blows perpendicular to the along-canyon direction above the roof level. The ambient wind speed (U_{amb}) is constant with height, and five different ambient wind speeds of 2, 3, 4, 5, and 6 m s^{-1} are considered. Cyclic boundary conditions are applied at the spanwise boundaries (*y*-direction). Zero gradient boundary conditions are applied at the outflow and upper boundaries. Four surfaces (roof, upwind building wall, downwind building wall, and road) have their own thermal properties: surface albedos and emissivities, thermal conductivities, and

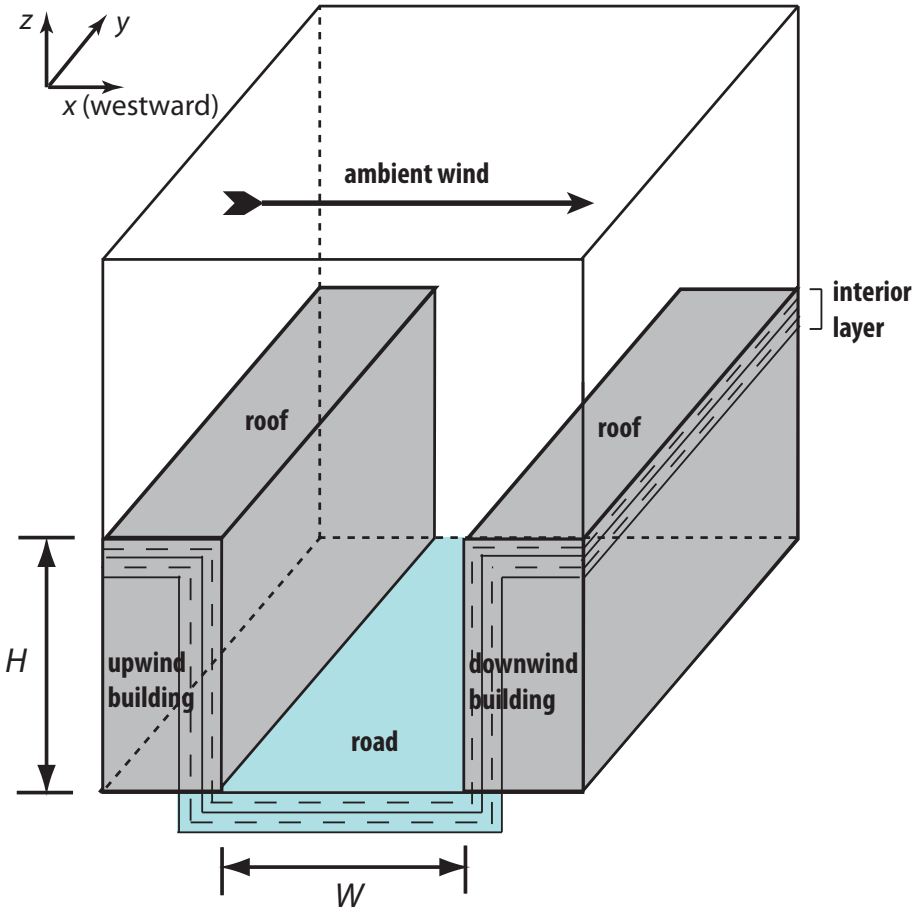

Figure 3.1. Computational domain and building configuration. *H* is the building height and *W* is the street canyon width. Positive in *x*-axis is westward.

heat capacities following those of the Marseille case summarised by Lee and Park (2008). The substrate of roof, walls, and road is comprised of 20 layers has a depth of 0.4 m. At the bottom of the innermost layer, a zero-flux boundary condition is applied. A 24-h spin-up time is allowed to obtain substrate temperatures that are used as initial conditions.

One-day simulations are performed for 18 June 2007 in Seoul, Korea. That day was clear and hot. The hourly air temperatures observed at the Korea Meteorological Observatory (126.97°E, 37.55°N) are used as ambient (inflow) air temperatures with a time interpolation. The observation showed a maximum air temperature of 32.7°C at 1500 LST and a minimum air temperature of 20.6°C at 0600 LST. Sunrise was at 0445 LST and sunset was at 1915 LST.

3.2 Surface temperature and sensible heat flux

To investigate the effects of surface heating by sky radiation on street canyon flow, the case with an ambient wind speed of 3 m s^{-1} is selected as a control simulation. During the day, the upwind building wall from 1200 LST to 1915 LST, the downwind building wall from 0445 LST to 1200 LST, and the road from 0840 LST to 1520 LST are the sunlit surfaces. The roof is always the sunlit surface in the daytime. Figure 3.2 shows the diurnal variations of surface

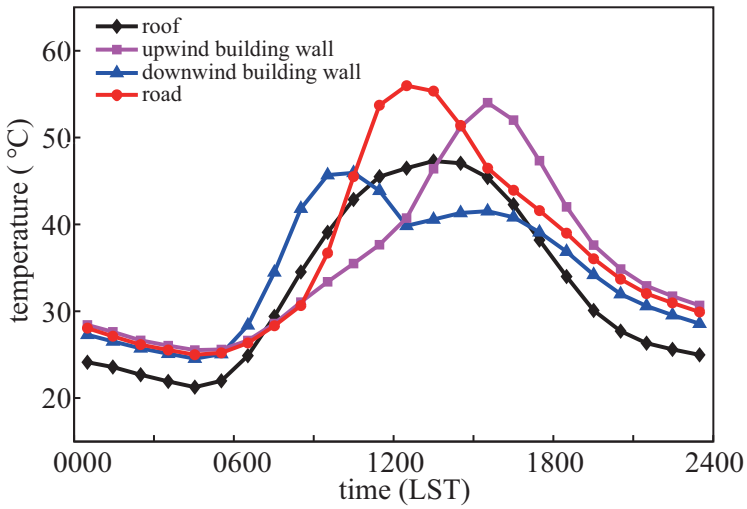

Figure 3.2. Diurnal variations of surface temperatures of roof (diamond), upwind building wall (square), downwind building wall (triangle), and road (circle) in the control simulation. Surface temperatures are hourly averaged.

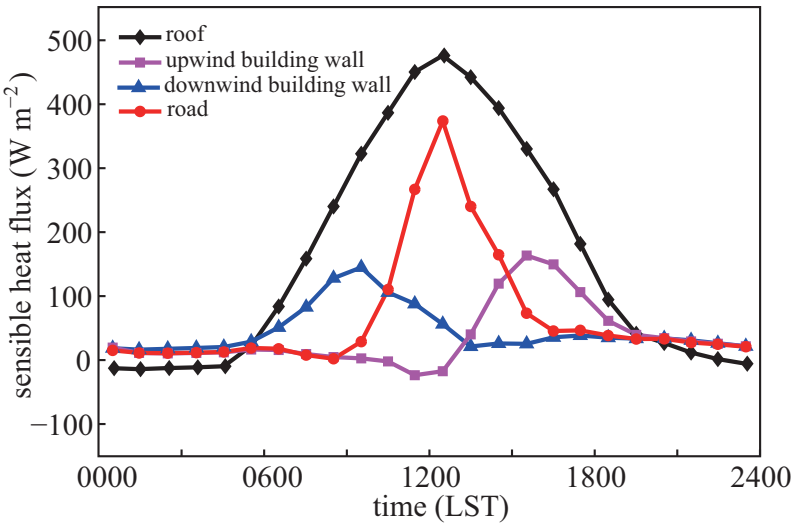

Figure 3.3. Diurnal variations of sensible heat fluxes from roof (diamond), upwind building wall (square), downwind building wall (triangle), and road (circle) in the control simulation. Surface sensible heat fluxes are hourly averaged.

temperatures in the control simulation. The maximum temperature at each surface is 47.3°C at 1330 LST (roof), 54.0°C at 1530 LST (upwind building wall), 45.9°C at 1030 LST (downwind building wall), and 56.0°C at 1230 LST (road). It is interesting that a secondary peak in the downwind building-wall temperature (41.5°C at 1530 LST) appears when the upwind building-wall temperature shows the maximum. The strongly heated surface also raises adjacent surface temperatures through longwave radiation emitted from the heated surface, thus forming the secondary peak. The radiation trapping effect in the street canyon is caused not only by emitted longwave radiation but also by reflected shortwave radiation. The road surface temperature is higher than the roof surface temperature around their peak times. This is partly due to the radiation trapping effect together with a low albedo (0.08) of the road. In the nighttime, the roof has the lowest surface temperature among the surfaces. This is related to the radiation trapping effect, which delays decreases in the surface temperatures of the walls and the road.

The diurnal variations of surface sensible heat fluxes are shown in Figure 3.3. The maximum sensible heat flux from each surface is 476 W m^{-2} at 1230 LST (roof), 163 W m^{-2} at 1530 LST (upwind building wall), 145 W m^{-2} at 0930 LST (downwind building wall), and 374 W m^{-2} at 1230 LST (road). In the daytime, the sensible heat flux is larger from the roof than from the road,

although the road surface temperature is higher than the roof surface temperature except in the early morning. Here, higher canyon air temperature than ambient air temperature plays a key role in reducing sensible heat fluxes from the walls and the road because surface sensible heat flux is proportional to the temperature difference between a surface and adjacent air. In the nighttime, sensible heat fluxes from the surfaces in the street canyon remain positive because of storage heat release. This storage heat in the nighttime is a consequence of large thermal inertia of the surfaces in the street canyon. A larger surface sensible heat flux implies a stronger thermal effect on street canyon flow since it strengthens buoyancy force in the vicinity of the strongly heated surface. Therefore, the diurnal variation of street canyon flow is strongly associated with that of surface sensible heat flux.

3.3 Street canyon flow and temperature

Figure 3.4 shows along-canyon averaged streamline fields in 1-h intervals from 0400 LST to 1500 LST. Streamline fields during the night before 0400 LST and in the afternoon after 1500 LST are almost the same as that at 0400 LST (Figure 3.4a) and 1500 LST (Figure 3.4l), respectively. A clockwise-rotating primary vortex, which is mechanically induced, forms in the street canyon at 0400, 0500, and 0600 LST (Figures 3.4a−c). At these times, the canyon-

averaged mean kinetic energy (a half of canyon-averaged square velocity) is about 0.16 m^2 s^{-2}. After the sun rises at 0445 LST, the sensible heat flux from the downwind building wall becomes larger than that from the upwind building wall and road. The downwind building-wall heating perturbs the primary vortex (Figure 3.4d). At 0800 LST, two counter-rotating vortices appear, which are the clockwise-rotating primary vortex remaining in the upper part and the counterclockwise-rotating secondary vortex growing in the lower part (Figure 3.4e). The lower vortex circulation interferes with the upper vortex circulation, so that the canyon-averaged mean kinetic energy decreases to 0.054 m^2 s^{-2} at 0820 LST. The road heating by direct shortwave radiation that starts from 0840 LST strengthens the lower vortex circulation. As the sensible heat flux from the road becomes larger, the mechanically induced upper vortex shrinks from 0900 LST to 1100 LST (Figures 3.4f–h) with increasing canyon-averaged mean kinetic energy from 0.063 m^2 s^{-2} at 0900 LST to 0.186 m^2 s^{-2} at 1100 LST. After the sensible heat flux from the road becomes larger than that from the downwind building wall, the two counter-rotating vortices have difficulty in sustaining themselves and are abruptly merged into a single primary vortex again (Figure 3.4i). The road heating strengthens the primary vortex circulation and increases the canyon-averaged mean kinetic energy, which is 1.09 m^2 s^{-2} at 1145 LST (daily maximum value). In the afternoon, the upwind building-wall heating

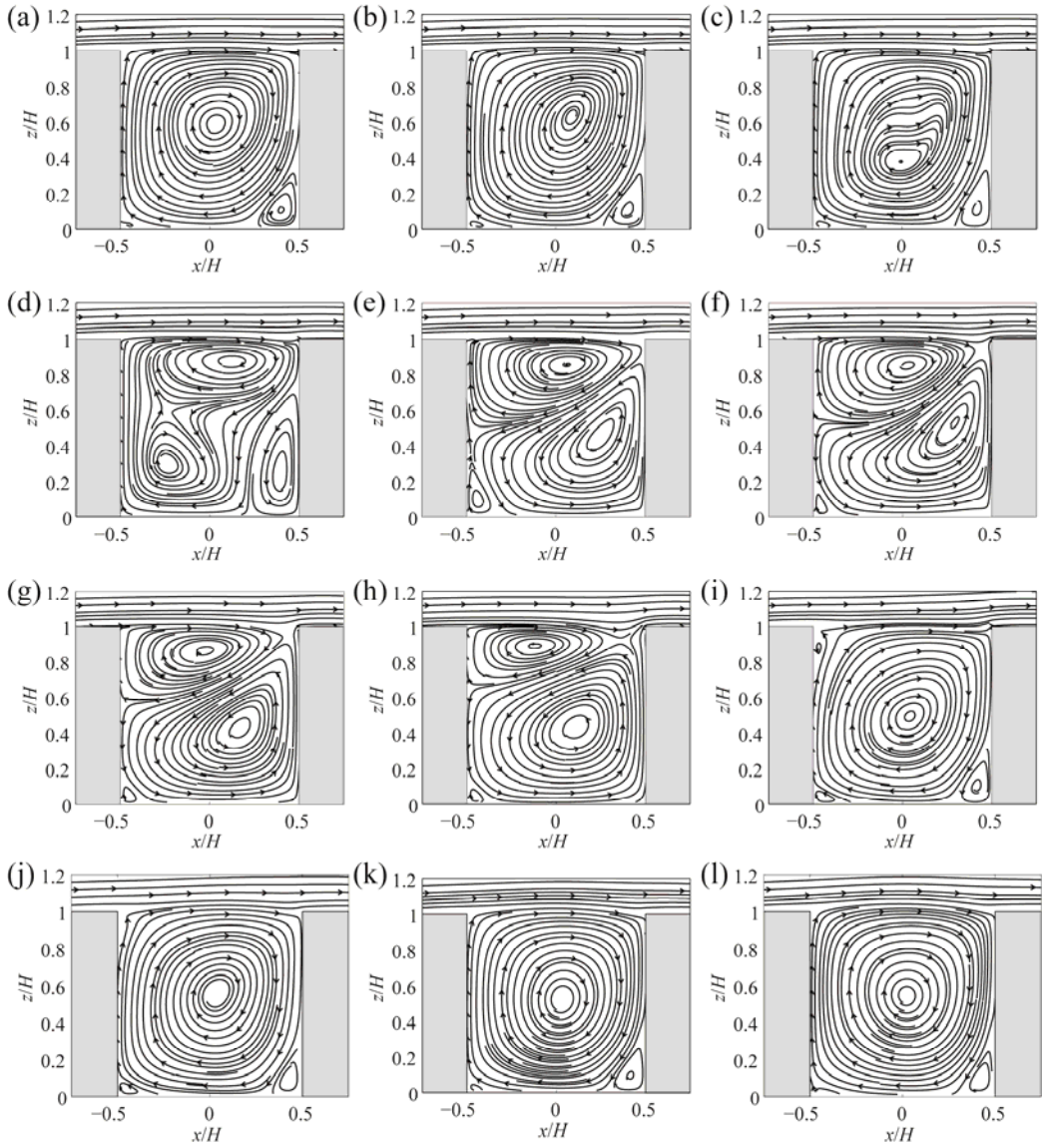

Figure 3.4. Along-canyon averaged streamline fields at (a) 0400, (b) 0500, (c) 0600, (d) 0700, (e) 0800, (f) 0900, (g) 1000, (h) 1100, (i) 1200, (j) 1300, (k) 1400, and (l) 1500 LST in the control simulation. The along-canyon average is taken from $y/H = -1.25$ to 1.25.

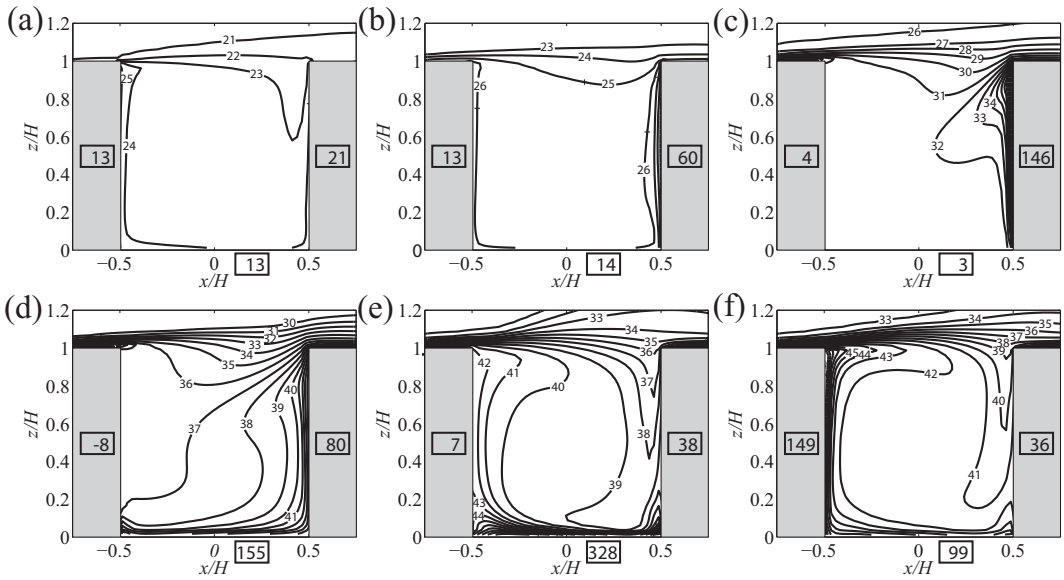

Figure 3.5. Along-canyon averaged temperature fields at (a) 0500, (b) 0700, (c) 0900, (d) 1100, (e) 1300, and (f) 1500 LST in the control simulation. The contour interval is 1 °C. The values in the boxes indicate the area-averaged sensible heat fluxes from surfaces in W m^{-2}.

increases sensible heat flux from the wall, whereas sensible heat flux from the road decreases. Then, canyon-averaged mean kinetic energy decreases. The vortex shape changes very little in the afternoon (Figures 3.4j–l).

Based upon the analysis of the diurnal variation of the street canyon flow, two flow regimes are identified. Flow regime I is characterized by a primary vortex shown at 0400, 0500, 0600, 1200, 1300, 1400, and 1500 LST in Figure 3.4. This flow regime appears with road and/or upwind building-wall heating as well as no surface heating. Flow regime II is characterized by two counter-rotating vortices consisting of a mechanically driven upper vortex and a thermally driven lower vortex. This flow regime appears at 0800, 0900, 1000, and 1100 LST in Figure 3.4 when the downwind building wall is strongly heated. In the control simulation, the regime transitions from I to II and from II to I occur at 0700 LST and 1130 LST, respectively. A streamline field at 0700 LST (Figure 3.4d) represents a transition of flow regime. The transition time of the flow regimes depends on ambient wind speed and differential sensible heat fluxes between the walls and road (not shown here).

Figure 3.5 shows along-canyon averaged temperature fields at 0500, 0700, 0900, 1100, 1300, and 1500 LST. When the downwind building-wall heating is insignificant in the early morning (Figures 3.5a and b), the temperature fields in the street canyon are relatively uniform. Since the canyon air

temperature is higher than the air temperature above the roof level, the entrance region of ambient air into the street canyon, located near the roof of the downwind building, coincides with the low temperature region in the canyon. In flow regime II, the temperature field changes in accordance with the locations of two counter-rotating vortices (Figures 3.5c and d). Cool ambient air mostly flows into the upper vortex, whereas heated air near the downwind building wall tends to stay in the lower vortex. Thus, the spatial extent of high/low temperature expands/shrinks as downwind building-wall heating increases. The temperature field changes remarkably when the transition from flow regime II to flow regime I occurs (i.e., from Figure 3.5d to Figure 3.5e). After the transition occurs, the region of cool/warm air appears along the downwind/upwind building wall, following the clockwise vortex circulation in flow regime I (Figures 3.5e and f).

3.4 Sensitivity to ambient wind speed

Figure 3.6 shows along-canyon averaged streamline fields at 0800, 0900, and 1000 LST for ambient wind speeds of 2, 4, and 6 m s^{-1}. As the ambient wind speed increases from 2 m s^{-1} to 6 m s^{-1}, it is clear in flow regime II that a mechanically driven upper vortex expands, whereas a thermally driven lower vortex shrinks. A slope of margin between the two vortices also changes. The slope is less steep with increasing ambient wind speed. When the ambient wind

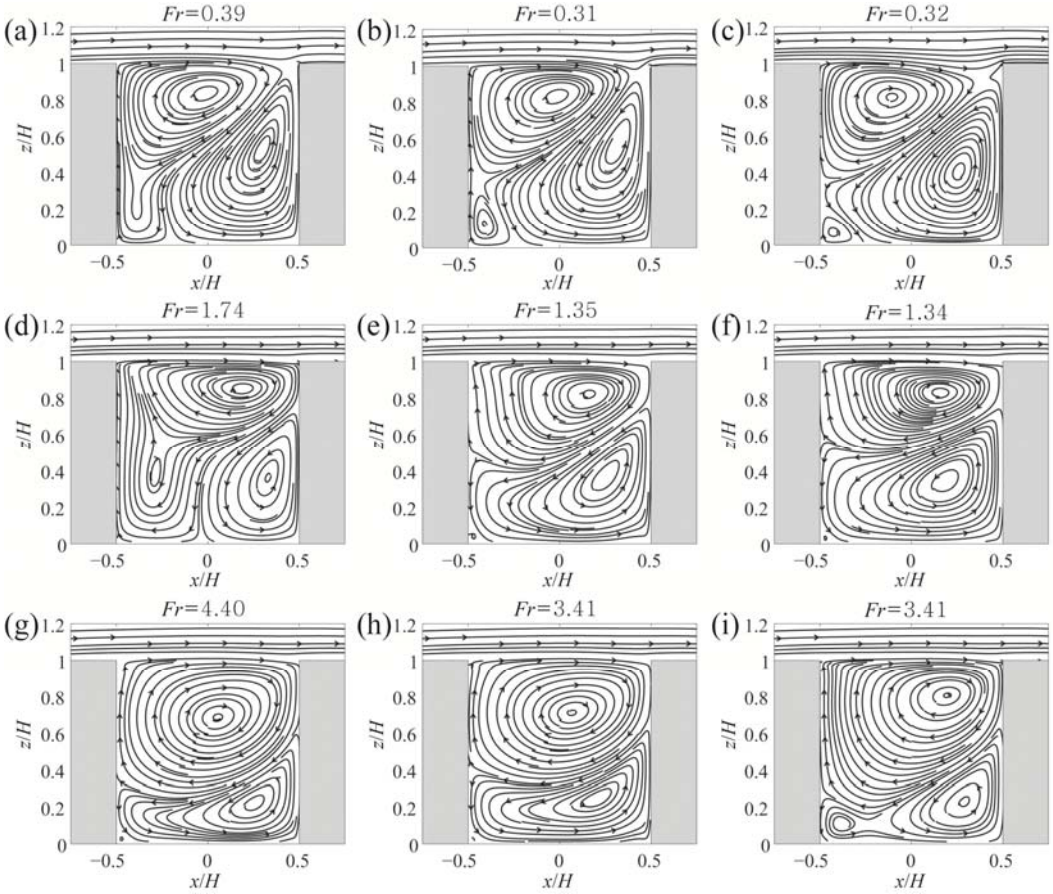

Figure 3.6. Along-canyon averaged streamline fields (a) 0800, (b) 0900, and (c) 1000 LST for an ambient wind speed of 2 m s^{-1}, at (d) 0800, (e) 0900, and (f) 1000 LST for an ambient wind speed of 4 m s^{-1}, and at (g) 0800, (h) 0900, and (i) 1000 LST for an ambient wind speed of 6 m s^{-1}. The values of the Froude number are given.

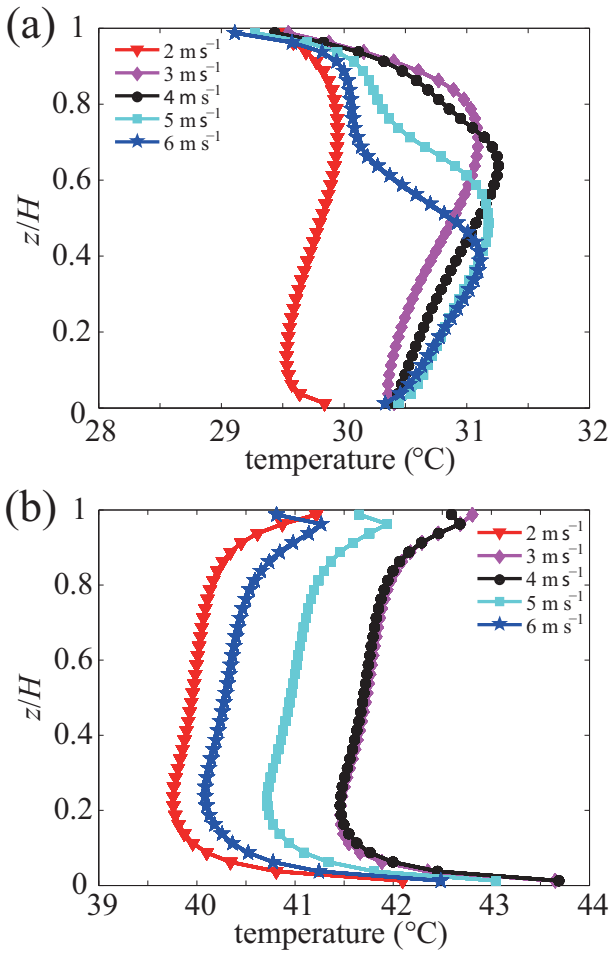

Figure 3.7. Vertical profiles of areal and hourly averaged canyon air temperatures in (a) 0800−0900 LST and (b) 1500−1600 LST for ambient wind speeds of 2, 3, 4, 5, and 6 m s^{-1}.

speed is 2 m s^{-1}, the lower vortex reaches the roof level near the downwind building. Hence, heat can be directly exchanged across the roof level (Figures 3.6a–c). When the ambient wind speeds are 4 m s^{-1} (Figures 3.6d–f) and 6 m s^{-1} (Figures 3.6g–i), on the other hand, there is downward motion near the upper part of the downwind building. Therefore, the downward motion enhanced by strong ambient wind plays an important role in enlarging the upper vortex and reducing the slope of margin between the two vortices.

Flow fields in Figure 3.6 are compared to those in the wind-tunnel study by Kovar-Panskus et al. (2002). For this, the Froude number defined as $Fr = U_{\mathrm{amb}}{}^2 T_{\mathrm{amb}} / gH(T_i - T_{\mathrm{amb}})$ is introduced. Here, T_{amb} is the ambient air temperature, g is the gravitational acceleration, and T_i is the downwind building-wall temperature. Since the downwind building-wall temperature is little changed by the ambient wind speed, Fr decreases with decreasing ambient wind speed. Fr is lower at 0900 and 1000 LST than at 0800 LST according to the variation of the downwind building-wall temperature (see Figure 3.2). As Fr decreases, the upper vortex shrinks and moves upward. This is consistent with the wind-tunnel result of Kovar-Panskus et al. (2002). Different flow patterns between our simulations and the wind-tunnel experiments for similar Fr might be caused to some extent by the temperature differences of other surfaces.

Figure 3.7 shows the areal (*xy*-plane) and hourly averaged vertical profiles of canyon air temperatures in 0800−0900 LST (flow regime II) and 1500−1600 LST (flow regime I). In flow regime II, the vertical temperature profiles reflect the extent of the upper vortex. As the ambient wind speed increases, the vertical level of the highest air temperature is lowered due to the expansion of the upper vortex. In flow regime I, the canyon air temperature does not vary significantly with height except near the street bottom and roof level. As the ambient wind speed increases, the canyon-averaged air temperature decreases because heat exchange across the roof level becomes large. When an ambient wind speed is 2 m s^{-1}, canyon vortices are not completely isolated from the ambient flow, allowing the active interaction of canyon air with ambient air across the roof level in both flow regimes.

Relationships between canyon wind speed and ambient wind speed are given in previous studies. Nakamura and Oke (1988) suggested an approximately linear relationship between canyon wind speed and ambient wind speed. Santamouris et al. (1999) argued that canyon wind speed is not directly related to ambient wind speed because not only a mechanical influence but also a thermal influence is important in the canyon circulation for weak ambient winds.

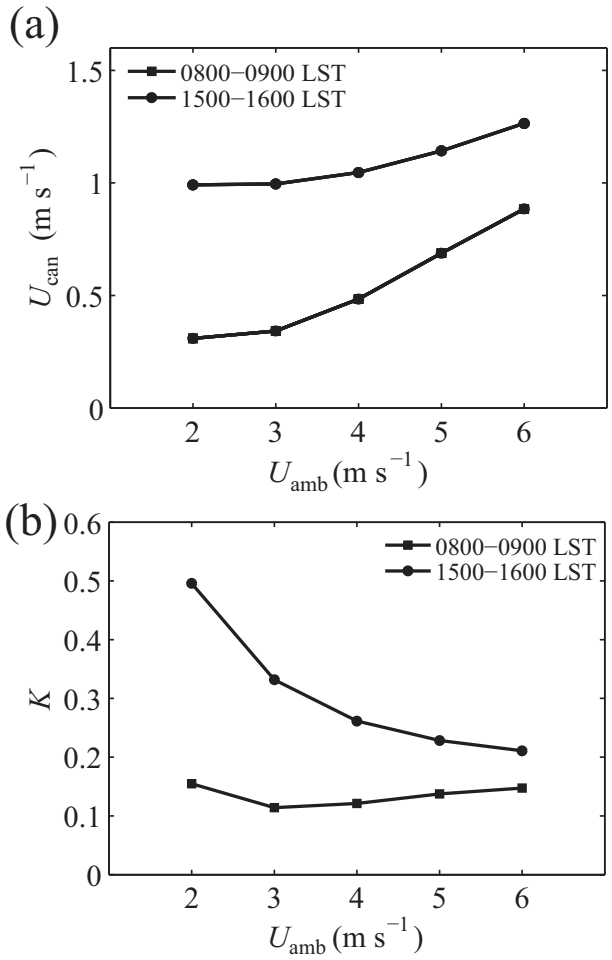

Figure 3.8. Variations of (a) mean canyon wind speed (U_{can}) and (b) normalized canyon wind speed (K) in 0800−0900 LST (square) and 1500−1600 LST (circle) with ambient wind speed.

We examine the relationship between canyon wind speed and ambient wind speed in two flow regimes. Figure 3.8 shows the variations of mean canyon wind speed (U_{can}) and normalized canyon wind speed ($K = U_{can}/U_{amb}$) with the ambient wind speed. The mean canyon wind speed is defined and calculated as the root mean square velocity in the street canyon. The dependencies of *K* on the ambient wind speed are different in the two flow regimes (Figure 3.8b). In 1500−1600 LST (flow regime I), *K* decreases with increasing ambient wind speed because the mean canyon wind speed is large even for weak ambient winds (e.g., 2 and 3 m s^{-1}). The mean canyon wind speed is not proportional to the ambient wind speed. In 0800−0900 LST (flow regime II), on the other hand, *K* does not change much between 0.1 and 0.2 with the ambient wind speed, showing a linear relationship between mean canyon wind speed and ambient wind speed. This linear relationship is in agreement with the finding of Nakamura and Oke (1988). For strong ambient winds (e.g., 5 and 6 m s^{-1}), *K* is approximately close to 0.2 regardless of flow regime. For weak ambient winds (e.g., 2 and 3 m s^{-1}), however, *K* significantly deviates from 0.2 in flow regime I because thermal influence as well as mechanical influence becomes important as mentioned in Santamouris et al. (1999). The difference in the dependencies of *K* on the ambient wind speed in two flow regimes implies that differential sensible heat fluxes from the surfaces play an important role in strengthening and

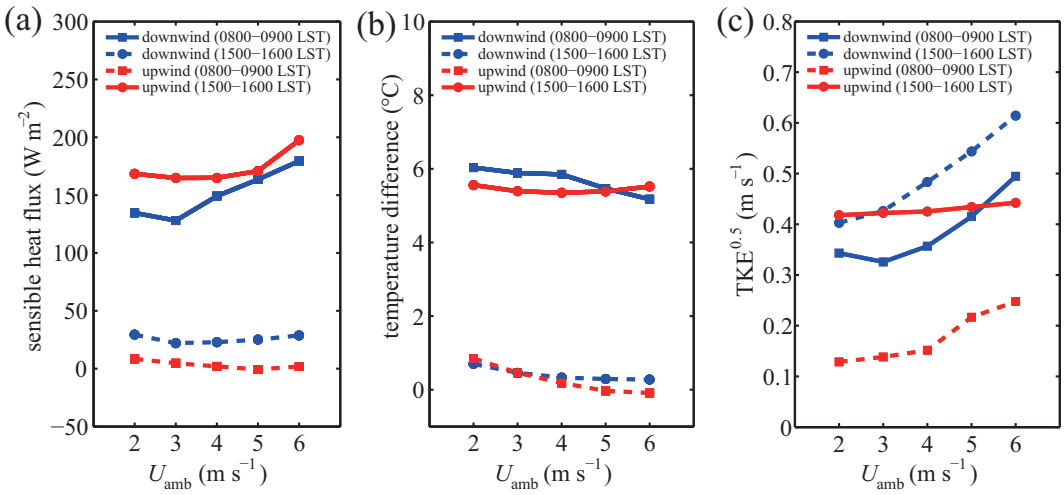

Figure 3.9. Variations of hourly averaged (a) surface sensible heat fluxes, (b) temperature differences between walls and adjacent air, and (c) roots of adjacent turbulent kinetic energies (TKE) with ambient wind speed. These are for downwind building wall and upwind building wall in 0800−0900 LST (square) and 1500−1600 LST (circle). The adjacent air temperatures and the turbulent kinetic energies are *yz*-plane averaged at $x/H = -0.4875$ (the closest plane to the upwind building wall) and $x/H = 0.4875$ (the closest plane to the downwind building wall) in the street canyon.

weakening street canyon flow, especially for weak ambient winds. To confirm this implication, the dependencies of sensible heat fluxes from the walls on the ambient wind speed are examined (Figure 3.9a). In 1500−1600 LST (flow regime I), the sensible heat flux from the upwind building wall remains almost constant between 165 W m^{-2} and 171 W m^{-2} regardless of the ambient wind speed, except in the case of an ambient wind speed of 6 m s^{-1}. In 0800−0900 LST (flow regime II), on the other hand, the sensible heat flux from the downwind building wall increases from 128 W m^{-2} (3 m s^{-1}) to 179 W m^{-2} (6 m s^{-1}) with increasing ambient wind speed, except in the case of an ambient wind speed of 2 m s^{-1}. In both periods, the sensible heat fluxes from the road do not significantly vary with the ambient wind speed (not shown here). As mentioned in subsection 2.2, the surface sensible heat flux depends on the turbulent kinetic energy and the temperature difference between a surface and its adjacent air. Temperature difference between a wall and air determines the magnitude of sensible heat flux from the wall but does not strongly depend on the ambient wind speed for all cases as shown in Figure 3.9b. However, the root of the turbulent kinetic energy shows a strong dependency on the ambient wind speed near the downwind building, compared to that near the upwind building (Figure 3.9c). In addition to the turbulent kinetic energy produced by buoyancy near the heated wall, a large amount of turbulent kinetic energy produced in a shear layer

near the roof level is transported to the region near the downwind building wall. By analyzing turbulent kinetic energy fields, it is found that the turbulent kinetic energy produced by wind shear increases with increasing ambient wind speed, but that produced by buoyancy near the heated wall is nearly independent of the ambient wind speed (not shown). Therefore, the sensible heat flux from the downwind building wall in 0800−0900 LST shows a significant change with the ambient wind speed (from 3 m s^{-1} to 6 m s^{-1}), whereas that from the upwind building wall in 1500−1600 LST shows little change with the ambient wind speed (from 2 m s^{-1} to 5 m s^{-1}).

A canyon wind speed is primarily related to momentum transport from ambient flow across a shear layer. In addition, differential sensible heat fluxes from the walls also affect a canyon wind speed. For weak ambient winds, the mean canyon wind speeds in 0800−0900 LST are relatively small because the sensible heat fluxes from the downwind building-wall are small. For strong ambient winds, the mean canyon wind speeds in 0800−0900 LST are relatively large because the sensible heat fluxes from the downwind building-wall are large. In 1500−1600 LST, however, the mean canyon wind speeds for weak ambient winds are relatively large because the surface sensible heat fluxes for weak ambient winds are still large. This is a reason for large *K*. Therefore, the different relationships between mean canyon wind speed and ambient wind speed in the

two flow regimes are attributed to their different dependencies of surface sensible heat flux on the ambient wind speed.

4 Coupling Complex Chemical Mechanism to CFD Model

4.1 Carbon bond mechanism Ⅳ (CBM–Ⅳ)

The CBM–Ⅳ adopted for this study has 36 reactive species and 93 reactions (Gery et al., 1989). The reactive species in the CBM–Ⅳ are listed in Table 4.1. VOCs are lumped in terms of carbon bond structures. PAR is a one-carbon surrogate for alkanes with a carbon single bond. OLE is a two-carbon surrogate for alkenes with a carbon double bond. ALD_2 is a two-carbon carbonyl surrogate for acetaldehydes or higher aldehydes. TOL and XYL are representations for lumped species with mono-alkyl-benzene structures (seven-carbon species) and di- or tri-alkyl-benzene structures (eight- or nine-carbon species), respectively. In contrast to the lumped species above, FORM and ETH are representations for single species that are formaldehyde and ethene, respectively. Simple isoprene (ISOP) chemistry is included (Carter, 1996).

4.2 Coupling strategy

The transport equation of a reactive species is given as

$$\frac{\partial C_i}{\partial t} + U_j \frac{\partial C_i}{\partial x_j} = D \frac{\partial^2 C_i}{\partial x_j \partial x_j} + \frac{\partial}{\partial x_j}\left(K_c \frac{\partial C_i}{\partial x_j} \right) + \left[\frac{\partial C_i}{\partial t} \right]_{\text{chem}} . \quad (4.1)$$

Here, C_i is the concentration of the ith reactive species, U_j the jth mean velocity component, D the molecular diffusivity of the species, and K_c the eddy diffusivity of the species. The last term denotes the net chemical production rate of the species calculated by the CBM–Ⅳ. The reaction coefficients in the CBM–Ⅳ are calculated at the atmospheric pressure and at the air temperature of 298 K, and the photolysis rate coefficients of NO_2, NO_3, HONO, O_3, H_2O_2, FORM, ALD_2, OPEN, MGLY, and ISPD are obtained from Jacobson (2005). The Eulerian backward iteration (EBI) method (Hertel et al., 1993) is used as a chemical solver to integrate the stiff system of photochemical reactions. Of the 36 reactive species in the CBM–Ⅳ, 23 are regarded as the species whose concentrations are calculated using the EBI method. The concentrations of the other 13 species are explicitly calculated (Table 4.1).

4.3 Validation

Explicit method (13 species)		EBI method (23 species)	
representation	species name	representation	species name
NO	Nitric oxide		Nitric acid
NO_2	Nitrogen dioxide	HNO_3	Hydrogen peroxide
NO_3	Nitrate radical	H_2O_2	Carbon monoxide
N_2O_5	Dinitrogen pentoxide	CO	Formaldehyde
HONO	Nitrous acid	FORM	High molecular weight
PNA	Peroxynitric acid	ALD_2	aldehydes
O^1D	Oxygen atom $O^1(D)$	PAR	Paraffin carbon bond
O	Oxygen atom $O^3(P)$	ROR	Secondary organic oxy radical
OH	Hydroxyl radical	NTR	Organic nitrate
O_3	Ozone	OLE	Olefinic carbon bond
HO_2	Hydroperoxy radical	ETH	Ethene
C_2O_3	Peroxyacyl radical	TOL	Toluene
PAN	Peroxyacyl nitrate	CRES	Cresol and higher molecular
			weight phenols
		TO_2	Toluene-hydroxyl radical
		CRO	adduct
		OPEN	Methylphenoxy radical
			High molecular weight aromatic
		XYL	oxidation ring fragment
		MGLY	Xylene
		ISOP	Methylglyoxal
		ISPD	Isoprene
		XO_2	Isoprene product
		XO_2N	NO-to-NO_2 operation
		SO_2	NO-to-nitrate operation
		SULF	Sulfur dioxide
			Sulfuric acid (gaseous)

Table 4.1. Reactive species in the CBM–Ⅳ.

The coupled CFD model is validated for NO_2 and NO_x concentrations against the field experiment data obtained during the Texas Roadway Study on 13 July 2007 (Zhu et al., 2009; Clements et al., 2009). The target road has two track lines, a width of 8.5 m, and a traffic volume of 1038 vehicles h^{-1}. During the measurement period, the wind direction is nearly perpendicular to the road. In this validation simulation, the background concentrations of NO_2, NO_x, O_3, HO_2, RO_2, HCHO, and CH_3CHO, the roadside concentrations of NO_2 and NO_x (source strength), the road temperature, and other meteorological parameters summarized in Wang et al. (2011) are used and the thermodynamic energy equation is included. Following Wang et al. (2011), 4 measurement points at the distances of 14, 62, 109, and 157 m from the road are considered for this validation.

Figure 4.1 shows the simulated and measured NO_2 and NO_x concentrations as a function of distance. The simulated NO_2 concentrations are slightly overestimated. The difference between the simulated and measured NO_2 concentrations decreases with increasing distance from the road. This difference is 1.4 ppb at the nearest point and 0.17 ppb at the farthest point. In contrast, the simulated NO_x concentrations match the measured values very well. From Figure 4.1, it is inferred that the NO to NO_2 conversion in the simulation is greater than the actual conversion especially near the road. To some extent, this might be due

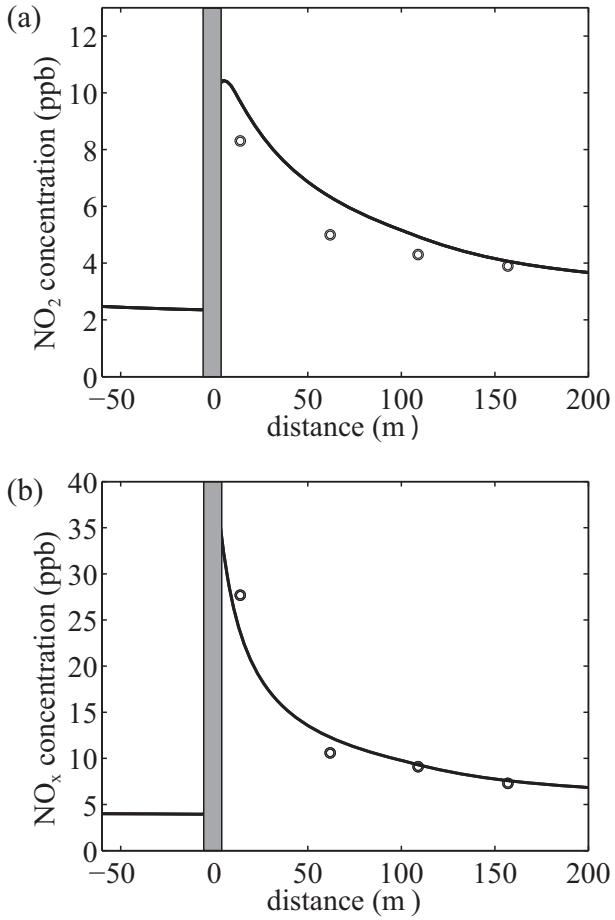

Figure 4.1. (a) NO_2 and (b) NO_x concentrations with distance in the simulation (line) and measurement (circle). The road is shaded.

to the uncertainties in the initial NO_2-to-NO_x ratio and the NO_2 photolysis rate coefficient. Overall, the CFD model coupled with the CBM–Ⅳ successfully simulates the NO_2-to-NO_x ratio that is an important indicator for urban atmospheric chemistry. The NO_2-to-NO_x ratio at a distance of 62 m from the road is 0.52 in the simulation and 0.47 in the measurement.

5 Reactive Pollutant Dispersion in and above a Street Canyon

5.1 Experimental design

Figure 5.1 illustrates a two-dimensional domain and an idealized street canyon. Both the building height (H) and the street canyon width (W) are 20 m, giving a canyon aspect ratio (H/W) of 1. The domain size is 40 m in the x-direction and 60.1 m in the z-direction. The grid interval is 0.5 m in the x-direction. The grid interval in the z-direction is 0.5 m up to z = 32 m and then gradually increases with an expansion ratio of 1.1. The ambient wind blows in the positive x-direction. The boundary conditions for the velocity components, turbulent kinetic energy, and its dissipation rate follow Baik et al. (2007). For example, the ambient wind speed at the roof level of the inflow boundary is 3.9 m s^{-1}. The isothermal condition is applied, assuming the air temperature of 298 K. For concentrations, the cyclic boundary condition in the x-direction is applied at the inflow and outflow boundaries and the zero-gradient boundary condition is applied at the upper boundary. An area source of 9 emission species (NO, NO_2, FORM, ALD_2, PAR, OLE, ETH, TOL, and XYL) is located at the lowest model level (z/H = 0.0125; hereafter referred to as the street bottom) in the street canyon. The CFD model is integrated for 90 min with a time step of 0.1 s.

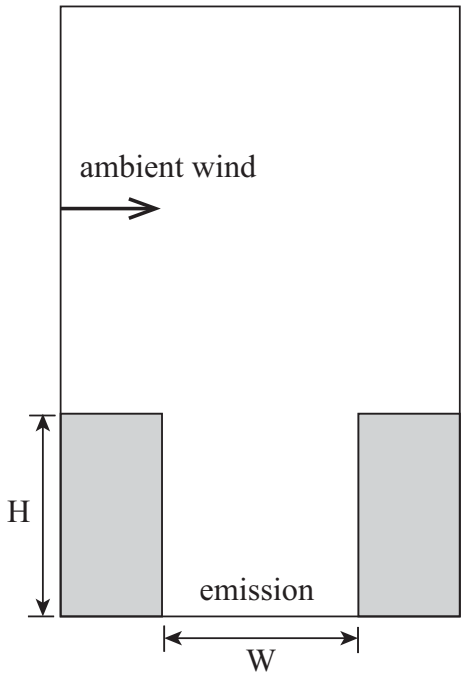

Figure 5.1. Illustration of computational domain and buildings. *H* is the building height and *W* is the street canyon width.

The initial concentrations of all reactive species are calculated using a chemistry box model composed of the same chemical mechanism and chemical solver. Concentrations calculated by a one-hour simulation of the chemistry box model reach an approximately quasi-steady state, while the concentrations of 9 emission species and O_3 are constrained at 10 ppb (NO), 30 ppb (NO_2), 30 ppb (O_3), and 40 ppb (7 VOCs in total). The relative portions of the 7 VOC concentrations among the emission species in volume are 56.3% for PAR, 12.4% for TOL, 11.9% for XYL, 9.5% for ETH, 6.7% for OLE, 2.1% for ALD_2, and 1.1% for FORM (Smylie et al., 1991; Bossioli et al., 2002). For the first 30 min of time integration, the concentrations of all reactive species are calculated without emission and chemical production or loss. After t = 30 min, the concentrations are calculated by considering advection, diffusion, emission, and chemical processes simultaneously at every time step. All results are analyzed at t = 90 min when the concentrations of reactive species are in an approximately pseudo steady-state in the street canyon.

Table 5.1 shows 14 emission scenarios of NO_x and VOCs with the same relative portions of the 7 VOC concentrations in the chemistry box model simulation. For analyzing the dispersion of reactive species in an approximately pseudo steady-state, concentrations of 9 emission species at the street bottom are specified as emission levels. Here, the NO_x and VOC concentrations of 300 ppb

No.	NO_x (ppb)	7 VOCs (ppb)	VOC/NO_x	O_3 sensitivity
S1	150	300	2.00	O
S2	225	300	1.33	X
S3 (base)	300 (1.0 NO_x)	300 (1.0 VOC)	1.00	O
S4	375	300	0.80	X
S5	450	300	0.67	X
S6	150	600	4.00	X
S7	225	600	2.67	X
S8	300	600	2.00	X
S9	375	600	1.60	X
S10	450	600	1.33	X
S11	300	150	0.50	O
S12	300	450	1.50	X
S13	300	750	2.50	X
S14	300	900	3.00	X

Table 5.1. Emission scenarios for NO_x and 7 VOCs.

are designated as emission levels of 1.0 NO_x and 1.0 VOC, respectively. The 14 emission scenarios cover the ratio of VOC to NO_x emission (the VOC-to-NO_x emission ratio) ranging from 0.5 (1.0 NO_x and 0.5 VOC) to 4 (0.5 NO_x and 2.0 VOC). Three emission scenarios in the last column of Table 5.1 are used to examine the O_3 sensitivity (subsection 3.3). In this study, two species (SO_2 and SULF) out of the 36 species in the CBM–Ⅳ are excluded for neglecting sulfur chemistry.

5.2 Dispersion types

The dispersion of NO, NO_2, and O_3 in street canyons using the simple photochemistry among them was numerically investigated by Baker et al. (2004), Baik et al. (2007), and Garmory et al. (2009). Garmory et al. (2009) examined the dispersion using the simple photochemistry and also the CBM–Ⅳ and indicated that NO, NO_2, and O_3 concentrations calculated using the CBM–Ⅳ are similar to those calculated using the simple photochemistry within approximately 1 ppb for the same experimental setting. However, they did not consider VOC emission and its impacts on O_3 concentration in the simulations. Here, we first examine the dispersion of NO, NO_2, and O_3 with the complexity of VOC

chemistry. Then, we examine the dispersion of other reactive species and compare it to the dispersion of NO, NO_2, and O_3.

Figure 5.2 shows the streamline field and the NO, NO_2, and O_3 concentration fields in and above the street canyon for the emission scenario of 1.0 NO_x and 1.0 VOC (S3; base scenario). A primary vortex is formed in the street canyon. Because the less-polluted ambient air flows into the street canyon near the downwind building wall, the NO concentration is lower near the downwind building wall than near the upwind building wall. The NO_2 concentration is broadly high over 55 ppb around the center of the street canyon. Because the NO_2 concentration above the street canyon is also comparably high, there is no significant impact of inflow on the concentration near the downwind building wall. The O_3 concentration below 30 ppb in the street canyon is primarily the result of the $NO + O_3 \rightarrow NO_2$ reaction (NO titration of O_3) that is a major sink of O_3. Around the center of the street canyon, the low NO and high NO_2 concentrations coincide with the low O_3 concentration. NO, NO_2, and O_3 do not reach a photo-stationary state among them because chemical O_3 loss due to the NO titration is not exactly balanced by chemical O_3 production due to the NO_2 photolysis. In the street canyon, the NO titration of O_3 that is more pronounced than the NO_2 photolysis causes the net chemical O_3 loss. The

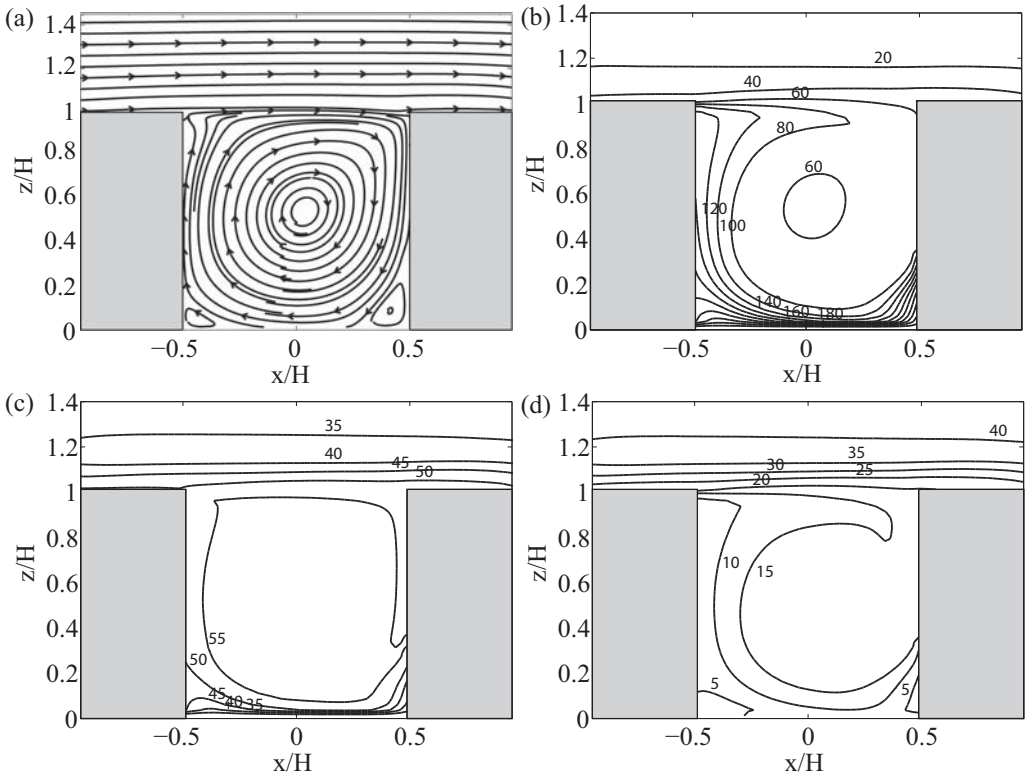

Figure 5.2. (a) Streamline field and (b) NO, (c) NO_2, and (d) O_3 concentration fields in and above the street canyon for the emission scenario of 1.0 NO_x and 1.0 VOC.

chemical O_3 loss is substantially compensated by the inflow of O_3 from the ambient air. Above the street canyon, the NO_2 photolysis that is more pronounced than the NO titration of O_3 causes the net chemical O_3 production. In addition to the differences in experimental setting, this chemical imbalance explains why the dispersion pattern of NO_2 in the street canyon that we found differs from the result of Baker et al. (2004) using the simple photochemistry that assumes a photo-stationary state for NO, NO_2, and O_3. Dispersion types of other reactive species are classified into the NO-type, NO_2-type, and O_3-type dispersion. The NO-type and NO_2-type dispersion are identified when the concentration is maximized at the street bottom and near the center of the street canyon, respectively. The species in these two dispersion types show higher concentrations in the street canyon than above it. The O_3-type dispersion is identified when the concentration is higher above the street canyon than in it.

Figure 5.3 shows the vertical profiles of the street canyon width-averaged concentrations. The average is taken over the street canyon width from $x/H = -0.5$ to 0.5. Each species concentration is normalized by the corresponding concentration at the street bottom. Based on their vertical profiles, 9 species (NO, HONO, ALD_2, PAR, ROR, OLE, ETH, TOL, and XYL) are classified into the NO-type dispersion (Figure 5.3a). Out of the 9 species, 7 species are emission species for which their concentrations are specified at the street bottom. HONO

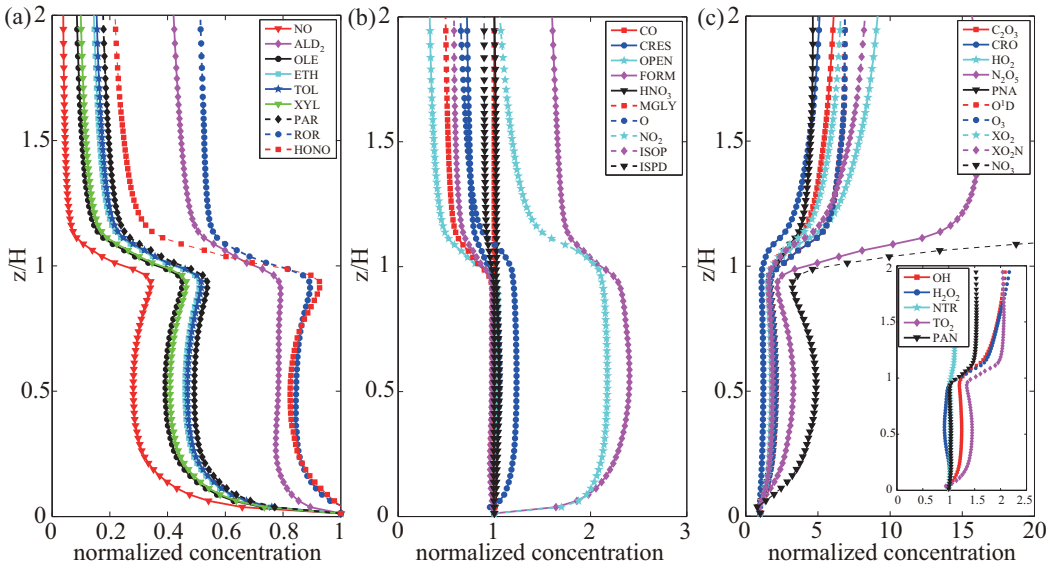

Figure 5.3. Vertical profiles of the street canyon width-averaged concentrations of species in (a) NO-type dispersion, (b) NO_2-type dispersion, and (c) O_3-type dispersion for the emission scenario of 1.0 NO_x and 1.0 VOC. Each species concentration is normalized by that at the street bottom.

and ROR are not emission species but can be directly produced by chemical reactions related to emission species. Ten species (NO_2, O, HNO_3, CO, FORM, CRES, OPEN, MGLY, ISOP, and ISPD) are classified into the NO_2-type dispersion (Figure 5.3b). Their concentration maxima appear near $z/H = 0.5$. NO_2 and FORM are emission species but are effectively produced in the street canyon by the NO titration of O_3 and by the oxidation of VOCs, respectively. CO concentration (approximately 1 ppm) is relatively high compared to the concentrations of the other species. Chemical processes, therefore, barely affect the CO concentration in and above the street canyon and the difference in CO concentration between in and above the street canyon is insignificant. Fifteen species (NO_3, N_2O_5, PNA, O^1D, OH, O_3, HO_2, C_2O_3, PAN, H_2O_2, NTR, TO_2, CRO, XO_2, and XO_2N) are classified into the O_3-type dispersion (Figure 5.3c). In this base scenario, all radical species except for O (NO_2-type) and ROR (NO-type) show the O_3-type dispersion. Species in the O_3-type dispersion experience large changes in normalized concentration with height as crossing the roof level. Because the street canyon is polluted with emission species, the chemical losses of highly reactive species are more promoted by their reactions with emission species in the street canyon than above it. Therefore, the rapid losses of highly reactive species lead to low concentrations in the street canyon compared to concentrations above the street canyon.

The dispersion type is not an inherent feature of a reactive species. The dispersion type may change in response to the emission level of NO_x or VOC. This is systematically analyzed for the emission scenarios of 0.5 to 1.5 NO_x with 1.0 VOC (S1–S5) and the emission scenarios of 0.5 to 3.0 VOC with 1.0 NO_x (S3, S8, S11–S14). While the NO- type dispersion is found to be invariable, transitions in dispersion type between the NO_2-type and the O_3-type dispersion are found to occur. The dispersion of HNO_3 is shifted from the NO_2-type dispersion (S3) to the O_3-type dispersion (S5, S11). In contrast, the dispersion of PNA, PAN, NTR, and TO_2 are shifted from the O_3-type dispersion (S3) to the NO_2-type dispersion (S1, S8, S12, S13, S14).

Figure 5.4 shows the vertical profiles of the street canyon width-averaged PNA, PAN, NTR, and TO_2 concentrations for the 3 emission scenarios of 0.5, 1.0, and 1.5 NO_x with 1.0 VOC (S1, S3, S5). As the NO_x emission level decreases, the concentrations in the street canyon increase more markedly than those above it. This change leads to a transition from the O_3-type dispersion (S3, S5) to the NO_2-type dispersion (S1). Figure 5.5 shows the vertical profiles of the street canyon width-averaged PNA, PAN, NTR, and TO_2 concentrations for the 3 emission scenarios of 1.0, 2.0, and 3.0 VOC with 1.0 NO_x (S3, S8, S14). As the VOC emission level increases, it is also clear that the concentrations in the street canyon increase more markedly than those above it. This change leads to a

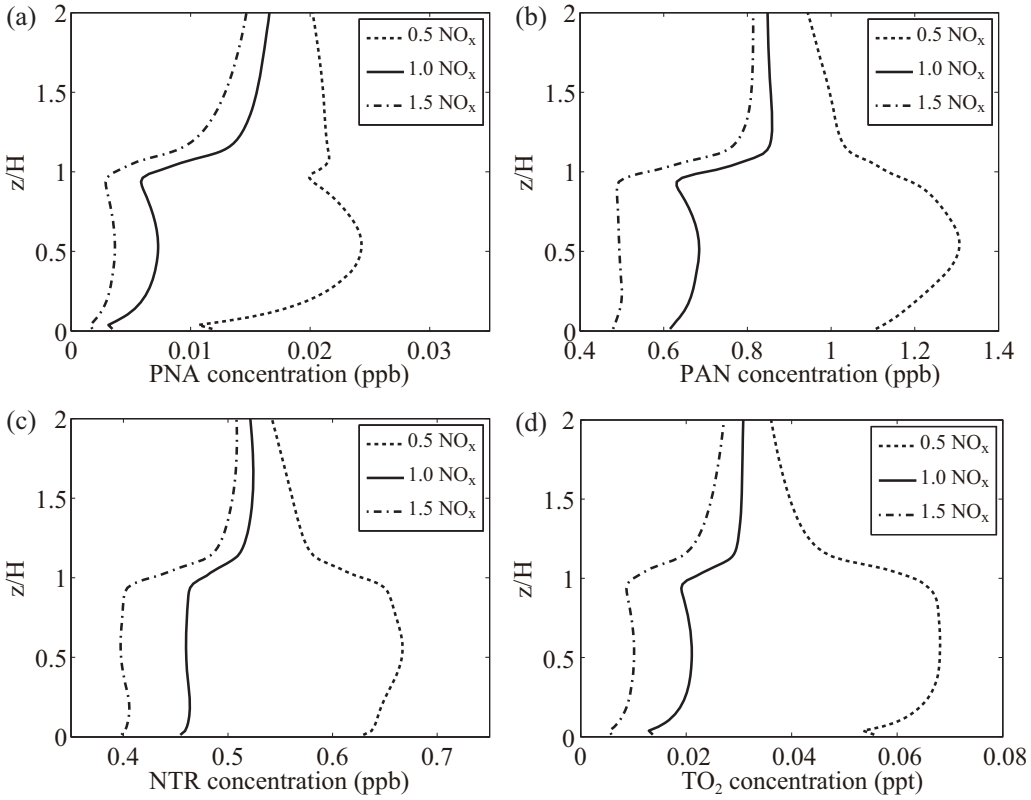

Figure 5.4. Vertical profiles of the street canyon width-averaged concentrations of (a) PNA, (b) PAN, (c) NTR, and (d) TO_2 for the emission scenarios of 0.5, 1.0, and 1.5 NO_x with 1.0 VOC.

transition from the O_3-type dispersion (S3) to the NO_2-type dispersion (S8, S14). In addition to the 4 species, all species in the O_3-type dispersion except for two species (O_3 and O^1D) are apparently shifted to the NO_2-type dispersion for these emission scenarios (not shown). O_3 and O^1D remain invariable in dispersion type in response to the changes in the emission scenarios.

In summary, species in the NO_2-type and O_3-type dispersion generally tend to be classified into the NO_2-type dispersion as the NO_x emission level decreases or the VOC emission level increases. When both NO_x and VOC emission levels change, the effect of decreasing NO_x emission level on concentrations is mostly cancelled out by the effect of decreasing VOC emission level. For example, a typical reactive species would show almost the same vertical concentration profiles for the emission scenario of 1.0 NO_x and 2.0 VOC (S8) and for the emission scenario of 0.5 NO_x and 1.0 VOC (S1). Note that the VOC-to-NO_x emission ratio is equally 2 for these two emission scenarios. Hence, an important factor in determining the dispersion type of any species is the VOC-to-NO_x emission ratio rather than the separate emission level of NO_x or VOC. In the next subsection, we will discuss why the dispersion type depends on the VOC-to-NO_x emission ratio and will identify a key player that leads to the transitions between the dispersion types.

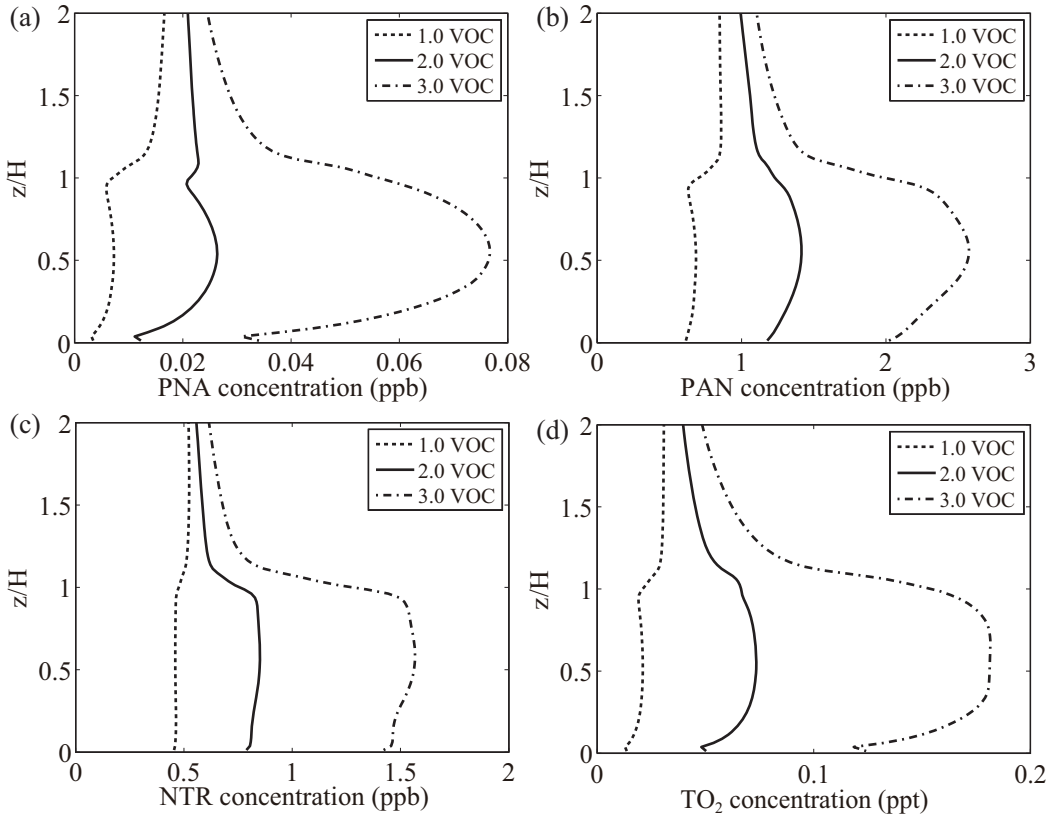

Figure 5.5. Same as Figure 5.4 but for the emission scenarios of 1.0, 2.0, and 3.0 VOC with 1.0 NO_x.

5.3 Hydroxy radical (OH) reactivity

The hydroxyl radical (OH) acts as a detergent in the troposphere. In the urban air, many pollutants such as VOCs and CO react easily with OH, thus initiating subsequent reactions (Sillman, 1999). Jenkin and Clemitshaw (2000) introduced a radical chain to describe the role of radical species such as OH, HO_2, RO, and RO_2 (Figure 5.6). Here, R represents an alkyl-substituted group. In this radical chain, the OH + NO_2 reaction reaction contributes to the propagation of the production of radical species. Therefore, the OH concentration controls the concentrations of other radical species through the OH + NO_2 reaction and the OH + RH reaction.

Figure 5.7 shows the street canyon-averaged OH concentrations as a function of the NO_x (S1–S10) and VOC (S3, S8, S11–S14) emission levels. The street canyon average is taken from $x/H = -0.5$ to 0.5 and from $z/H = 0$ to 1. The OH concentration obviously decreases with increasing NO_x emission level from 0.5 to 1.5. However, the OH concentration almost linearly increases with increasing VOC emission level from 0.5 to 3.0. This dependence of the OH concentration on the NO_x and VOC emission levels, which is consistent with the dependence shown in the diagram of Sillman (1999) for the contributes to the termination of the production of radical species, whereas the OH + RH

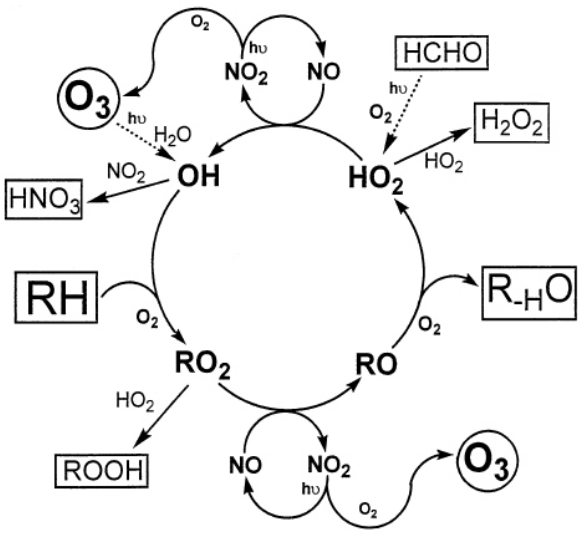

Figure 5.6. Schematic representation of the radical chain propagation process (Jenkin and Clemitshaw, 2000).

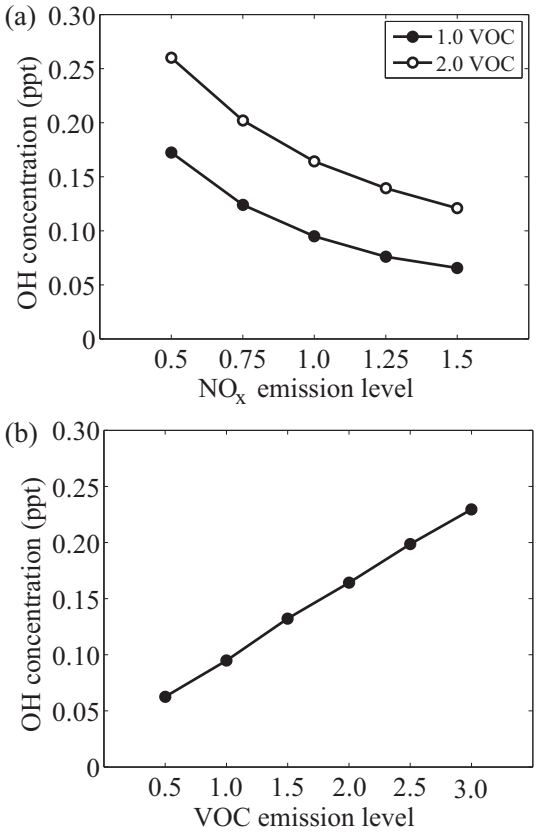

Figure 5.7. Street canyon-averaged OH concentrations for the emission scenarios of (a) from 0.5 to 1.5 NO_x with 1.0 and 2.0 VOC and (b) from 0.5 to 3.0 VOC with 1.0 NO_x.

polluted urban air, can be explained by the radical chain shown in Figure 5.6. An increase in the NO_x emission level enhances the role of the OH + NO_2 reaction to suppress the propagation of the radical chain, thus decreasing OH concentration. On the other hand, an increase in the VOC emission level enhances the role of the OH + RH reaction to promote the propagation of the radical chain, thus increasing OH concentration. In the propagation of the radical chain, decreasing (increasing) OH concentration reduces (raises) the concentrations of other radical species such as HO_2, RO, and RO_2.

Figure 5.8 shows the vertical profiles of the street canyon-width averaged concentrations of OH, HO_2, C_2O_3 and CRO for the emission scenarios of 0.5, 1.0, and 1.5 NO_x with 1.0 VOC (S1, S3, S5). Figure 5.9 is the same as Figure 5.8 but for the emission scenarios of 1.0, 2.0, and 3.0 VOC with 1.0 NO_x (S3, S8, S14). Figures 5.8 and 5.9 verify what we discussed above, showing that the concentrations of HO_2, C_2O_3, and CRO are proportional to the OH concentration, which in turn depends on the NO_x and VOC emission levels. Here, C_2O_3 and CRO are examples of RO_2 and RO, respectively. Note that the concentrations of OH, HO_2, C_2O_3, and CRO decrease with increasing NO_x emission level (Figure 5.8) but increase with increasing VOC emission level (Figure 5.9). Therefore, the VOC-to-NO_x emission ratio controls the propagation of the radical chain through the OH + NO_2 reaction and the OH + RH reaction in opposite ways and hence it

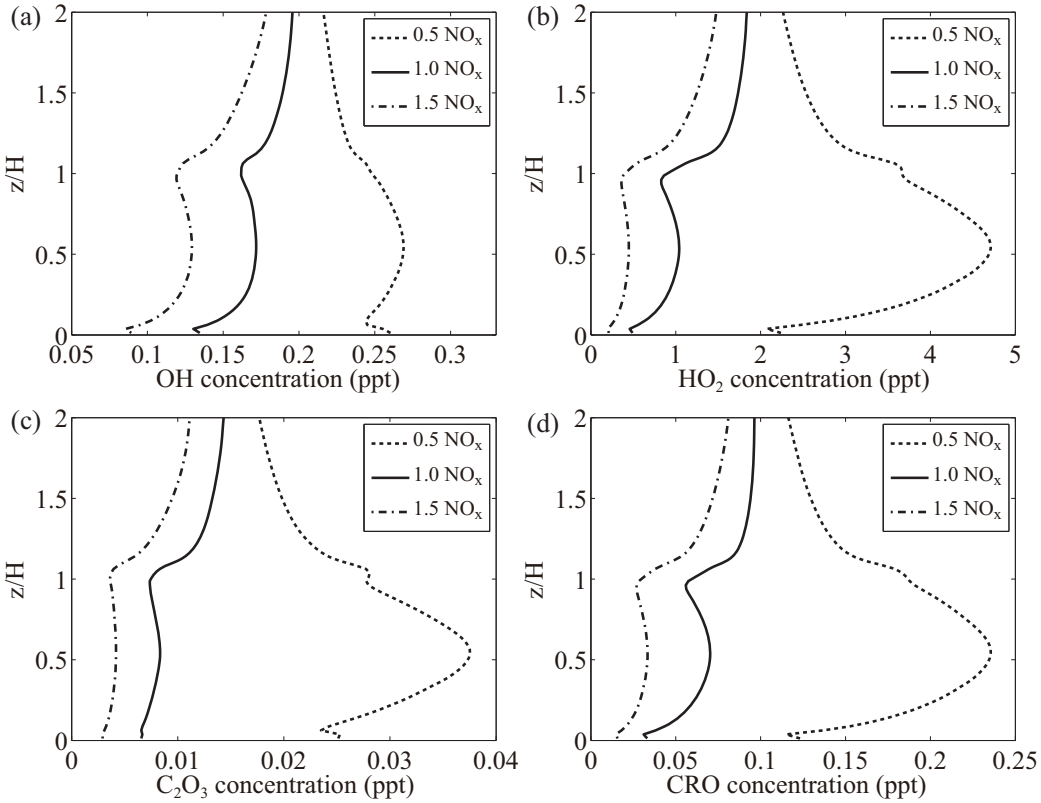

Figure 5.8. Vertical profiles of the street canyon width-averaged concentrations of (a) OH, (b) HO_2, (c) C_2O_3, and (d) CRO for the emission scenarios of 0.5, 1.0, and 1.5 NO_x with 1.0 VOC.

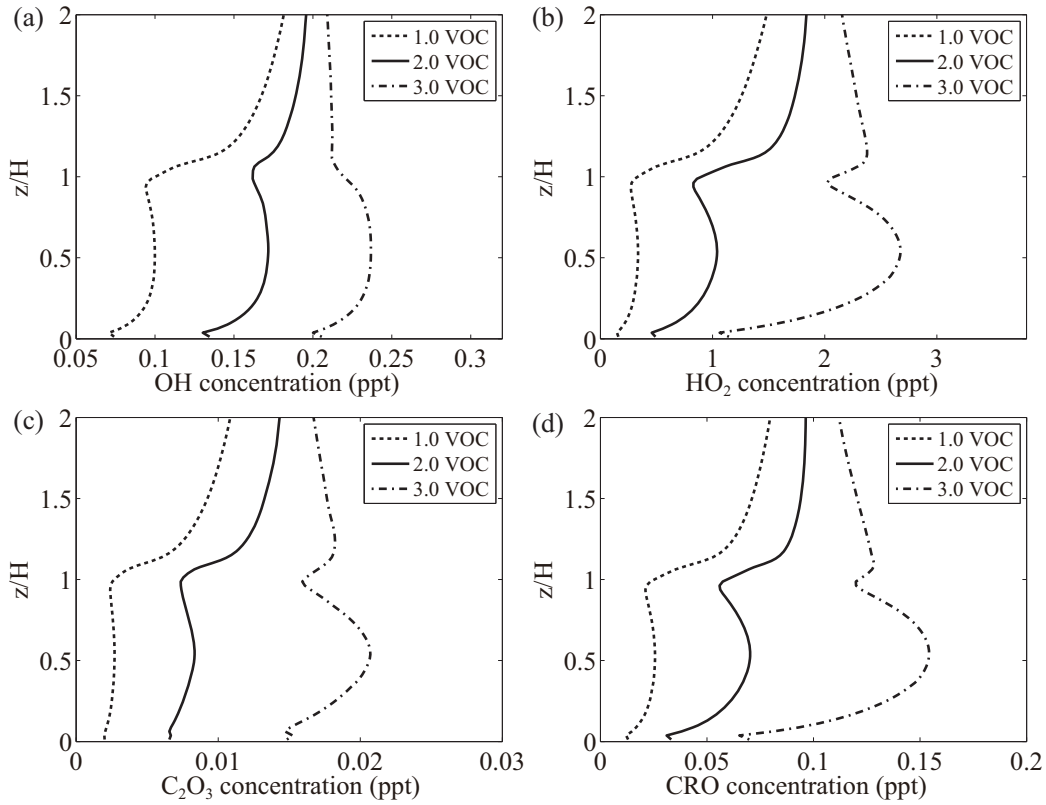

Figure 5.9. Same as Figure 5.8 but for the emission scenarios of 1.0, 2.0, and 3.0 VOC with 1.0 NO_x.

changes the concentrations of radical species and also their products. The changes in concentration are more apparent in the street canyon than above it because of the source location of NO_x and VOC. For this reason, the transitions between dispersion types occur depending on the VOC-to-NO_x emission ratio.

The reactivity of VOC, compared to the total amount of VOC, suitably represents an actual impact of VOC (Sillman, 1999). Understanding the relative reactivity of VOC is essential for measuring its actual effect on the initiation, propagation, and termination of relevant reactions. The OH reactivity (R_i), the reactivity of the *i*th VOC to OH, is calculated using

$$R_i = k_{\mathrm{OH+VOC}_i}[\mathrm{VOC}_i]. \tag{5.1}$$

Here, $k_{\mathrm{OH+VOC}_i}$ is the reaction coefficient between OH and the *i*th VOC and $[\mathrm{VOC}_i]$ is the concentration of the *i*th VOC.

Figure 5.10 shows the pie charts of the street canyon-averaged VOC concentrations and OH reactivities for the emission scenario of 1.0 NO_x and 1.0 VOC (S3). Each relative portion of the VOC concentrations is similar to the corresponding relative portion of the VOC emissions (Figure 5.10a). However, each relative portion of the OH reactivities deviates significantly from the corresponding relative portion of the VOC emissions (Figure 5.10b). Although

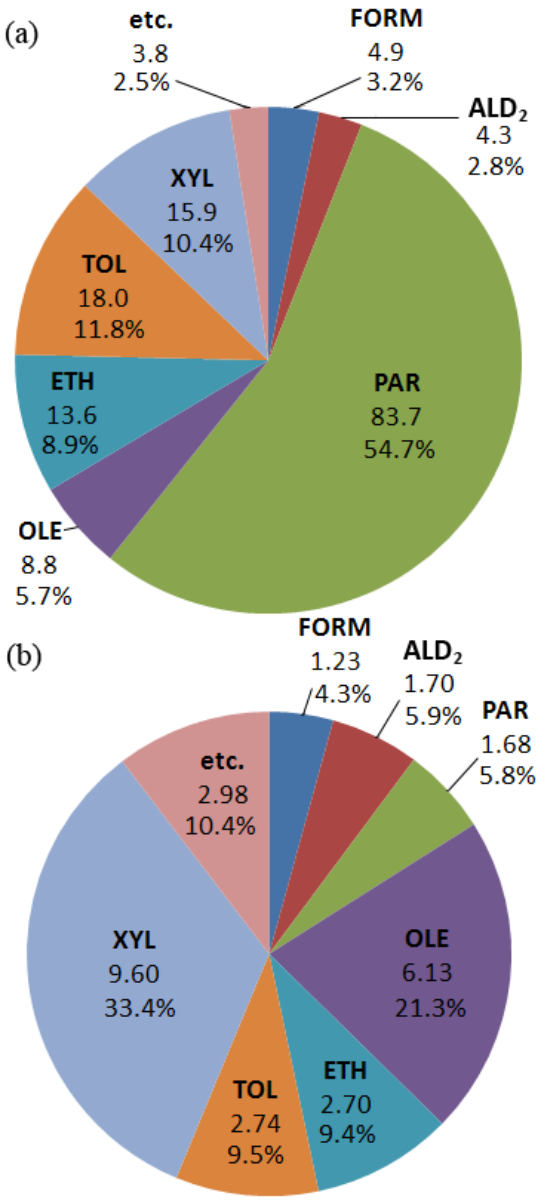

Figure 5.10. Pie charts of the street canyon-averaged (a) concentrations (ppb) and (b) OH reactivities (s^{-1}) of VOCs for the emission scenario of 1.0 NO_x and 1.0 VOC.

PAR (54.7%) is the largest in relative portion of the concentrations, its rank in OH reactivity is sixth because of the small reaction coefficient of the OH + PAR reaction. XYL (33.4%) followed by OLE (21.3%), instead, is the largest in relative portion of the OH reactivities, indicating that XYL and OLE are responsible for more than a half of the total contribution to the OH + RH reaction in the street canyon. This rank in OH reactivity is consistent with the observation of Doraiswamy et al. (2009). They explained that the OH reactivities of ISOP, XYL, and OLE among the VOCs in the CBM–Ⅳ are higher than those of other VOCs at an urban site because the VOCs in the aromatic and olefin groups are highly reactive.

5.4 Ozone (O_3) sensitivity

The O_3 concentration is sensitive to NO_x and VOC emission levels in different ways. Sillman (1999) reviewed two contrasting O_3-precursor relationships, the NO_x-sensitive and the VOC-sensitive chemical regimes. The NO_x-sensitive regime refers to situations in which a percent reduction in NO_x results in a significantly greater decrease in O_3 relative to the same percent reduction in anthropogenic VOC. In contrast, the VOC-sensitive regime refers to situations in which a percent reduction in anthropogenic VOC results in a

significantly greater decrease in O_3 relative to the same percent reduction in NO_x. The O_3–NO_x–VOC sensitivity has been widely studied for urban areas by comparing changes in O_3 concentration resulting from reductions in NO_x and VOC emissions. Previous studies found that the VOC-sensitive regime is general in megacities such as Paris (Deguillaume et al., 2008) and Mexico City (Lei et al., 2007; Song et al., 2010).

As analyzed above, however, the chemical characteristics in a street canyon are distinct from those in broad-scale urban areas because of the proximity of mobile sources. We evaluate O_3–NO_x–VOC sensitivity in the street canyon by comparing the O_3 concentrations of 3 emission scenarios (S1, S3, S11). The diagram of Sillman and West (2009) is used to identify chemical regimes. In the diagram, the location of each grid point in the numerical model is assigned to NO_x-sensitive, VOC-sensitive, mixed, NO_x titration, or no sensitivity regimes.

Following Sillman and West (2009), a scatter diagram of decreases in O_3 concentration due to reduction in NO_x emission level from 1.0 NO_x to 0.5 NO_x [O_3(S3) − O_3(S1) in the ordinate] and due to reduction in VOC emission level from 1.0 VOC to 0.5 VOC [O_3(S3) – O_3(S11) in the abscissa] is plotted in Figure 5.11. Most locations in and above the street canyon belong to the NO_x titration regime based on the definition of Sillman and West (2009). They defined a

location as dominated by the NO_x titration if the O_3 concentration increases by 5 ppb or more in response to reduced NO_x emission and does not decrease by 5 ppb or more in response to reduced VOC emission. In response to reduced NO_x emission level from 1.0 NO_x to 0.5 NO_x, increases in O_3 concentration are significant at all locations in and above the street canyon. These increases range from a few ppb near the street bottom to over 30 ppb near the center of the street canyon. In response to reduced VOC emission level from 1.0 VOC to 0.5 VOC, the locations near the street bottom rarely show changes in O_3 concentration. On the other hand, the locations near the center of the street canyon show comparable decreases in O_3 concentration due to the reduction in VOC emission level.

In the street canyon, where the NO-to-NO_2 ratio exceeds 1, the NO titration is a major sink of O_3 and more pronounced than the NO_2 photolysis. The street canyon-averaged chemical O_3 production is governed primarily by the O + O_2 reaction induced by the NO_2 photolysis. In contrast, the street canyon-averaged chemical O_3 loss is governed primarily by the NO titration and partly by the O_3 photolysis. Compared to the reactions, others are negligible. Although the effect of VOCs on the O_3 concentration is important through the radical chain, NO_x strongly affects O_3 not only by means of the radical chain but also by means

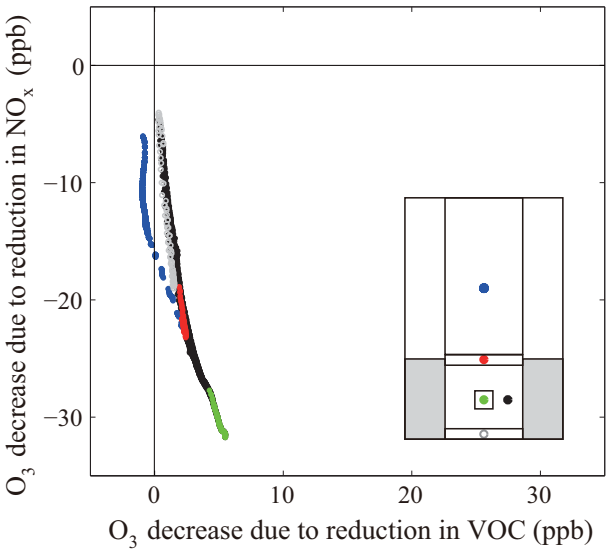

Figure 5.11. Scatter diagram of decreases in O_3 concentration due to 50% reduction in NO_x (O_3 decrease due to NO_x) or VOC emission (O_3 decrease due to VOC). Note that negative values in O_3 decrease due to NO_x or VOC mean O_3 increases due to NO_x or VOC. Individual dots for each of the five different filled and open circles in the diagram correspond to grid points for each of the five different regions of the computational domain (inset).

of the NO titration. Consequently, the street canyon is a negatively NO_x-sensitive regime because of freshly emitted NO from mobile sources.

6 Reactive Pollutant Dispersion in and above a Street Canyon with Different Canyon Aspect Ratios

6.1 Experimental setup

Figure 6.1 depicts the computational domain and street canyon configuration. The street canyon width (W) is 20 m, and the building height (H) considered is 20 m and 40 m. Thus, the street canyon aspect ratio (H/W) considered is 1 and 2. The domain size is 40 m × 60.1 m for H/W = 1 and 40 m × 100 m for H/W = 2. The grid interval in the x-direction is 0.5 m, and the grid interval in the z-direction is 0.5 m up to z = 32 m for H/W = 1 and z = 68.5 m for H/W = 2. Above these heights, an expansion ratio of 1.1 is applied to the grid interval in the z-direction. The ambient wind blows in the positive x-direction, and the ambient wind speed is vertically uniform at the inflow boundary. Turbulent kinetic energy and its dissipation rate at the inflow boundary are also vertically uniform based on the ambient wind speed. The air temperature is set to be 298 K (isothermal condition). For concentrations of reactive species, cyclic boundary conditions are applied at the inflow and outflow boundaries. Nine emission species (NO, NO_2, and 7 VOCs) are emitted at the lowest model level (z = 0.25 m) in the street canyons. The 7 VOCs are FORM (formaldehyde),

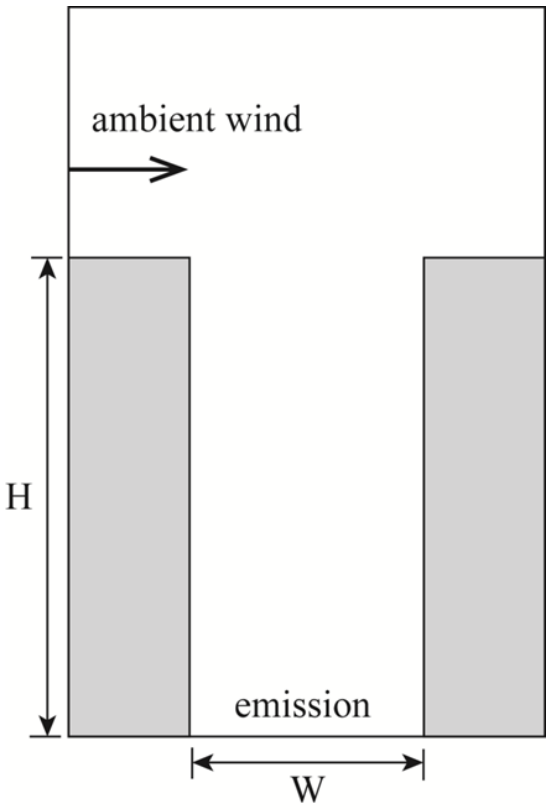

Figure 6.1. Description of computational domain and buildings. *H* is the building height and *W* is the street canyon width.

ALD_2 (high molecular weight aldehydes), PAR (paraffin carbon bond), OLE (olefin carbon bond), ETH (ethene), TOL, and XYL. The relative portion between NO and NO_2 emission rates is 9:1. As in Kwak and Baik (2012), the relative portions of the emission rates of the 7 VOCs are 56.3% for PAR, 12.4% for TOL, 11.9% for XYL, 9.5% for ETH, 6.7% for OLE, 2.1% for ALD_2, and 1.1% for FORM (Smylie et al., 1991; Bossioli et al., 2002).

An experiment is performed for $H/W = 1$. Fifteen experiments for $H/W = 2$ are performed to examine sensitivities to NO_x and VOC emission rates, photolysis rate, and ambient wind speed. Four different emission rates of NO_x and the 7 VOCs (1, 2, 4, and 6 ppb s^{-1} per grid cell), five different reductions in all photolysis rates (0, 20, 40, 60, and 80%), and five different ambient wind speeds (3, 4, 5, 6, and 7 m s^{-1}) are considered for $H/W = 2$. A case with NO_x and VOC emission rates of 2 ppb s^{-1} per grid cell, no reduction in photolysis rate, and an ambient wind speed of 5 m s^{-1} is selected as the control experiment. In addition to the fifteen experiments, one additional experiment that is the same as the control experiment but with the chemistry-off is performed. The CFD model is integrated for 120 min with a time step of 0.1 s. Emission and chemical processes are off for the first 30 and 60 min, respectively. For analysis, simulation data are averaged from $t = 90$ to 120 min.

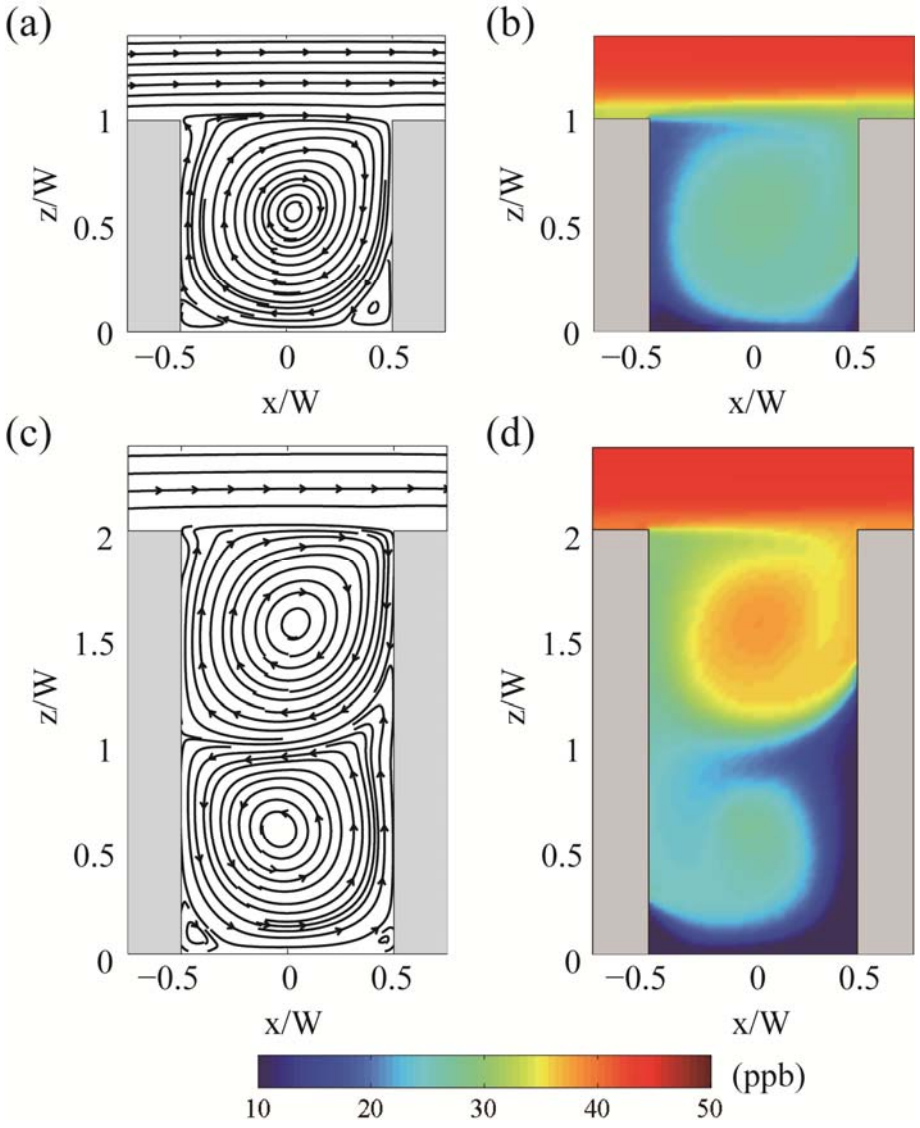

Figure 6.2. (a, c) Streamline and (b, d) O_3 concentration fields in the street canyons with canyon aspect ratios of 1 (upper panels) and 2 (lower panels).

6.2 Ozone (O_3) dispersion and chemistry

Many previous CFD modeling studies have shown that in street canyons O_3 is markedly depleted by NO (Baker et al., 2004; Baik et al., 2007; Garmory et al., 2009; Kwak and Baik, 2012). Kwak and Baik (2012) examined the O_3 sensitivity to precursors and concluded that the street canyon with an aspect ratio of 1 is a negatively NO_x-sensitive regime because of freshly emitted NO from mobile sources. However, it is not clear whether O_3 is always chemically reduced due to the NO titration of O_3 in a street canyon or not. In the first part of this study, we focus on O_3 chemical production and reduction in street canyons.

Figure 6.2 shows the streamline and O_3 concentration fields in the H/W = 1 and 2 street canyons. In the H/W = 1 street canyon, a primary vortex and secondary corner vortices appear. In association with the primary vortex circulation, the O_3 concentration is lower than 20 ppb near the street bottom and the upwind building wall. In the H/W = 2 street canyon, two counter-rotating vortices, that is, a clockwise-rotating upper vortex and a counterclockwise-rotating lower vortex, appear. In association with these vortices circulation, the O_3 concentration is lower than 20 ppb near the street bottom and the lower part of the downwind building wall. In the upper region of the street canyon, the O_3 concentration is generally higher than the initial O_3 concentration (30 ppb). An air mass in the lower region of the street canyon is directly affected by emission,

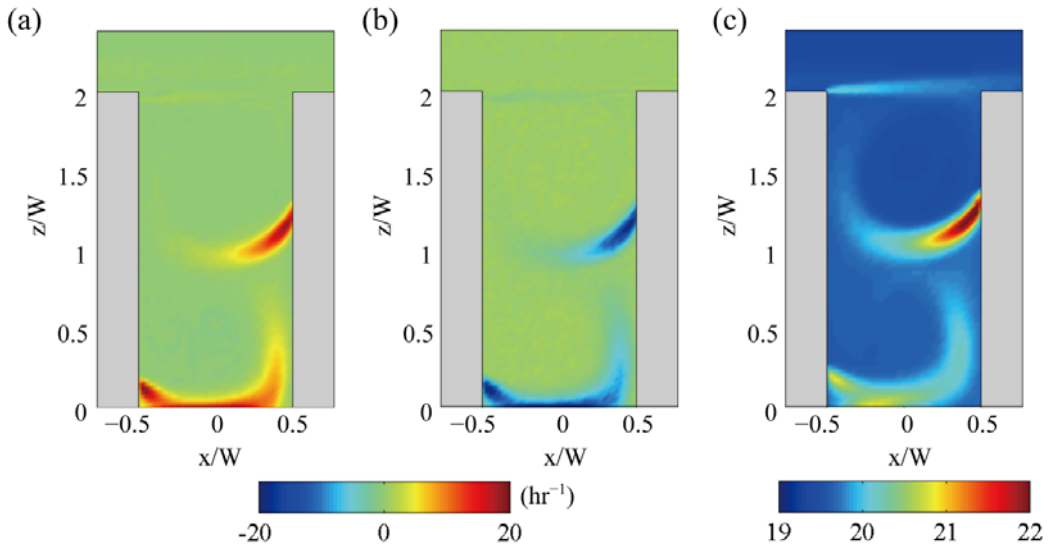

Figure 6.3. Scatter plots of O_3 chemical production rate divided by O_3 concentration at corresponding grid point with (a) $t_{NO_x}/t^{bg}{}_{NO_x}$ and (b) $t_{VOC}/t^{bg}{}_{VOC}$. Closed and open circles indicate grid points in the lower and upper regions of the street canyon with a canyon aspect ratio of 2, respectively.

which is similar to that in the H/W = 1 street canyon. On the other hand, an air mass in the upper region of the street canyon is largely affected by the background air across the roof level. In addition, air masses in the lower and upper regions of the street canyon are likely to be isolated from each other due to the counter-rotating vortices circulation. As a result, the O_3 chemical characteristics in the lower region of the street canyon can be different from those in the upper region of the street canyon.

Figure 6.3 shows the fields of O_3 transport (advection plus turbulent diffusion in this study) rate and O_3 chemical production rate, which are divided by O_3 concentration, and the field of the photo-stationary state (= $[NO][O_3]/[NO_2]$). When the chemical equilibrium among NO, NO_2, and O_3 is satisfied, the photo-stationary state is equivalent to J_{NO_2} / k_{NO+O_3}. The chemical instability is large near the street bottom and the mid-level of the downwind building wall. In these two regions, O_3 is reduced chemically but is produced at almost equal rates owing to transport. Near the street bottom, O_3 is depleted by freshly emitted NO. The O_3 transport following the lower vortex compensates for this O_3 depletion. Near the mid-level of the downwind building wall, NO is transported upward following the lower vortex and O_3 is transported downward following the upper vortex. Both rich NO and O_3 accelerate the O_3 depletion there and result in a large deviation from the chemical equilibrium.

6.3 Photochemical characteristics in different regions of street canyons

To quantitatively compare each contribution in AR1, AR2, AR2L, and AR2U, the area-averaged emission, transport, chemical production, and total (= emission + transport + chemical production) rates of NO, NO_2, O_3, XYL, FORM, and OH divided by their area-averaged concentrations are calculated (Figure 6.4). NO and XYL that are emitted species at the street bottom are chemically reduced and transported upward in AR1 and AR2L. The large amounts of the transported NO and XYL remaining in AR2U are chemically reduced. On the other hand, NO_2 and FORM that are emitted species at the street bottom are chemically produced and transported upward in AR1 and AR2L. The chemical production rates of NO_2 and FORM are even larger than their emission rates averaged over the regions. In AR2U, the chemical production of NO_2 and FORM is more pronounced than their transport. Overall, the total rates of NO_2 and FORM are positively significant in all regions. O_3 is transported downward across the roof level in both AR1 and AR2. Whereas the transported O_3 is chemically reduced in AR1 and AR2L, O_3 is chemically produced in AR2U. This means that the NO titration of O_3 is less pronounced than the NO_2 photolysis in AR2U where the air

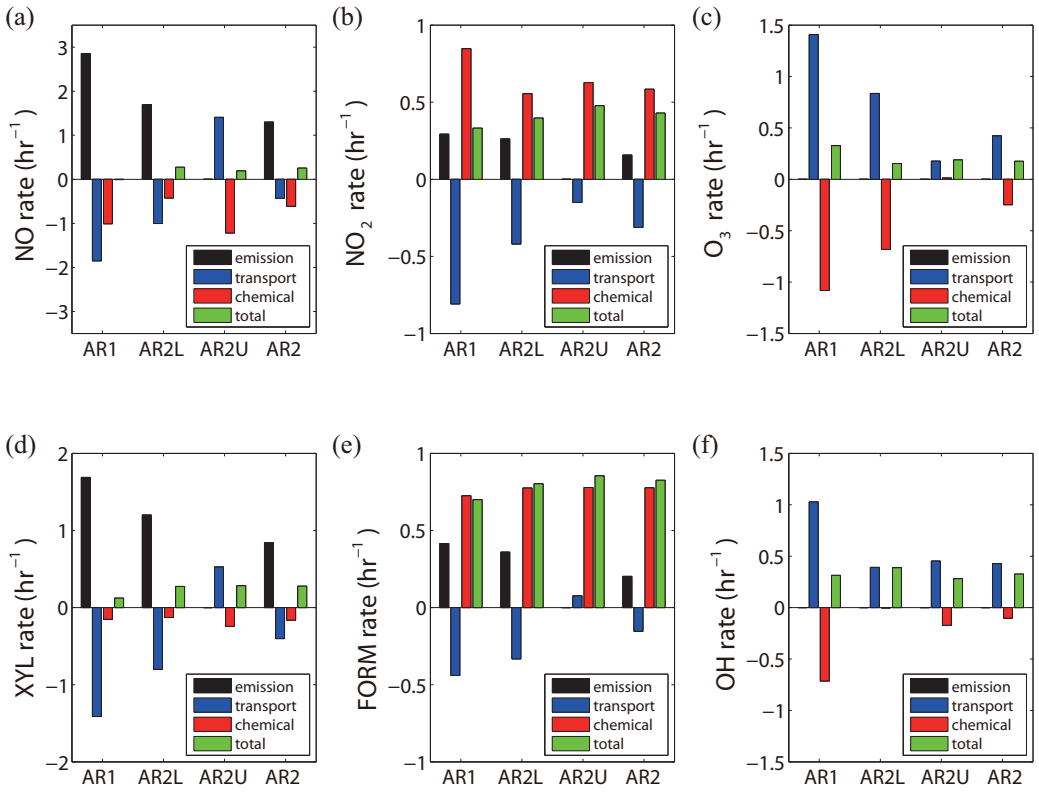

Figure 6.4. Averaged emission, transport, chemical production, and total rates of (a) NO, (b) NO_2, (c) O_3, (d) XYL, (e) FORM, and (f) OH divided by their averaged concentrations in the street canyons with canyon aspect ratios of 1 (AR1) and 2 (AR2) and the lower (AR2L) and upper (AR2U) regions of the street canyon with a canyon aspect ratio of 2.

is more aged than in AR1 and AR2L. OH is also transported downward across the roof level in both AR1 and AR2, while its chemical production rate is always negative.

6.4 Sensitivity to environmental conditions

In the control experiment, it was found that O_3 can be chemically produced in AR2U as well as transported downward across the roof level. The O_3 chemical production can be affected by conditions such as NO_x and VOC emission rates, photolysis rate, and ambient wind speed. Sensitivities to such conditions are examined for $H/W = 2$.

Figure 6.5 shows area-averaged O_3 concentrations and area-averaged O_3 rates divided by the area-averaged O_3 concentrations at different NO_x and VOC emission rates. The O_3 concentration decreases with increasing NO_x emission rate but increases with increasing VOC emission rate in both AR2L and AR2U. For example, the O_3 concentration decreases by 9.0 ppb in AR2L and 10.0 ppb in AR2U when the NO_x emission rate increases from 2 to 4 ppb s^{-1}. On the other hand, the O_3 concentration increases by 5.5 ppb in AR2L and 5.0 ppb in AR2U when the VOC emission rate increases from 2 to 4 ppb s^{-1}. The O_3 concentration changes are better attributed to the changes in chemical production rate than

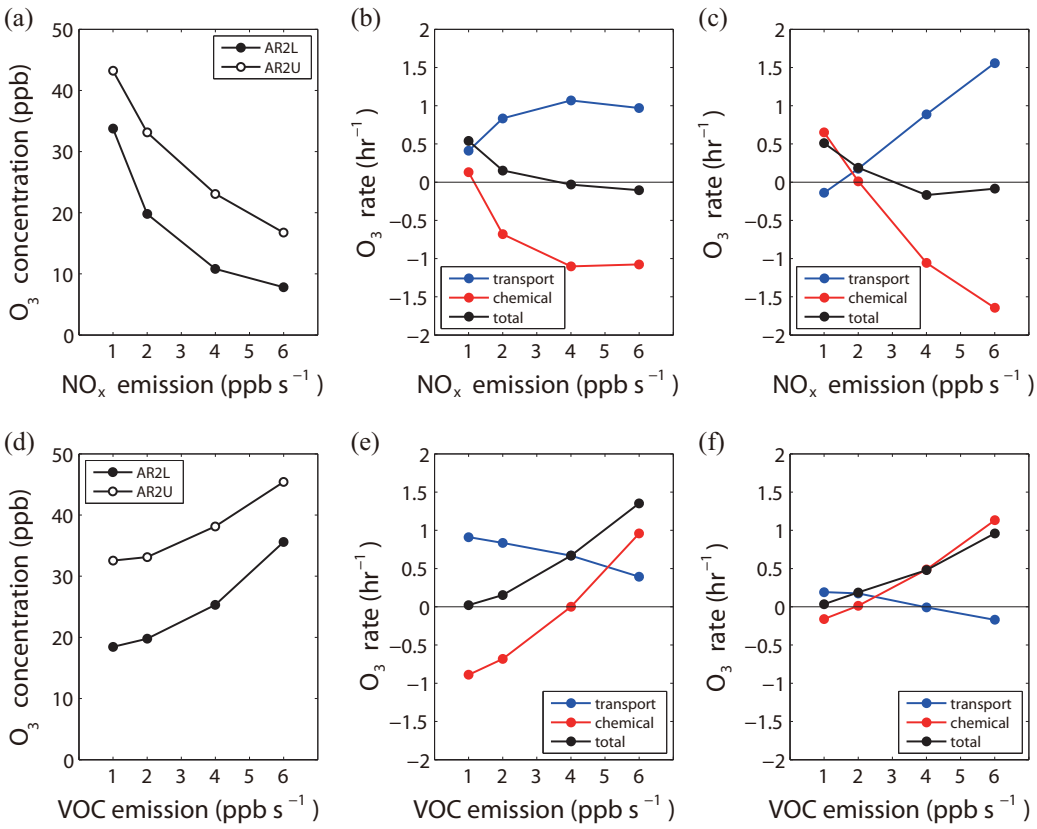

Figure 6.5. Averaged O_3 concentrations (left panels) and averaged O_3 transport, chemical production, and total rates divided by the averaged O_3 concentrations in AR2L (middle panels) and AR2U (right panels) at different (a–c) NO_x and (d–f) VOC emission rates.

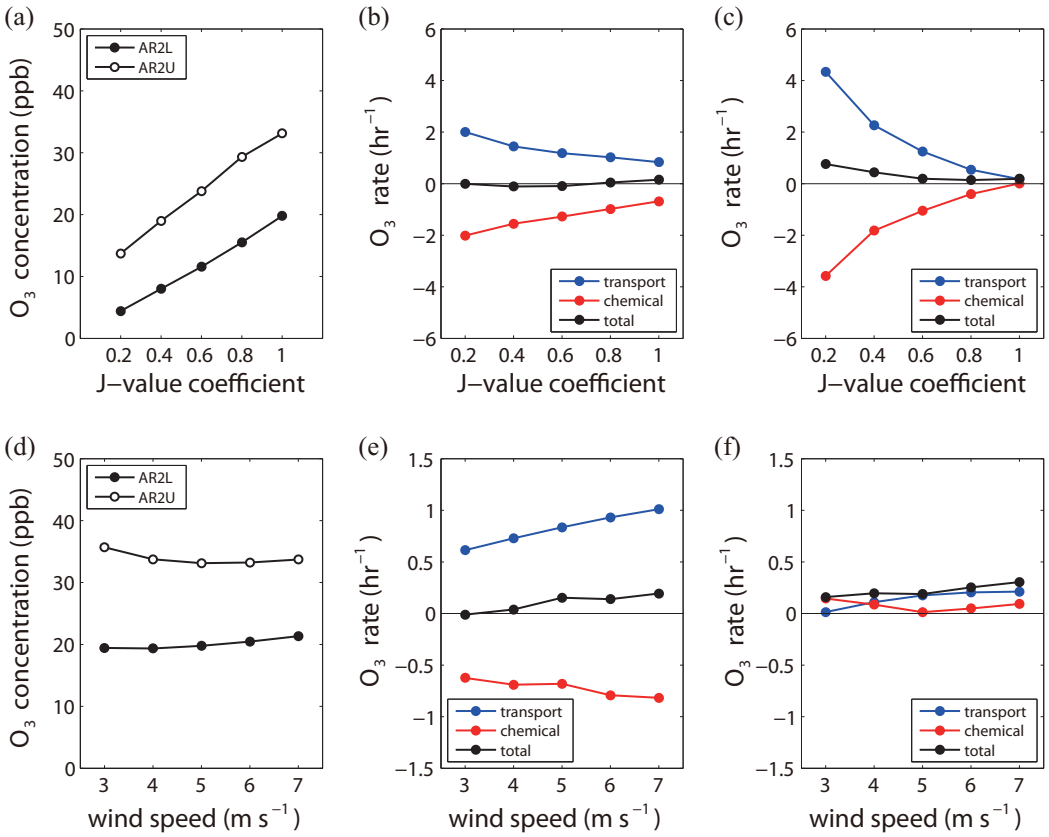

Figure 6.6. Same as Figure 6.5 but at different (a–c) photolysis rates and (d–f) ambient wind speeds.

those in transport rate. When the NO_x emission rate increases from 2 to 4 ppb s^{-1}, the O_3 chemical production rate decreases from −0.68 to −1.10 hr^{-1} in AR2L and from 0.01 to −1.06 hr^{-1} in AR2U. When the VOC emission rate increases from 2 to 4 ppb s^{-1}, the O_3 chemical production rate increases from −0.68 to −0.001 hr^{-1} in AR2L and from 0.01 to 0.50 hr^{-1} in AR2U. Although the changes in O_3 transport rate partially compensate for the changes in O_3 chemical production rate, the total rates generally follow the O_3 chemical production rates. A positive O_3 chemical production rate is favorable when the NO_x emission rate is 1 ppb s^{-1} or the VOC emission rate is 6 ppb s^{-1} in AR2L but when the NO_x emission rate is 1 and 2 ppb s^{-1} or the VOC emission rate is 2, 4, and 6 ppb s^{-1} in AR2U. This result agrees with the result of Liu and Leung (2008) that high levels of O_3 would occur in street canyons when the ratio of VOC emission rate to NO_x emission rate is high.

Figure 6.6 shows area-averaged O_3 concentrations and area-averaged O_3 rates divided by the area-averaged O_3 concentrations at different photolysis rates and ambient wind speeds. Here, a J-value coefficient of 0.2 denotes an 80% reduction in photolysis rate and a J-value coefficient of 1.0 denotes no reduction in photolysis rate. The O_3 concentration decreases with decreasing J-value coefficient. For example, the O_3 concentration decreases by 8.2 ppb in AR2L and

9.3 ppb in AR2U when the J-value coefficient decreases from 1.0 to 0.6. Reducing the photolysis rate causes the NO_2 photolysis to be less pronounced than the NO titration of O_3, resulting in a decreased O_3 chemical production rate in the street canyon. When the J-value coefficient decreases from 1.0 to 0.6, the O_3 chemical production rate decreases from −0.68 to −1.28 hr^{-1} in AR2L and from 0.01 to −1.05 hr^{-1} in AR2U. A positive O_3 chemical production rate is not favorable in AR2L but only favorable in AR2U when the J-value coefficient is 1.0. It is interesting that the sensitivities of O_3 concentration and rate to the J-value coefficient are larger in AR2U than in AR2L. This may indicate more active photolysis processes in the more aged air than in the less aged air.

The sensitivity of O_3 concentration to the ambient wind speed is relatively small. The O_3 concentration slightly increases with increasing ambient wind speed in AR2L but varies very little in the ambient wind speed ranging from 4 to 7 m s^{-1} in AR2U. Increasing ambient wind speed enhances the mixing process in the street canyon, resulting in strengthened upward transport of emitted pollutants and strengthened downward transport of O_3. When the ambient wind speed increases from 4 to 6 m s^{-1}, the O_3 transport rate increases from 0.73 to 0.93 hr^{-1} in AR2L and from 0.11 to 0.20 hr^{-1} in AR2U. A positive O_3 chemical production rate is not favorable in AR2L but always favorable in

AR2U. The total rate generally follows the O_3 transport rate, while the contribution of O_3 transport to the O_3 concentration is not significant.

7 Diurnal Variation of NO_x and Ozone between a Street Canyon and the Overlying Air

7.1 Formation of vertical transport

The transport equation of a species is expressed as

$$\frac{\partial C_i}{\partial t} + U_j \frac{\partial C_i}{\partial x_j} = D \frac{\partial^2 C_i}{\partial x_j \partial x_j} + \frac{\partial}{\partial x_j}\left(K_c \frac{\partial C_i}{\partial x_j} \right) + \left[\frac{\partial C_i}{\partial t} \right]_{chem} + \left[\frac{\partial C_i}{\partial t} \right]_{depo}. \quad (7.1)$$

Here, C_i is the mean concentration of the *i*th species, U_j is the *j*th mean velocity component, D is the molecular diffusivity of the species, and K_c is the eddy diffusivity of the species. The last two terms on the right hand side of Eq. (7.1) are the net chemical production term of the species calculated by the CBM–Ⅳ and the dry deposition loss term of the species, respectively. The dry deposition loss term is calculated by

$$\left[\frac{\partial C_i}{\partial t} \right]_{depo} = -\frac{V_{d,i}}{\Delta} C_i, \quad (7.2)$$

where $V_{d,i}$ and Δ are the deposition velocity and the distance from the surface, respectively (Pugh et al., 2012). This term is only activated at the grid points nearest to the surfaces.

The vertical mean flux of the *i*th species ($F_{m,i}$) and the vertical turbulent flux of the *i*th species ($F_{t,i}$) are calculated using

$$F_{m,i} = C_i W , \tag{7.3}$$

$$F_{t,i} = \overline{c_i w} = -K_c \frac{\partial C_i}{\partial z} . \tag{7.4}$$

Here, W is the mean vertical velocity, c_i is the deviation from C_i, and w is the deviation from W. The vertical mean and turbulent fluxes are calculated and analyzed for NO_x and O_3 to examine the NO_x removal and O_3 entrainment in a street canyon.

7.2 Formulation of exchange velocity

The exchange velocity is defined as the spatially averaged mass exchange between a canyon and the overlying air (Bentham and Britter, 2003;

Solazzo and Britter, 2007), which is different from the transfer velocity that reflects the mass transfer from a source at a surface to a canyon or the overlying air (Barlow and Belcher, 2002). The exchange velocity is used as a parameter measuring pollutant exchange between a street canyon and the overlying air. The exchange velocity of the *i*th species (ω_i) can be calculated using

$$\omega_i = \frac{\langle F_i \rangle}{C_{\mathrm{C},i} - C_{\mathrm{B},i}}, \tag{7.5}$$

where $F_i = F_{\mathrm{m},i} + F_{\mathrm{t},i}$. (7.6)

Here, F_i is the total vertical flux of the *i*th species, $C_{\mathrm{C},i}$ is the concentration of the *i*th species averaged inside the street canyon, and $C_{\mathrm{B},i}$ is the background concentration of the *i*th species. $\langle\ \rangle$ denotes the horizontal average at the roof level of the street canyon. The exchange velocity can be rewritten in terms of each flux component by substituting Eq. (7.6) into Eq. (7.5):

$$\omega_{\mathrm{m},i} = \frac{\langle F_{\mathrm{m},i} \rangle}{C_{\mathrm{C},i} - C_{\mathrm{B},i}}, \tag{7.7}$$

$$\omega_{\mathrm{t},i} = \frac{\langle F_{\mathrm{t},i} \rangle}{C_{\mathrm{C},i} - C_{\mathrm{B},i}}. \tag{7.8}$$

Here, $\omega_{m,i}$ and $\omega_{t,i}$ are the mean and turbulent exchange velocities of the *i*th species, respectively. When the concentration of a species, such as NO_x, is higher in the street canyon than in the background, both the turbulent vertical flux and the concentration difference in Eq. (7.8) are positive. On the other hand, when the concentration of a species, such as O_3, is higher in the background than in the street canyon, both the turbulent vertical flux and the concentration difference in Eq. (7.8) are negative. Thus, the turbulent exchange velocity calculated using Eq. (7.8) is always positive regardless of species.

7.3 Validation

An additional validation for transfer velocity is performed against the wind tunnel experiment data of Barlow et al. (2004). In the wind tunnel experiments, transfer velocities with different inflow wind speeds were obtained in street canyons under an isothermal condition using the naphthalene sublimation technique. In the simulations, the emission of passive scalar is modeled using the wall function for scalar described in Cai et al. (2008) when dry deposition process is not considered. Figure 7.1 shows the transfer velocities in the street canyon with a canyon aspect ratio of 1 as a function of inflow wind

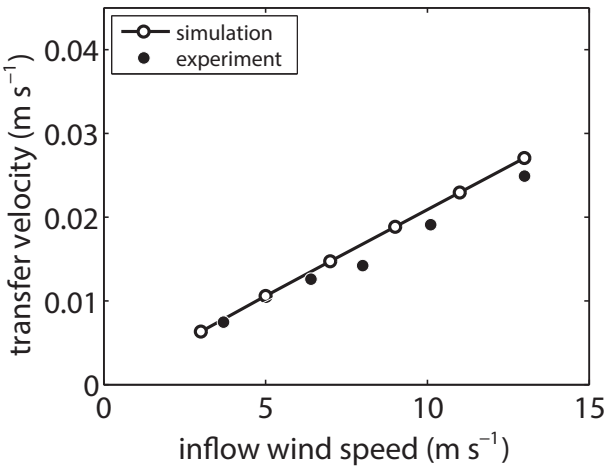

Figure 7.1. Transfer velocities estimated in the simulations (open circle) and in the wind tunnel experiments (closed circle) as a function of inflow wind speed.

speed when the source of passive scalar is located at the road. The linear relationship between the transfer velocity and the inflow wind speed is reasonably well reproduced by the CFD model. The transfer coefficient (i.e., the transfer velocity normalized by the inflow wind speed) is estimated using the slope of the linear regression with a zero offset in Figure 7.1. The transfer coefficient in the simulations (0.00208) is slightly larger than that in the wind tunnel experiments (0.00192), which is acceptable compared to 0.00179 obtained by Cai et al. (2008) and 0.00213 obtained by Cheng and Liu (2011). The deviation in transfer coefficient is to some extent attributed to uncertainties in the representation of emission and/or inflow wind profile.

7.4 Experimental setup

A two-dimensional (2-D) idealized street canyon is considered (Figure 7.2). The building height (H) is 20 m and the street canyon width (W) is 20 m, giving a canyon aspect ratio (H/W) of 1. The grid interval in the x-direction is 0.5 m, and the grid interval in the z-direction is uniformly 0.5 m up to z = 32 m and then increases with an expansion ratio of 1.1. The computational domain size is 40 m in the x-direction and 60.1 m in the z-direction. The inflow wind blows in the x-direction, and constant wind speed (= 3 m s^{-1}) and turbulent kinetic energy (= 0.11 m^2 s^{-2}) are set to be vertically uniform at the inflow boundary to remove

the arbitrariness of inflow profiles especially for the estimation of exchange velocity (Solazzo and Britter, 2007). We selected 18 June 2007 (the same day as in Kwak et al. (2011)) in Seoul, South Korea, for estimating the sky radiation. The ambient air temperatures at the inflow boundary are the same as the observed air temperatures during the day. For a detailed description of the thermal properties of surfaces and substrates, see Kwak et al. (2011). The zero gradient boundary condition is applied at the outflow and upper boundaries.

In this study, the diurnal variations of inflow concentrations and pollutant emission rates as well as inflow wind speed are neglected to isolate the effects of diurnally varying surface heating. The initial and inflow concentrations are 10 ppb for NO, 30 ppb for NO_2, 30 ppb for O_3, 200 ppb for CO, and 41 ppb in total for 7 VOCs that are FORM (formaldehyde), ALD_2 (high molecular weight aldehydes), PAR (paraffin carbon bond), OLE (olefin carbon bond), ETH (ethene), TOL (toluene), and XYL (xylene). NO_x, CO, and the 7 VOCs are emitted at the lowest model level ($z/H = 0.0125$). The emission rate of NO_x is 2 ppb s^{-1} (equivalent to 0.64 μg s^{-1}) per a grid point, the relative portion of NO_x emission rate in the unit of ppb s^{-1} is 9:1 ($NO:NO_2$). The emission rate of the total 7 VOCs is also 2 ppb s^{-1} per a grid point, the relative portions of the 7 VOCs emission rates in the unit of ppb s^{-1} are 56.3% for PAR, 12.4% for TOL, 11.9% for XYL, 9.5% for ETH, 6.7% for OLE, 2.1% for ALD_2, and 1.1% for

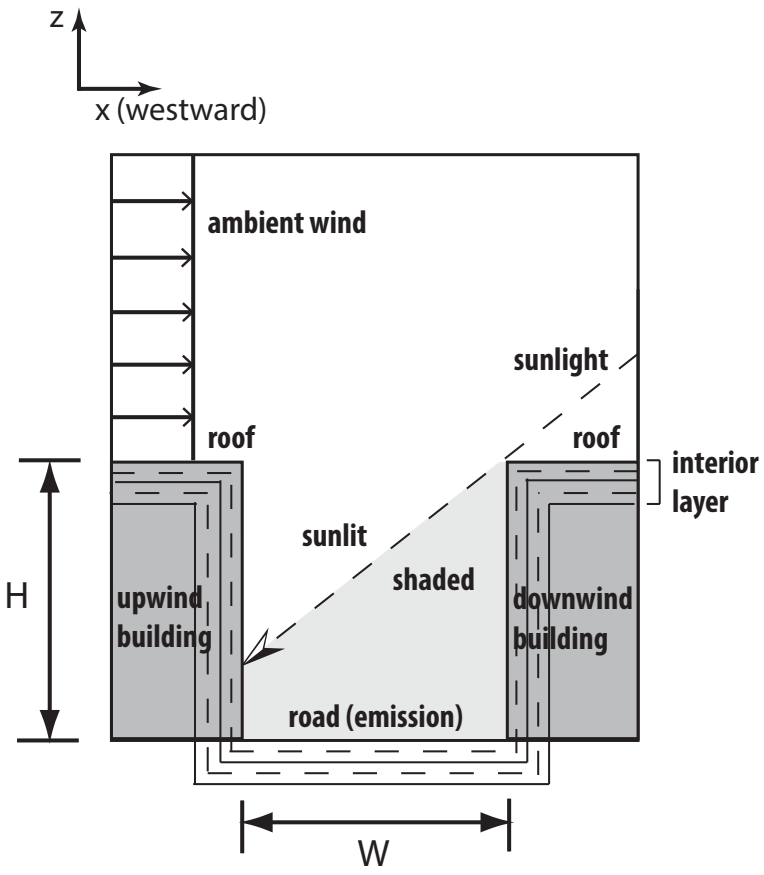

Figure 7.2. Illustration of building and street canyon configuration. The street canyon is divided into sunlit and shaded spaces. *H* is the building height, and *W* is the street canyon width.

FORM (Bossioli et al., 2002; Kwak and Baik, 2012). The emission rate of CO is ten times larger than that of NO_x. The model is integrated for 24 h with a dynamics time step of 0.1 s and a chemistry time step of 1 s.

The shading effect on photochemistry is included by separating a canyon space into a sunlit space and a shaded space based on the direct shortwave radiation reaching the surfaces in the street canyon (Figure 7.2). The shortwave radiation in a sunlit space consists of direct, diffuse, and reflected radiation, whereas the shortwave radiation in a shaded space consists of diffuse and reflected radiation. Photolysis rate coefficients obtained from Jacobson (2005) are then modified in proportion to the sum of shortwave radiation in each space at every time step.

Dry deposition process is included by calculating deposition fluxes for reactive species at all surfaces (e.g., Kim et al., 2012). Assuming no vegetation at surfaces, the deposition velocity that is constant over all surfaces is 0.063 cm s^{-1} for NO_2, 0.12 cm s^{-1} for O_3, and 8 cm s^{-1} for HNO_3 (Grøntoft and Raychaudhuri, 2004; Aikawa et al., 2005). The deposition velocity for other reactive species is identically 0.012 cm s^{-1}.

7.5 Surface temperature and streamline field

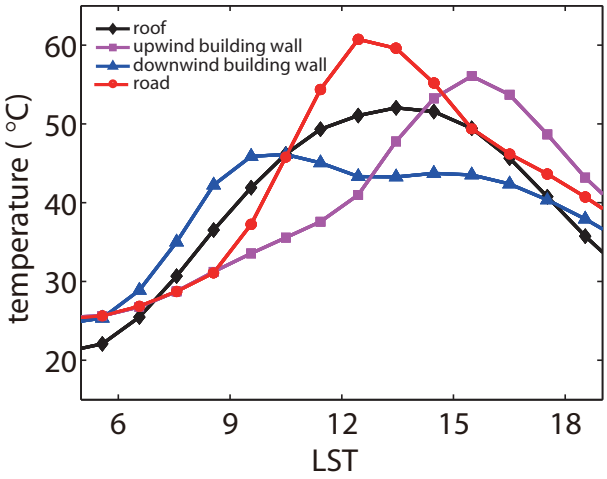

Figure 7.3. Diurnal variations of hourly averaged surface temperatures of roof, upwind building wall, downwind building wall, and road.

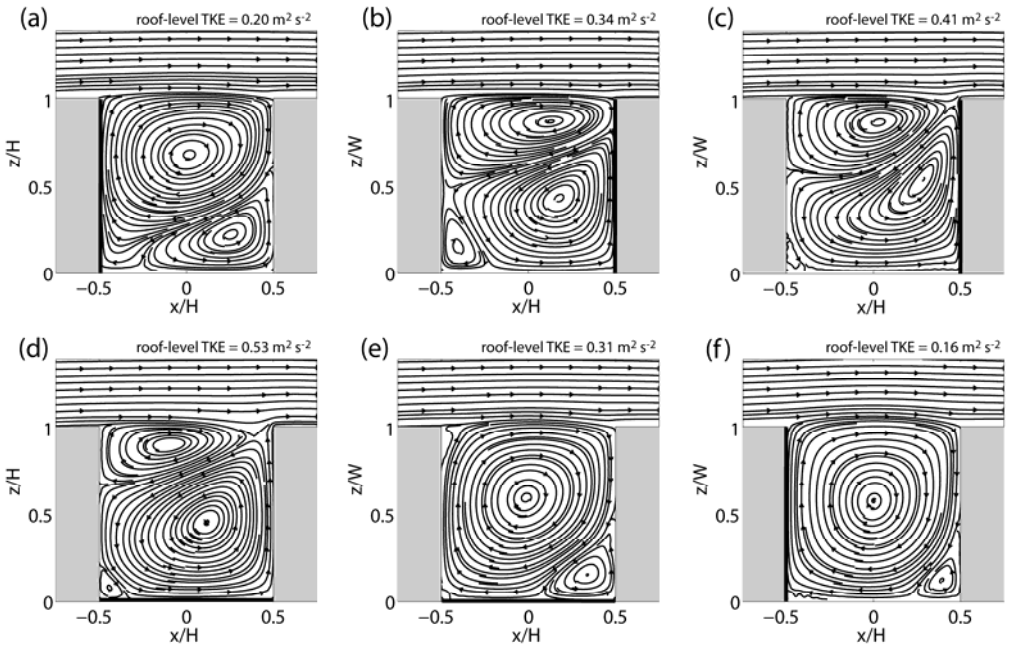

Figure 7.4. Streamline fields at (a) 0500, (b) 0700, (c) 0900, (d) 1100, (e) 1300, and (f) 1500 LST. Bold lines indicate the surfaces with the highest temperature. The roof-level averaged turbulent kinetic energy (TKE) is given on the top of each figure.

The diurnal variations of surface temperatures and streamline field are analyzed and compared with those in the three-dimensional (3-D) simulation of Kwak et al. (2011). Figure 7.3 shows the diurnal variations of surface temperatures of roof, upwind building wall, downwind building wall, and road. The surface temperature of the downwind building wall is higher than that of the upwind building wall in the morning (from 0630 to 1230 LST), while the surface temperature of the upwind building wall is higher than that of the downwind building wall in the afternoon (from 1330 LST). The maximum surface temperature (60.8°C at 1230 LST) appears at the road, and the temperature difference between the road surface and the canyon air is 18.9°C at the same time. Although the diurnal patterns are quite similar to those in Kwak et al. (2011), the surface temperatures in this study are slightly higher than those in the previous study by up to 4.8°C (road). This is because the heated air is less mixed with the ambient air in this 2-D simulation than in the 3-D simulation.

Figure 7.4 shows streamline fields in 2-h intervals from 0500 to 1500 LST. The upper vortex is larger than the lower vortex at 0500, 1300, and 1500 LST, which was classified into flow regime I in the previous study. On the other hand, the lower vortex is larger than the upper vortex at 0900 and 1100 LST, which was classified into flow regime II in the previous study. The transition of flow regime from I to II is captured at 0700 LST, showing three vortices that

includes a small vortex with a considerable size near the upwind building wall. Compared to the previous study, the lower vortex tends to be more expanded especially at 0500, 0700, and 1300 LST because the heated air is less mixed with the ambient air in this 2-D simulation. The roof-level averaged turbulent kinetic energy is obviously higher in flow regime II (e.g., 0.53 m^2 s^{-2} at 1100 LST) than in flow regime I (e.g., 0.16 m^2 s^{-2} at 1500 LST). It is observed that the flow near the roof level where we mainly focus on is similar to that in the previous study. Based on the understanding of the diurnal variation of flow, the diurnal variation of NO_x and O_3 exchange at the roof level is presented and discussed in the next subsection.

7.6 Vertical transport

The vertical transport by mean and turbulent flow at the roof level is the responsible mechanism for pollutant removal from a street canyon and pollutant entrainment into a street canyon. To examine the horizontal and temporal distributions of NO_x transport by mean and turbulent flow, the vertical mean and turbulent NO_x fluxes at the roof level are shown in Figure 7.5. In flow regime II, the vertical mean and turbulent NO_x fluxes are the largest at x/H = 0.4875 (1030 LST) and x/H = 0.4625 (1010 LST), respectively. In flow regime I, a dipole pattern of vertical mean NO_x flux is apparent, and the vertical mean NO_x flux is

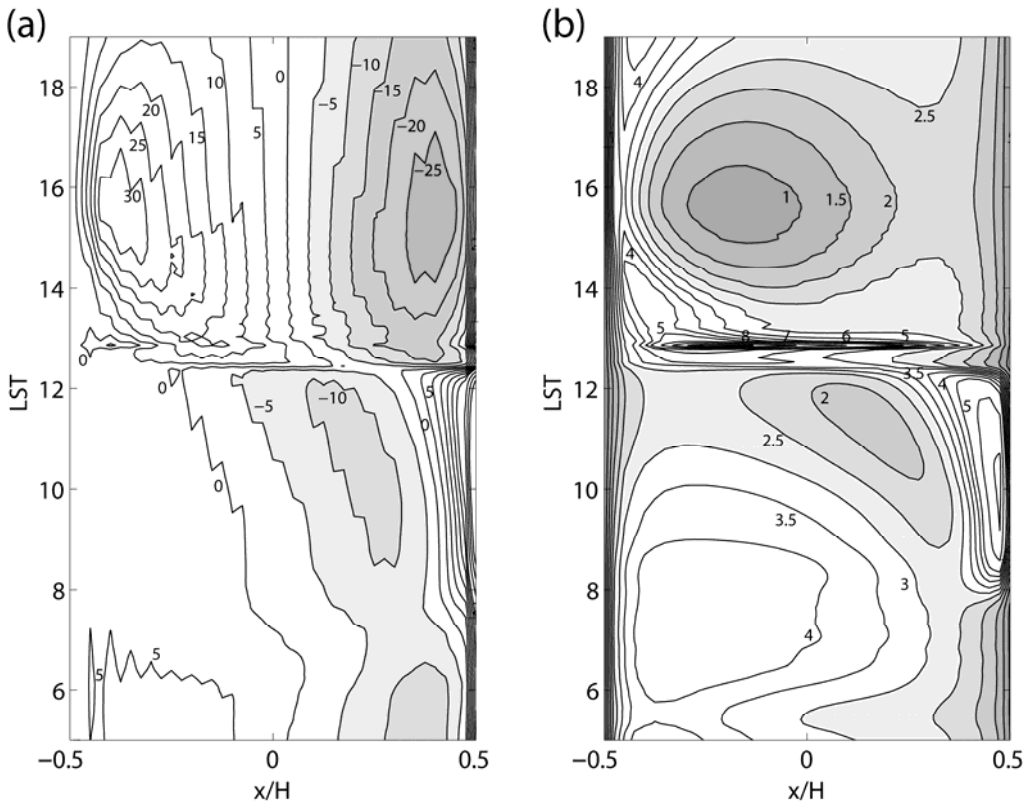

Figure 7.5. Diurnal variations of vertical (a) mean and (b) turbulent NO_x fluxes at the roof level. Positive (negative) values denote upward (downward) flux. The unit is ppb m s^{-1}. Shaded areas are for the vertical mean and turbulent NO_x fluxes smaller than 0 and 3 ppb m s^{-1}, respectively.

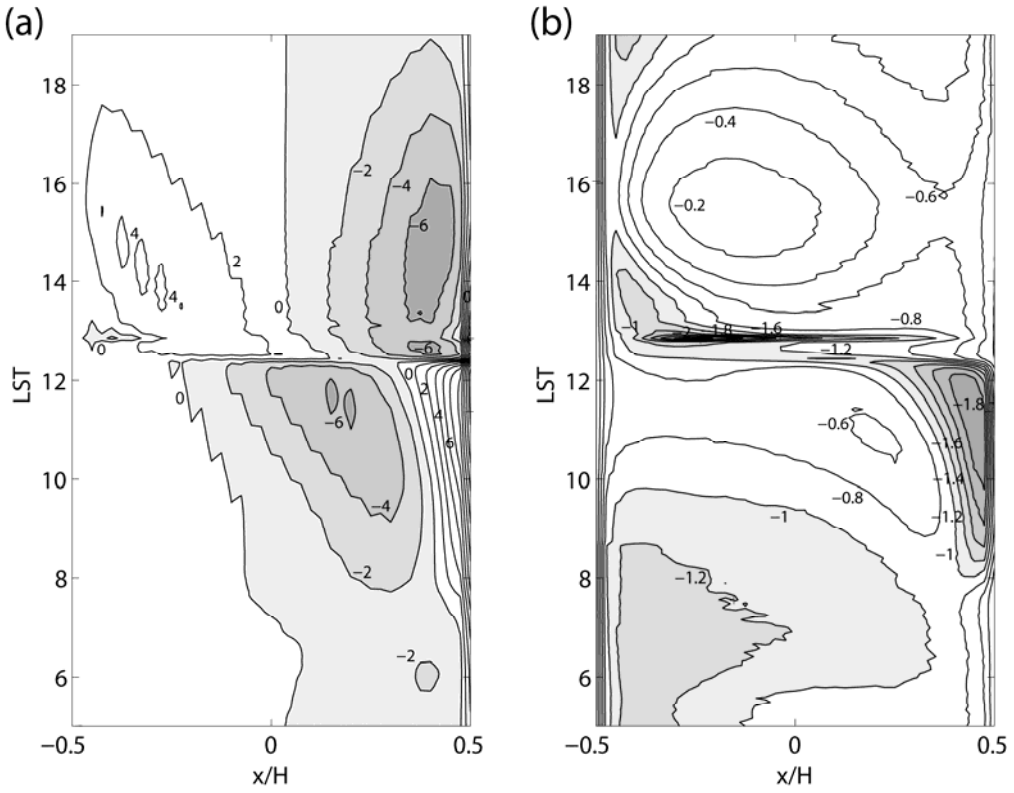

Figure 7.6. The same as Figure 7.5 but for O_3 fluxes. Shaded areas are for the vertical mean and turbulent O_3 fluxes smaller than 0 and –0.8 ppb m s^{-1}, respectively.

the largest at x/H = –0.3875 (1525 LST). As shown in Figure 7.4c and d (flow regime II) and Figure 7.4e and f (flow regime I), thermally driven upward flow and thermally intensified upward flow, respectively, are evident along the building wall with the higher temperature, which are important for the vertical NO_x transport in the street canyon. Therefore, it is natural that the vertical mean and turbulent NO_x fluxes are large in the region close to the building wall with the higher temperature. During the transition of flow regime from II to I at about 1240 LST, plenty of poorly ventilated NO_x is removed out of the street canyon because the transition leads to a rapid NO_x mixing in the street canyon. As a result, the vertical turbulent NO_x flux abruptly increases.

In an isothermal condition, the dipole pattern of vertical mean scalar flux at the roof level of the street canyon with a canyon aspect ratio of 1 has been reported (Cai et al., 2008; Li et al., 2009). The vertical turbulent scalar flux exhibits its active region close to the upwind building wall ($x/H \sim -0.2$ in terms of the label in this study) (Liu and Barth, 2002; Liu et al., 2004). When the surface is heated, active regions for scalar transport by both mean and turbulent flow are further shifted toward the upwind building wall (Cheng et al., 2009; Li et al., 2012). The previous studies mentioned above did not consider the effect of dry deposition and the diurnal variation of surface heating. Despite the differences, the features mentioned in the previous studies are qualitatively

captured in this study because NO_x, which is conserved during the conversion between NO and NO_2, can be regarded as a passive scalar in a short period of time.

The patterns of the horizontal and temporal distributions of vertical mean and turbulent O_3 fluxes at the roof level (Figure 7.6) are similar to those of vertical mean and turbulent NO_x fluxes (Figure 7.5). Note that the signs of vertical mean NO_x and O_3 fluxes are the same because these are identically determined by the sign of mean vertical velocity. Unlike the NO_x removal by mean flow, the O_3 entrainment by mean flow is active on the downwind building wall side (but not very close to the wall). In contrast, the signs of vertical turbulent NO_x and O_3 fluxes are opposite to each other because these are individually determined by the signs of vertical NO_x and O_3 concentration gradient, respectively. Accordingly, the NO_x removal and O_3 entrainment by turbulent flow are identically active in the region close to the building wall with the higher temperature.

Figure 7.7 shows the diurnal variations of horizontally averaged NO_x and O_3 fluxes at the roof level. It is found that the transport by turbulent flow is mostly responsible for both NO_x removal and O_3 entrainment except for the period of 1430–1530 LST. In flow regime II, the upward mean NO_x flux and downward mean O_3 flux are much smaller than the upward turbulent NO_x flux

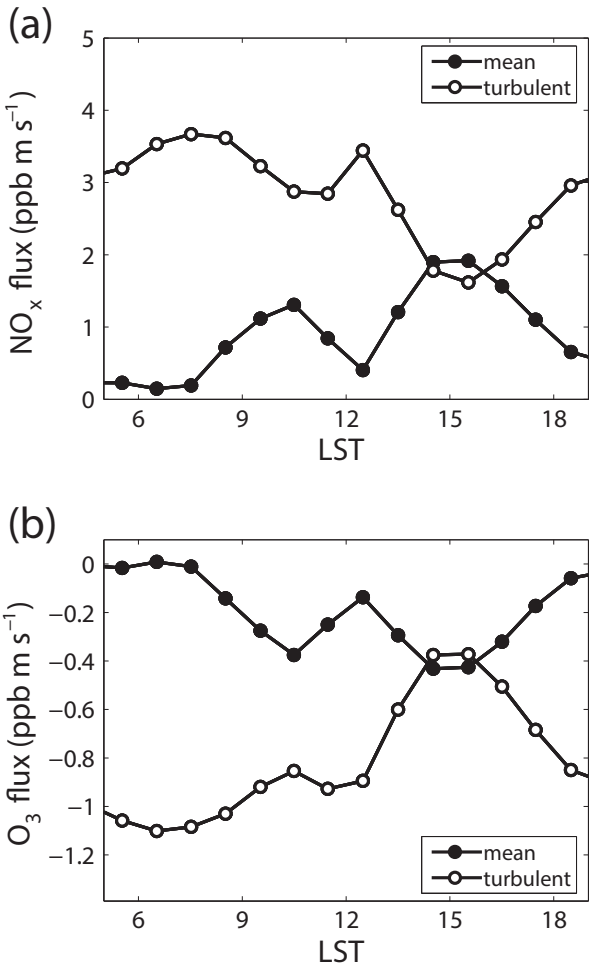

Figure 7.7. Diurnal variations of horizontally averaged vertical mean and turbulent (a) NO_x and (b) O_3 fluxes at the roof level. The vertical fluxes are hourly averaged.

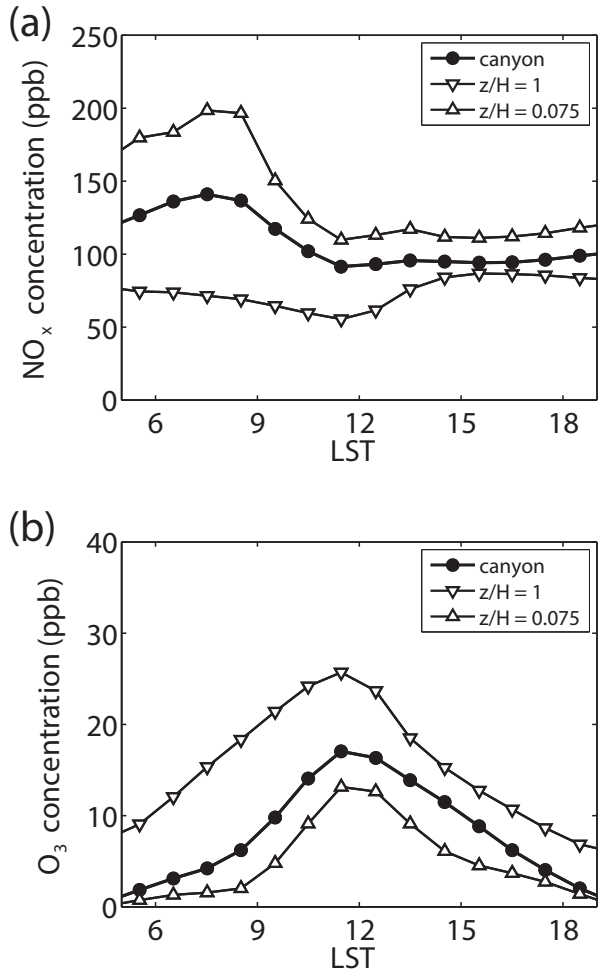

Figure 7.8. Diurnal variations of canyon-, pedestrian-level- (z/H = 0.075), and roof-level- (z/H = 1) averaged (a) NO_x and (b) O_3 concentrations. The concentrations are hourly averaged.

and downward turbulent O_3 flux, respectively. This can be attributed to the negligible vertical flow at the roof level in relation to the weakened upper vortex as shown in Figure 7.4b. After the transition of flow regime from II to I, the upward mean NO_x flux and downward mean O_3 flux evidently increase up to 1.92 ppb m s^{-1} at 1530 LST and 0.43 ppb m s^{-1} at 1430 LST, respectively. For the period of 1430–1530 LST, the contribution of mean flow to the NO_x removal and O_3 entrainment eventually exceeds that of turbulent flow. This can be attributed to the intensified primary vortex expanding over the roof level in flow regime I as shown in Figure 7.4f.

The diurnal variation of vertical pollutant flux should be interpreted in association with the diurnal variation of pollutant concentration as well as the diurnal variation of flow. Figure 7.8 shows the diurnal variations of canyon-, pedestrian-level- (z/H = 0.075), and roof-level-averaged NO_x and O_3 concentrations. The canyon-averaged NO_x concentration is higher in flow regime II than in flow regime I. This agrees with the results of previous studies showing that the scalar concentration in a street canyon is high when two counter-rotating vortices appear in the street canyon in the presence of the downwind building-wall heating (Sini et al., 1996; Kim and Baik, 1999; Xie et al., 2007). The O_3 concentrations are the highest around noon. The differences between the pedestrian-level- and roof-level-averaged concentrations are large in flow regime

II with maximum differences of 127 ppb at 0830 LST for NO_x and 17 ppb at 0930 LST for O_3. The large differences in flow regime II are resulted from the weakened vertical NO_x and O_3 transport in the street canyon by the two counter-rotating vortices. On the contrary, the vertical NO_x and O_3 transport in the street canyon is enhanced by the intensified primary vortex in flow regime I, resulting in the small differences between the pedestrian-level- and roof-level-averaged concentrations.

7.7 Exchange velocity

The efficiencies of NO_x removal and O_3 entrainment are quantified by estimating NO_x and O_3 exchange velocities, respectively, that are individually calculated using Eq. (7.5). Figure 7.9a shows the diurnal variations of NO_x and O_3 exchange velocities. The NO_x and O_3 exchange velocities increase in the morning and then decrease in the afternoon. The NO_x and O_3 exchange velocities are obviously similar to each other only in the early morning. In their mean (Figure 7.9b) and turbulent (Figure 7.9c) components, the mean NO_x exchange velocity is generally higher in flow regime I than in flow regime II, whereas the turbulent O_3 exchange velocity is lower in flow regime I than in flow regime II. As a result, the O_3 exchange velocity is significantly lower than the NO_x

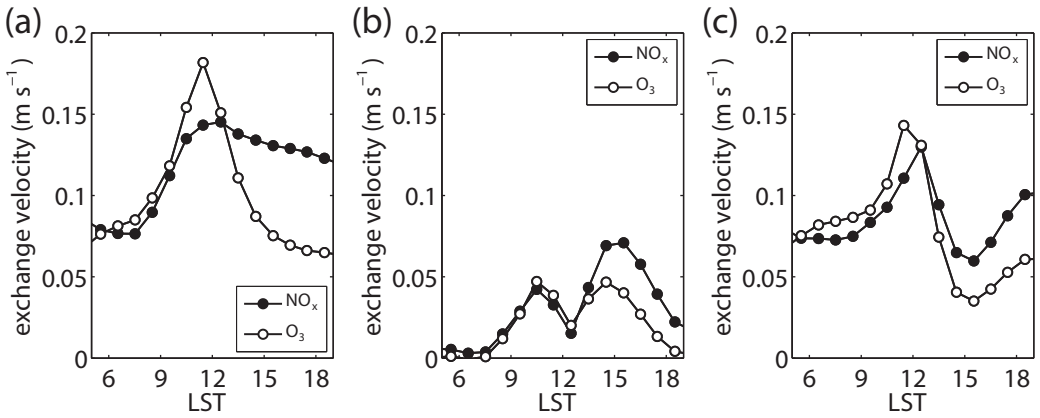

Figure 7.9. Diurnal variations of (a) NO_x and O_3 exchange velocities and their (b) mean and (c) turbulent components.

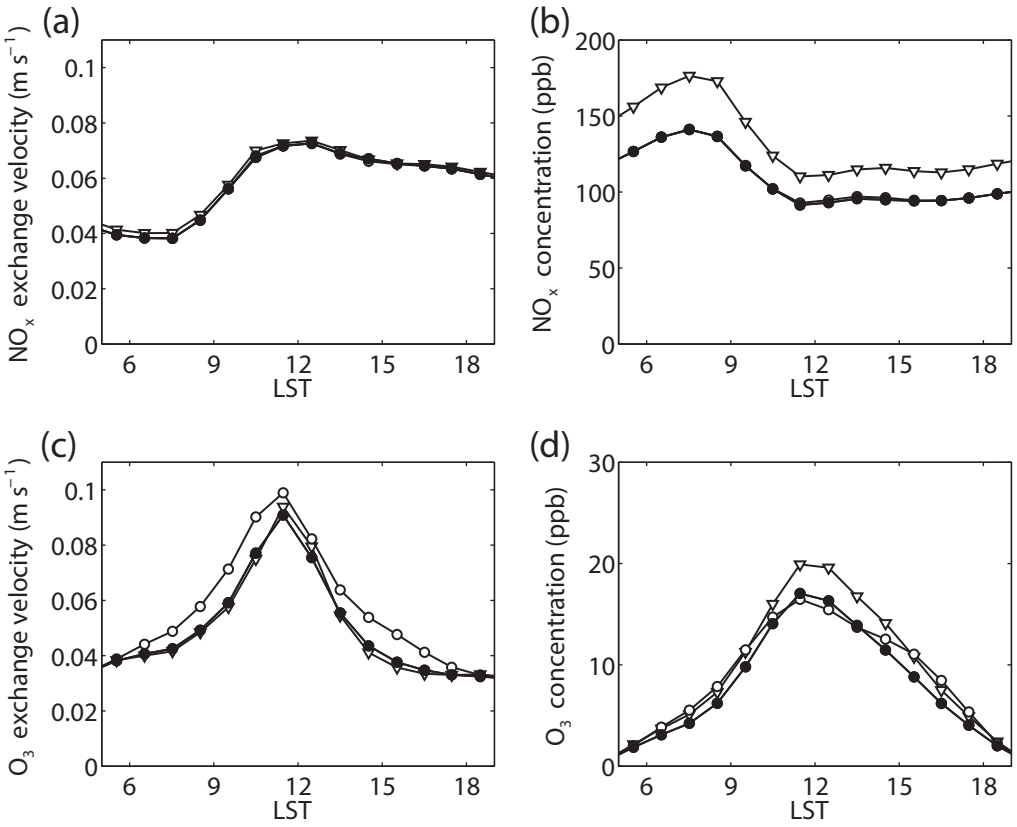

Figure 7.10. Diurnal variations of (a) NO_x and (c) O_3 exchange velocities and canyon-averaged (b) NO_x and (d) O_3 concentrations in the control (closed circle), sunlit-canyon (open circle), and no-deposition (open reversed triangle) simulations.

exchange velocity in flow regime I, which in turn emphasizes that the exchange velocities of reactive pollutants depend on flow regime.

Most previous studies adopting an exchange velocity have considered isothermal conditions in which the vertical mean pollutant flux is minor compared to the vertical turbulent pollutant flux at the roof level. Cai (2012) extended the use of exchange velocity in non-isothermal conditions in which the vertical mean pollutant flux is not minor any further. Based on previous studies, we extend the use of exchange velocity for reactive pollutants removed out or entrained into the street canyon and find that the difference between NO_x and O_3 exchange velocities is significantly large in flow regime I when the vertical mean pollutant fluxes at the roof level are not minor.

Another interesting point is that the diurnal variation of O_3 exchange velocity (0.032–0.091 m s^{-1}) is larger than that of NO_x exchange velocity (0.038–0.073 m s^{-1}). To examine the dependencies of exchange velocity on photochemistry and deposition processes in the street canyon, two additional simulations (hereafter, called the sunlit-canyon simulation and the no-deposition simulation) are performed in which the effect of shadow on photochemistry and the effect of dry deposition are neglected in the street canyon, respectively. Figure 7.10 shows the diurnal variations of NO_x and O_3 exchange velocities and canyon-averaged NO_x and O_3 concentrations in the control, sunlit-canyon, and

no-deposition simulations. The NO_x exchange velocities in the control and sunlit-canyon simulations are nearly overlapped. The NO_x exchange velocity in the no-deposition simulation is slightly higher than that in other simulations. In contrast, the O_3 exchange velocity in the sunlit-canyon simulation is higher than that in other simulations. For example, the O_3 exchange velocity at 1030 LST increases from 0.077 to 0.090 m s^{-1} when the effect of shadow on photochemistry is neglected. On the other hand, the O_3 exchange velocities in the control and no-deposition simulations show negligible differences between them, although the effects of dry deposition on the NO_x and O_3 concentrations are significant (Figure 7.10b and d). This comparison indicates that photochemistry in a street canyon is influential for estimating the exchange velocity of a reactive pollutant, whereas dry deposition in a street canyon is not influential as much as photochemistry.

8 Urban Air Quality Simulation in a High-rise Building Area using a CFD Model Coupled with Mesoscale Meteorological and Chemistry-Transport Models

8.1 One-way coupling

As microscale turbulent mixing and photochemical processes are major parts of our concerns, an investigation of these processes in a real morphology is the next step of this study. Photochemistry and dispersion of pollutants in a real morphology are complex and different from those in an idealized street canyon. A number of important factors such as building geometry, emission, wind speed and direction, shadow, and surface heat exchange are heterogeneous in a small area. For preparing microscale simulations of flow and dispersion, initial and boundary conditions for wind, temperature, and pollutant concentrations are

needed. Baik et al. (2009), for example, simulated microscale flow and scalar dispersion in a densely built-up area of Seoul with initial and boundary conditions obtained from the linear interpolation of mesoscale meteorological model results. It was reasonable for reproducing wind speed and direction and turbulent kinetic energy at inflow boundaries of the CFD model domain. However, initial and boundary conditions for pollutant concentrations are still questionable to be applied in a microscale simulation. In this step, a one-way coupling of mesoscale meteorological and chemistry-transport models to a CFD model is attempted to address these scientific and technical issues.

A CFD model that is a Reynolds-averaged Navier–Stokes equations (RANS) model (Kim and Baik, 2004; Baik et al., 2007) is coupled with the Weather Research and Forecasting (WRF) model version 3.2 (Skamarock et al., 2008) and the Community Multiscale Air Quality (CMAQ) model version 4.7.1 (Byun and Schere, 2006). For the consistency of chemical processes between the CFD model and CMAQ model, the Statewide Air Pollution Research Center version 99 (SAPRC-99) chemical mechanism (Carter, 2000) and the Eulerian Backward Iteration (EBI) method (Hertel et al., 1993) used in the CMAQ model are implemented into the CFD model in this study.

One-way coupling is employed. The horizontal wind components, air temperature, and turbulent kinetic energy profiles and 2-m air temperature

obtained from the WRF simulation and the pollutant concentration profiles, mobile emission rates, and photolysis rates obtained from the CMAQ simulation are used as the initial and boundary conditions in the CFD simulation. The horizontal wind components, air temperature, turbulent kinetic energy, 2-m air temperature, and pollutant concentration data are prepared at every 30 minutes, and the mobile emission rate and photolysis rate data are prepared at every 60 minutes. The horizontal wind components, air temperature, turbulent kinetic energy, and pollutant concentration data obtained from the several vertical levels of the mesoscale model domains are linearly interpolated at every vertical level of the CFD model domain. The 2-m air temperature data in the WRF simulation is used for specifying the air temperature at the grid points closest to horizontal surfaces in the CFD simulation, while the adiabatic boundary condition is adopted at the grid points closest to vertical surfaces (e.g., building walls). The mobile emission rates are spatially allocated on roads in the CFD model domain. The photolysis rates are uniformly adopted in the CFD model domain. To update the input data in the CFD simulation at every dynamics time step, the linear interpolation method is also applied in time for the output data of the mesoscale simulations.

8.2 Experimental setup

The WRF and CMAQ simulations are performed for the period from 2100 LT (= UTC + 9 h) 1 June 2010 to 0900 LT 4 June 2010. In the WRF simulation, four nested domains with horizontal grid sizes of 27, 9, 3, and 1 km are adopted. Seoul (37°N, 127°E), a megacity in Republic of Korea, is located in the middle of the innermost domain (Figure 8.1a). Mellor-Yamada-Janjić (MYJ) Planetary Boundary Layer (PBL) scheme (Mellor and Yamada, 1982; Janjić, 1994) that prognostically calculates turbulent kinetic energy and the Seoul National University Urban Canopy Model (SNUUCM; Ryu et al., 2011) are used. This study takes account of the gridded anthropogenic heat data established by Lee et al. (2009) with a spatial resolution of 0.01° and a temporal resolution of hour.

In the CMAQ simulation, three nested domains with horizontal grid sizes of 9, 3, and 1 km are adopted. The SAPRC-99 chemical mechanism and the fifth-generation modal (AERO5) aerosol module (Foley et al., 2010) are used. Anthropogenic emission data are prepared using the Sparse Matrix Operator Kernel Emissions (SMOKE) system (Houyoux et al., 2000). The 2007 Clean Air Policy Support System (CAPSS) (Moon et al., 2006) data updated by Ryu et al. (2013) for year of 2008 are used as the anthropogenic emission inventory in Republic of Korea. Biogenic emission data are prepared using the Model of Emissions of Gases and Aerosols from Nature (MEGAN) (Guenther et al., 2006).

The default concentration profiles of CMAQ model are applied at the boundaries of outermost domain.

A CFD simulation is performed for the period from 0900 to 1800 LT 3 June 2010 in a high-rise building area of Seoul. The CFD model domain size is 1600 m in the *x*- and *y*-directions and 997 m in the *z*-direction (corresponding to 11 vertical model levels in the mesoscale simulations). The number of grids is 160 × 160 × 106, and the grid size up to z = 200 m is 10 m × 10 m × 4 m. In the CFD model domain, the surface heights that includes topographical and building heights were estimated by a light detection and ranging (LIDAR) measurement on an aircraft in 2008 (Figure 8.1b). The surface height is the lowest at z = 8 m and the highest at z = 124 m.

For the first 10-minute model run, the transport equations of chemical species are not integrated. At 0910 LT, the transport, dry deposition, and emission terms in the transport equations are activated. The chemical production term calculated by the SAPRC-99 chemical mechanism is activated at 0920 LT. The dynamics and chemistry time steps are 1 s and 60 s, respectively. The dry deposition term is calculated at all surfaces with constant deposition velocities that are, for example, 0.063 cm s^{-1} for NO_2, 0.12 cm s^{-1} for O_3, and 8 cm s^{-1} for HNO_3. Mobile emission is spatially allocated on roads in the CFD model domain

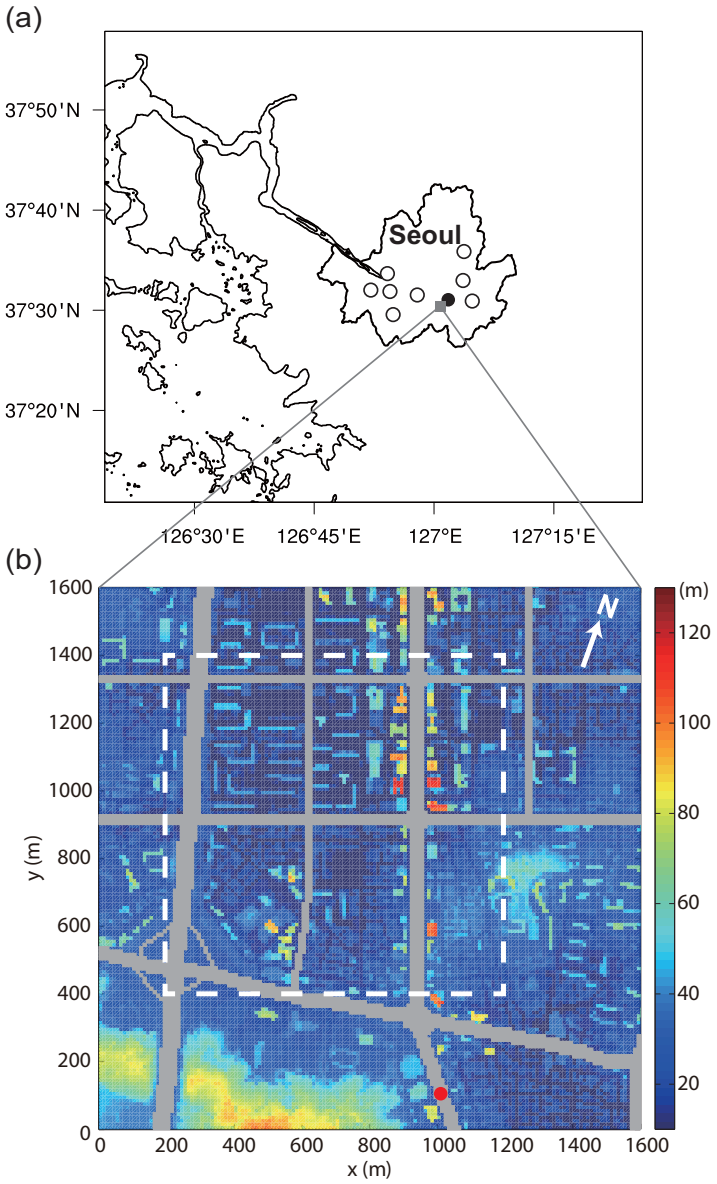

Figure 8.1. (a) The innermost mesoscale model domain and (b) the heights in the CFD model domain. In (a), open circles indicate the locations of automatic weather station (AWS) in Seoul, and a filled circle indicates the Gangnam AWS. In (b), a boxed area with a white dashed line is considered for analysis of CFD simulation results, and a red filled circle indicates the location of roadside air quality monitoring station.

(Figure 8.1b). Although the NO_2-to-NO_x ratio of mobile emission in the SAPRC-99 chemical mechanism is originally fixed as 0.05, the NO_2-to-NO_x ratio fixed as 0.05, the NO_2-to-NO_x ratio is changed to 0.2 in the CFD simulation based on the recent report in Seoul (Shon et al., 2011). The diurnal variation of mobile emission rate is also adjusted based on actual traffic counts near the study area.

8.3 Evaluation

Figure 8.2a shows the diurnal variations of simulated and observed near-surface air temperatures averaged over 9 Automatic Weather Stations (AWS) indicated by circles in Figure 8.1a in urban areas of Seoul on 3 June 2010. The cloud cover was 0/10−1/10 at Seoul meteorological observatory on that day under the influence of high-pressure system. The daily maxima of simulated and observed average air temperatures are 25.7°C and 26.8°C, respectively, at 1500 LT. The underestimation of air temperature is to some extent due to the daytime development of low-level clouds in the simulation. Despite the slight underestimation, the diurnal pattern is quite well reproduced in the WRF simulation.

Figure 8.2b and c shows the diurnal variations of the simulated and observed near-surface wind speeds and directions at Gangnam AWS indicated by the filled circle in Figure 8.1a on 3 June 2010. The WRF model reproduces

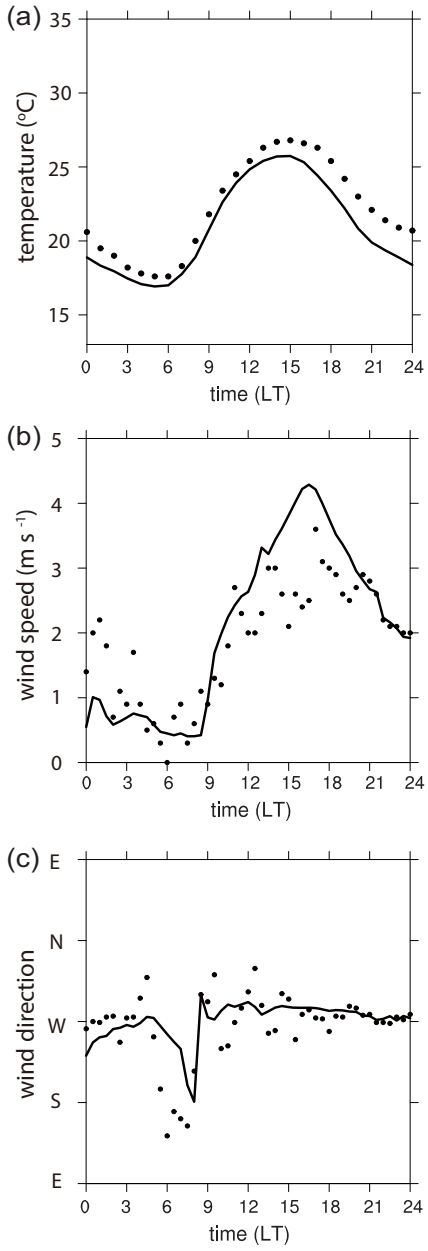

Figure 8.2. (a) Diurnal variations of the simulated (line) and observed (dot) near-surface air temperatures averaged over 9 AWS in urban areas of Seoul on 3 June 2010. The diurnal variations of the simulated (line) and observed (dot) near-surface (b) wind speeds and (c) directions at Gangnam AWS (AWS closest to the selected area for the CFD simulation) on 3 June 2010.

the low wind speeds in the early morning and the increasing trend of wind speed until the late afternoon. The WRF model also well reproduces the northwesterly to westerly wind during the daytime especially for the period of CFD simulation, which guarantees the accurate inputs of horizontal wind components at the inflow and outflow boundaries of the CFD model domain.

Figure 8.3 shows the diurnal variations of the simulated and observed near-surface NO_2 and O_3 concentrations averaged over 71 air quality monitoring stations in urban areas in the innermost domain on 3 June 2010. While the NO_2 concentration widely ranges from a few ppb to tens ppb at a certain time, the daily maxima of simulated and observed average NO_2 concentrations are 53 ppb and 48 ppb, respectively, at 0800 LT. The average NO_2 concentration is consistently underestimated from 1000 LT. On the other hand, the daily maxima of simulated and observed average O_3 concentrations are 50 ppb and 63 ppb, respectively, at 1300 LT. The maximum of O_3 concentration at an air quality monitoring station is 92 ppb at 1500 LT, which is not reproduced in the CMAQ simulation. Overall, the average O_3 concentration is consistently underestimated for the period of CFD simulation.

The underestimations of average NO_2 and O_3 concentrations for the period of CFD simulation can be resulted from the improper boundary conditions for pollutant concentrations in the CMAQ simulation. The prevailing

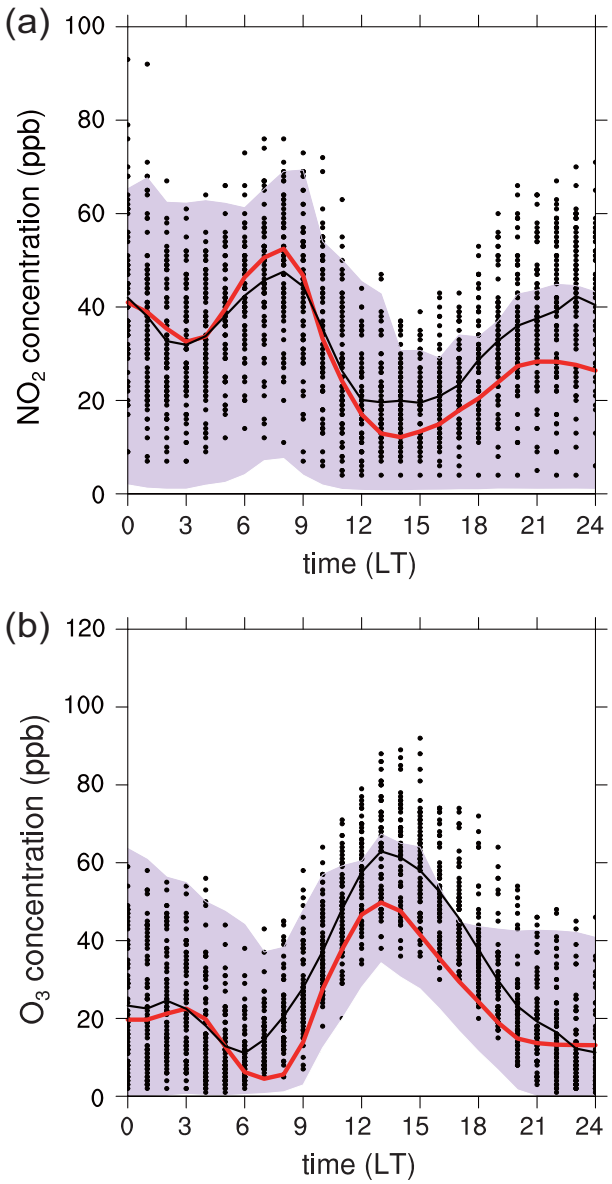

Figure 8.3. Diurnal variations of the simulated (red, purple) and observed (black) near-surface (a) NO_2 and (b) O_3 concentrations averaged over 71 air quality monitoring stations in urban areas in the innermost domain on 3 June 2010. Lines indicate the averaged concentrations.

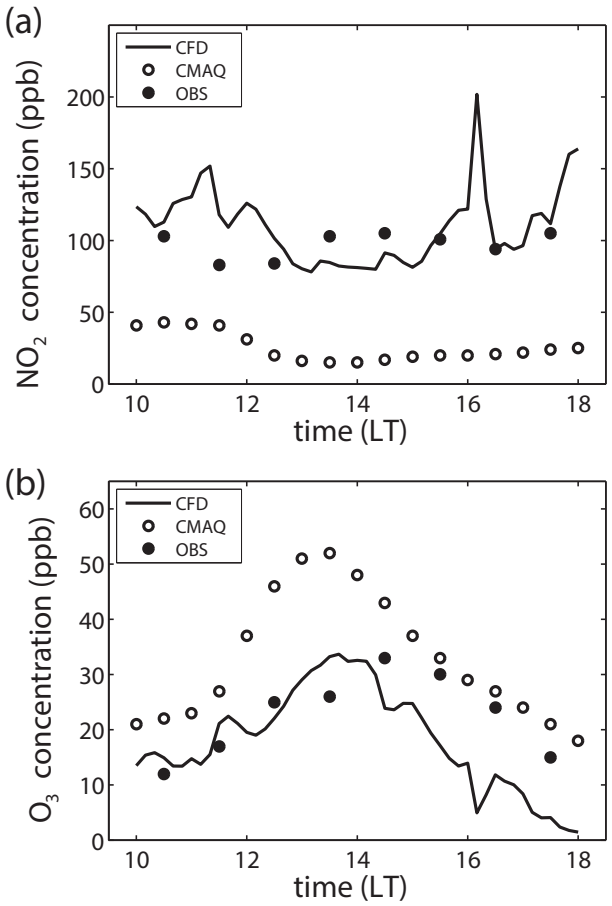

Figure 8.4. Temporal variations of the simulated (line, open circle) and observed (filled circle) near-surface (a) NO_2 and (b) O_3 concentrations at a roadside air quality monitoring station indicated by a red circle in Figure 8.1b on 3 June 2010.

westerly wind on that day could enhance the long-range transport of pollutants such as NO_2 and O_3 emitted or chemically produced in the west (the Yellow Sea or China). Another possibility is an insufficient urban surface representation in the CMAQ simulation. Because the evaluation is conducted for the near-surface NO_2 and O_3 concentrations in urban areas, urban surface characteristics such as building geometry and mobile emission are certainly reflected in the NO_2 and O_3 concentrations observed at air quality monitoring stations. This is an incompleteness of chemistry-transport model which can be improved by using the coupled CFD model.

The NO_2 and O_3 concentrations in the CFD simulation are evaluated at a roadside air quality monitoring station and compared with those in the CMAQ simulation (Figure 8.4). The roadside air quality monitoring station with an inlet height of 4 m above the surface is located at the red circle in Figure 8.1b. As expected from the proximity to mobile emission source, the NO_2 concentration in the CFD simulation is much higher than that in the CMAQ simulation, whereas the O_3 concentration in the CFD simulation is much lower than that in the CMAQ simulation. The observed NO_2 concentration is obviously better reproduced in the CFD simulation than in the CMAQ simulation. The observed O_3 concentration is close to the simulated one in the CFD simulation until 1400 LT but close to the simulated one in the CMAQ

simulation in the late afternoon. The daily maxima of O_3 concentration are 34 ppb in the CFD simulation and 33 ppb in the observation. The large deviation of O_3 concentration in the CFD simulation in the late afternoon is basically resulted from the underestimated O_3 concentration in the CMAQ simulation as discussed with Figure 8.3b. Using the integrated urban air quality modeling system, the evaluation shows a significant improvement particularly for simulating near-road air quality in a high-rise building area.

8.4 Control simulation

The 1 km × 1 km area indicated by a white dashed line in Figure 8.1b is considered for the analysis of CFD simulation. This area includes a highway (x ~ 200 m) and a main road (x = 950 m) almost in parallel to each other and several high-rise buildings along the main road. The orientation of the main road in this area is 21° from the due North. The CFD simulation results are analyzed for 8 h from 1000 to 1800 LT excluding the first 1-h spin-up time.

Figure 8.5 shows the NO_2 and O_3 concentration fields at z = 30 m at 1200, 1400, and 1600 LT. Note that the height of z = 30 m in the CFD simulation approximately corresponds to the height of the lowest CMAQ model level. The high NO_2 concentration (> 100 ppb) and low O_3 concentration (< 10 ppb) are

apparent above roads regardless of time, which is attributed to the freshly emitted NO_x from vehicles. The polluted air is shown to be hardly dispersed outside the roads due to buildings. At 1400 LT, for example, an apartment area (x ~ 600 m, y ~ 1000 m) exhibits relatively low NO_2 and high O_3 concentrations that are much close to their ambient concentrations. The opposite relationship between the NO_2 and O_3 concentrations is a result from the NO titration of O_3 that is the most dominant chemical process near mobile sources. Therefore, Figure 8.5 reveals that the large NO_2 and O_3 spatial variabilities at this height are strongly associated with mobile emission on road.

Figure 8.6 shows the NO_2 and O_3 concentration fields at z = 74 m at 1200, 1400, and 1600 LT. Note that the height of z = 74 m in the CFD simulation approximately corresponds to the height of the second lowest CMAQ model level. The locations of several high-rise buildings along the main road are depicted in the concentration fields. The high NO_2 concentration and low O_3 concentration are apparent around the high-rise buildings. As the ambient wind speed increases with time until 1600 LT (Figure 8.2b), plume-like NO_2 dispersion patterns are elongated to the downwind of the buildings especially at 1400 and 1600 LT. Around the high-rise buildings, the low O_3 concentration is still distinct at this height. At 1400 LT, for example, the O_3 concentration around

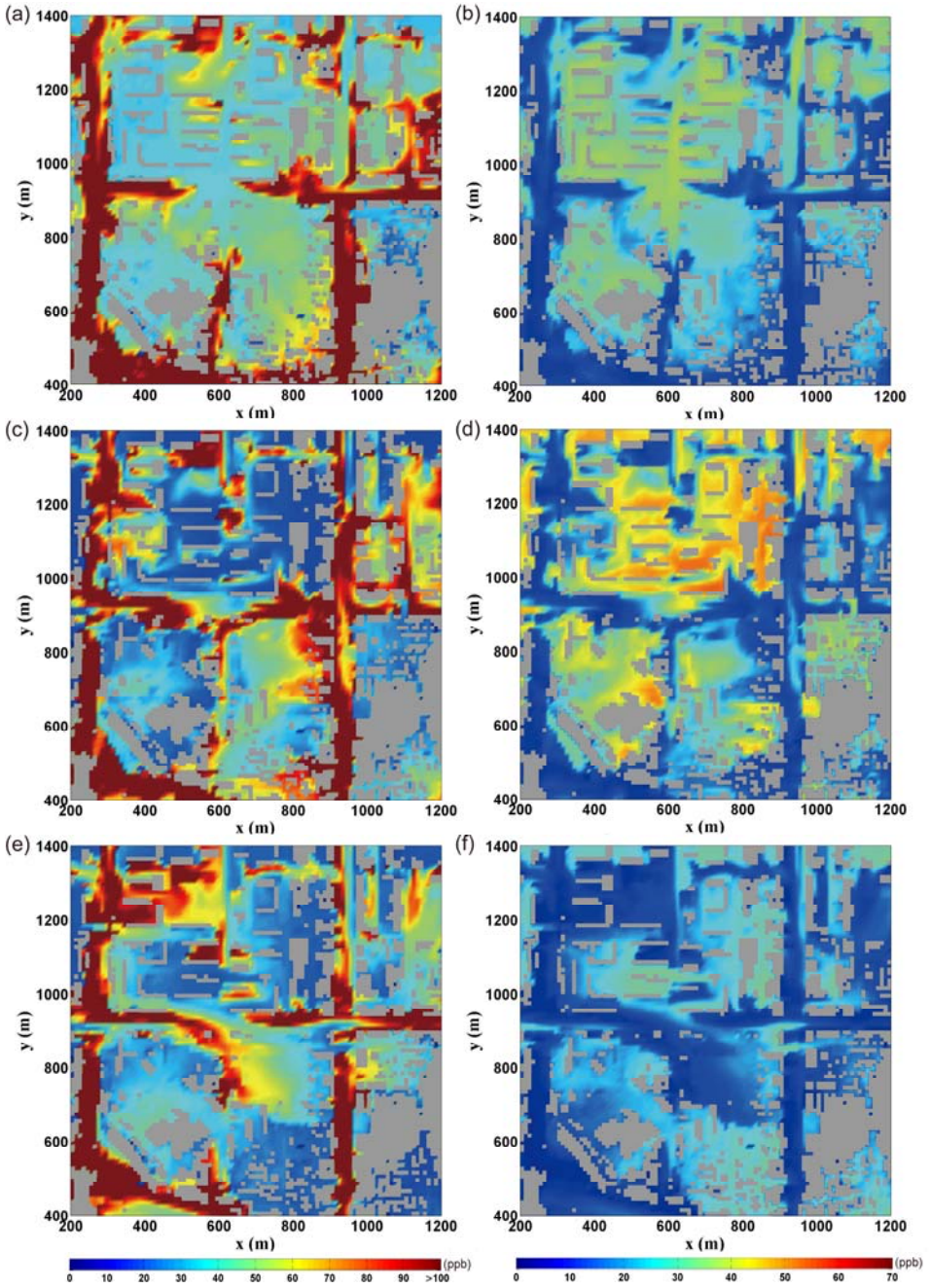

Figure 8.5. (left panels) NO_2 and (right panels) O_3 concentration fields at z = 30 m at (a, b) 1200, (c, d) 1400, and (e, f) 1600 LT.

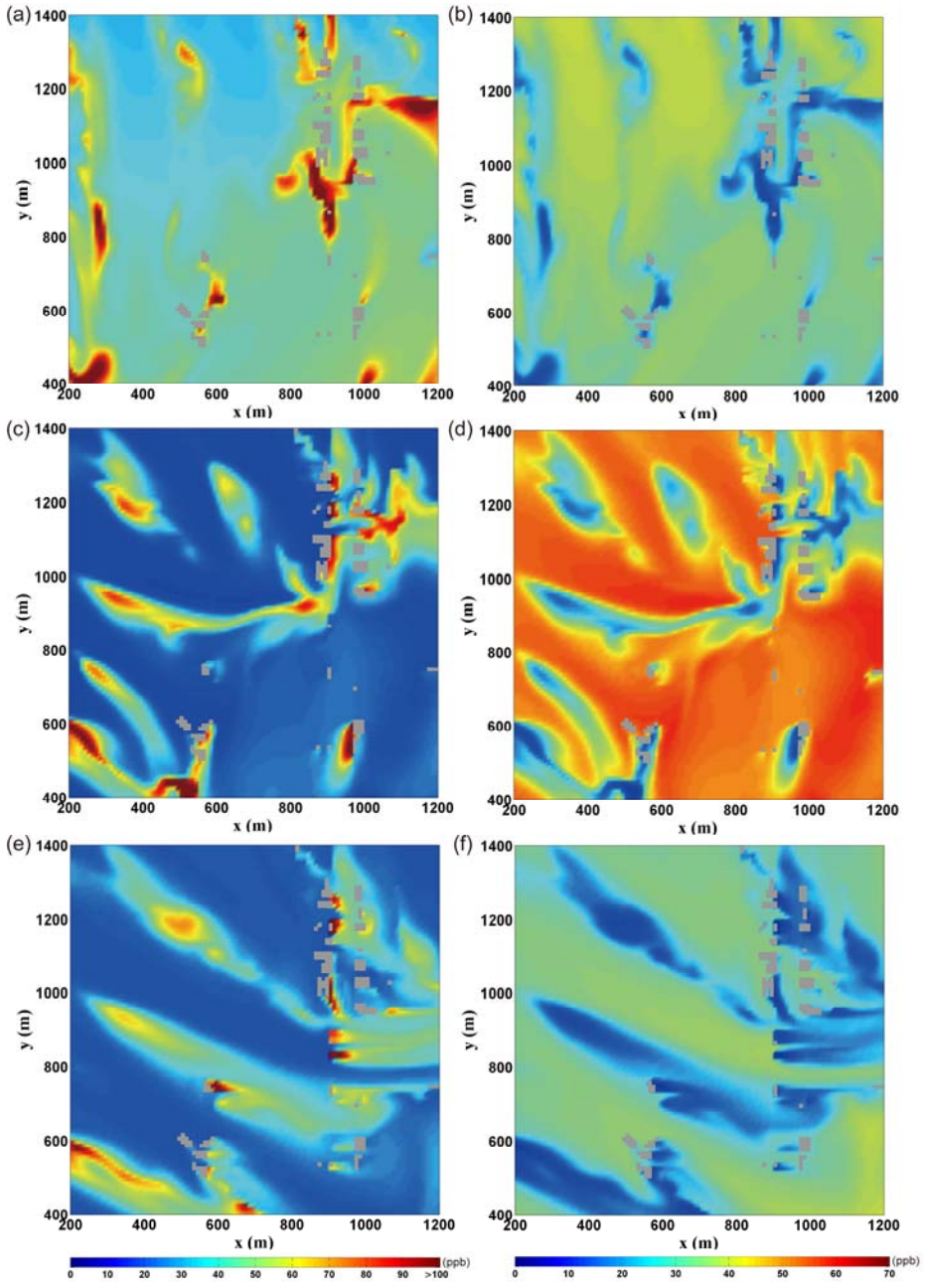

Figure 8.6. (left panels) NO_2 and (right panels) O_3 concentration fields at z = 74 m at (a, b) 1200, (c, d) 1400, and (e, f) 1600 LT.

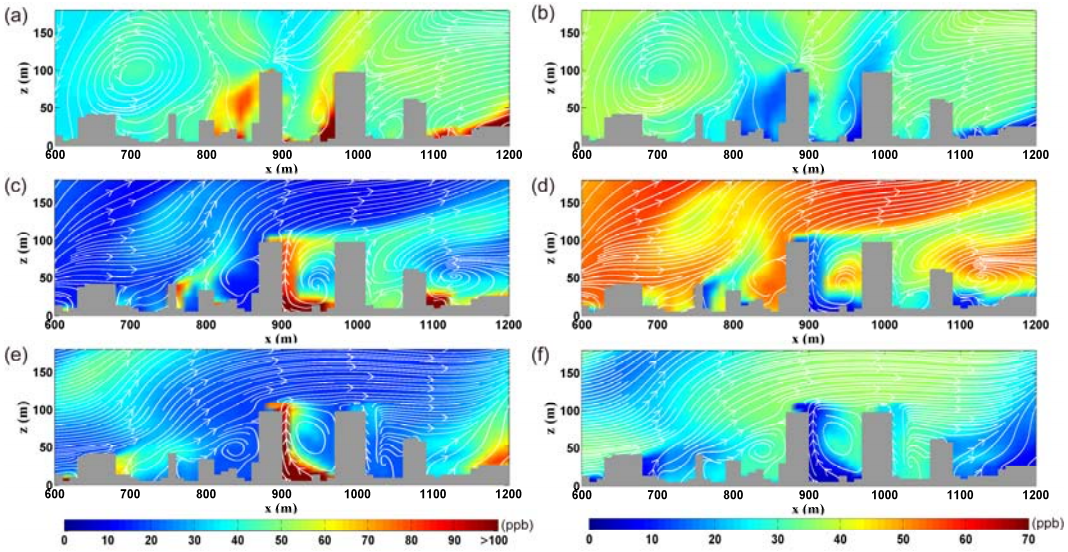

Figure 8.7. (left panels) NO_2 and (right panels) O_3 concentrations and streamline fields at y = 1025 m at (a, b) 1200, (c, d) 1400, and (e, f) 1600 LT.

and downwind of the high-rise buildings is found to be lower than 20 ppb, while the ambient O_3 concentration is higher than 50 ppb. Therefore, Figure 8.6 reveals that the large NO_2 and O_3 spatial variabilities at this height are strongly associated with high-rise buildings.

Figure 8.7 shows the NO_2 and O_3 concentrations and streamline fields at y = 1025 m at 1200, 1400, and 1600 LT. The width of the main road is 40 m from x = 930 to 970 m. At 1200 LT when the ambient wind is relatively weak, there is little vortex-type flow near the surface. As the ambient wind speed increases with time, the upward NO_2 transport to the rooftop level following an apparent clockwise vortex is significant along the upwind building wall, coincident with the low O_3 concentration. This is a well-known phenomenon examined within a street canyon (Baik et al., 2007). The plume-like NO_2 dispersion around high-rise buildings shown in Figure 8.6 is originated from the upward NO_2 transport along building walls starting from the mobile emission on roads.

The large NO_2 and O_3 spatial variabilities shown in their concentration fields are found to be associated with heterogeneities of building geometry and mobile emission. The local phenomena are not able to be captured by the CMAQ simulation at the corresponding model levels because of its low model resolution and insufficient representation of urban surface characteristics. In the next, the

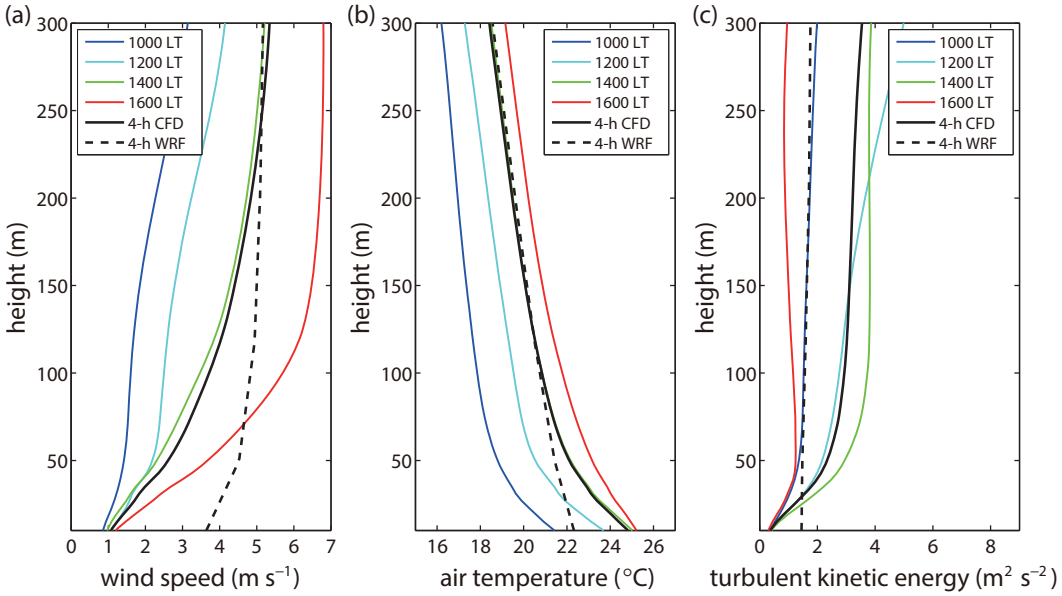

Figure 8.8. Vertical profiles of area-averaged (a) wind speed, (b) air temperature, and (c) turbulent kinetic energy at 1000, 1200, 1400, and 1600 LT in the CFD simulation. Vertical profiles of area averages in the CFD simulation (black solid line) and vertical profiles in the WRF simulation (black dashed line) are averaged for 4 h from 1200 to 1600 LT.

area averages of NO_2 and O_3 concentrations over the 1 km × 1 km area in the CFD simulation are systematically compared with the NO_2 and O_3 concentrations in the CMAQ simulation to examine the roles of spatial variability in the representative air quality in this area.

Figure 8.8 shows the vertical profiles of area-averaged wind speed, air temperature, and turbulent kinetic energy at 1000, 1200, 1400, and 1600 LT in the CFD simulation. In addition, the vertical profiles of area averages in the CFD simulation and the vertical profiles in the WRF simulation are identically averaged for 4 h from 1200 to 1600 LT to compare the representativeness in this area. The wind speed increases with height and is higher at 1600 LT than at other selected times as discussed with Figure 8.2b. The 4-h averaged wind speed in the CFD simulation (1.7 m s^{-1} at z = 30 m) is largely reduced below the heights of high-rise buildings, compared to that in the WRF simulation (4.0 m s^{-1} at z = 30 m). The air temperature decreases with height and increases with time. The 4-h averaged air temperature near surfaces is higher in the CFD simulation (23.4°C at z = 30 m) than in the WRF simulation (21.9°C at z = 30 m). The turbulent kinetic energy increases with height and is the highest at 1400 LT below the heights of high-rise buildings. The 4-h averaged turbulent kinetic energy in the CFD simulation (1.3 m^2 s^{-2} at z = 30 m) is reduced by surfaces and buildings, whereas that in the WRF simulation (1.5 m^2 s^{-2} at z = 30 m) does not vary much

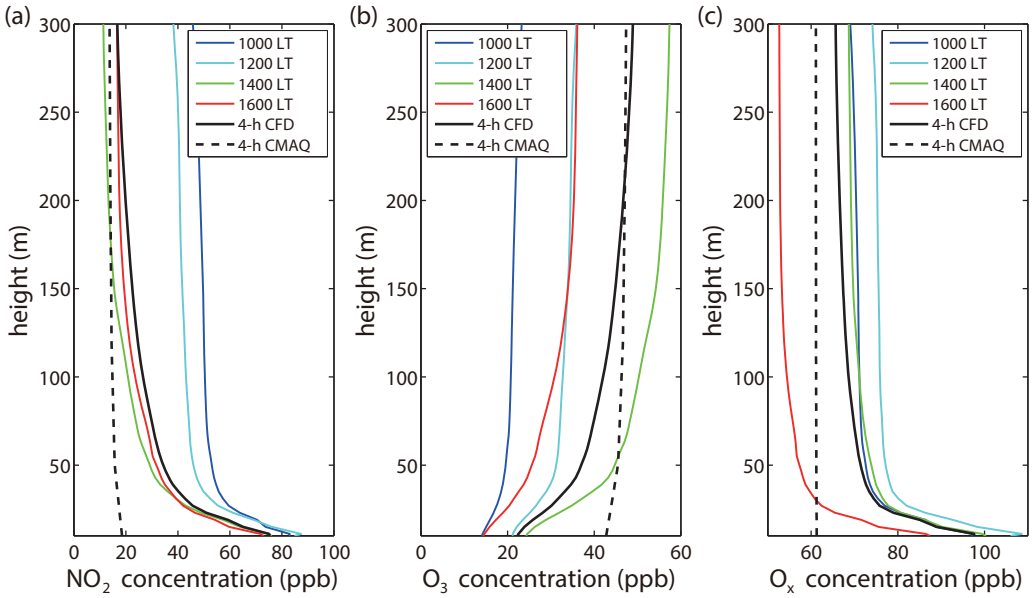

Figure 8.9. Vertical profiles of area-averaged (a) NO_2, (b) O_3, and (c) O_x concentrations at 1000, 1200, 1400, and 1600 LT in the CFD simulation. Vertical profiles of area averages in the CFD simulation (black solid line) and vertical profiles in the CMAQ simulation (black dashed line) are averaged for 4 h from 1200 to 1600 LT.

with height. In the evaluation of WRF simulation (Figure 8.2), the wind speed and the air temperature are overestimated and underestimated, respectively, in the period of CFD simulation. The comparison between the results in the CFD and WRF simulations indicates that the deviations in the WRF simulation can be resulted from the incomplete consideration of urban surface characteristics.

Figure 8.9 shows the vertical profiles of area-averaged NO_2, O_3, and O_x concentrations at 1000, 1200, 1400, and 1600 LT in the CFD simulation. In addition, the vertical profiles of area averages in the CFD simulation and the vertical profiles in the CMAQ simulation are identically averaged for 4 h from 1200 to 1600 LT to compare the representativeness in this area. The NO_2 concentration decreases with height. Comparing the vertical profiles of area averages at between 1400 and 1600 LT, the NO_2 concentration is lower at 1400 LT above z = 32 m, whereas it is lower at 1600 LT below z = 32 m. As the NO_2 concentration in the CMAQ simulation is lower at 1400 LT (Figure 8.3a), the lower NO_2 concentration below z = 32 m is possibly attributed to such local influences (e.g., trapping in building canopy, mobile emission, etc.). The O_3 concentration increases with height and is the highest at 1400 LT. At every selected time, the vertical gradient of O_3 concentration is larger below $z \sim 40$ m than above $z \sim 40$ m, which much differs the 4-h averaged O_3 concentration in the CFD simulation (30 ppb at z = 30 m) from that in the CMAQ simulation (44

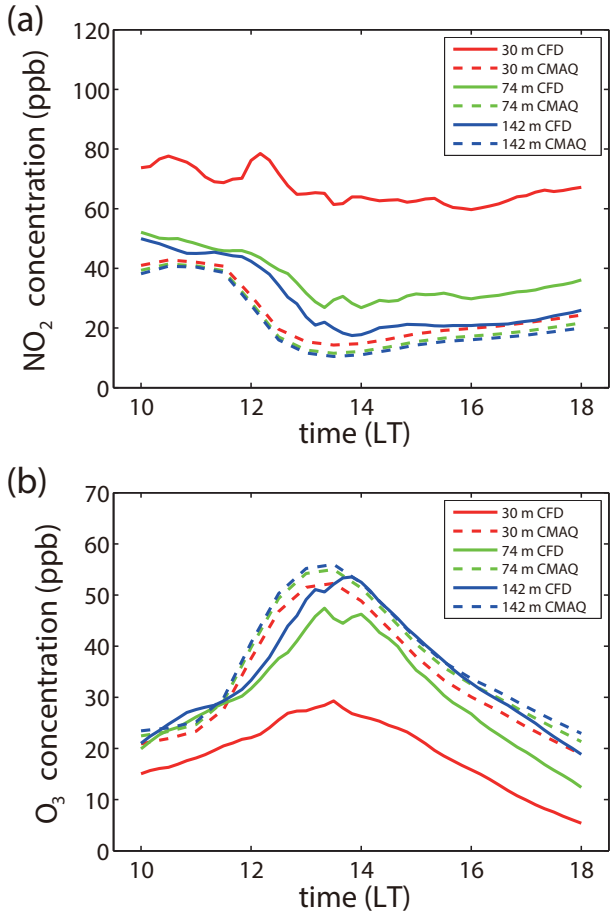

Figure 8.10. Temporal variations of area-averaged (a) NO_2 and (b) O_3 concentrations in the CFD simulation (solid line) and CMAQ simulation (dashed line) at z = 30, 74, and 162 m.

ppb at z = 30 m) below z ~ 40 m. In the CFD simulation, NO titrates O_3 mostly in limited spaces near roads because of the trapping effect in building canopy (Figure 8.5). In addition, this inefficient O_3 titration enables a large amount of NO to be transported to the roof level of high-rise buildings as shown in Figure 8.7. As a result, the vertical range of local influence is extended higher in the CFD simulation than that without building effects in the CMAQ simulation. O_x is simply defined as the sum of NO_2 and O_3, therefore, conserved during the rapid NO_2-to-O_3 conversion. It is interesting that the 4-h averaged O_x concentration in the CMAQ simulation (~ 61 ppb) shows an almost uniform distribution in the vertical. Hence, the increase in 4-h averaged O_x concentration below z ~ 40 m in the CFD simulation reflects the local influences of urban surface characteristics on the NO_2 and/or O_3 concentrations.

Figure 8.10 shows the temporal variations of area-averaged NO_2 and O_3 concentrations at z = 30, 74, and 162 m (the three lowest model levels in the CMAQ simulation). The temporal variations of NO_2 and O_3 concentrations in the CFD simulation generally follow those in the CMAQ simulation. At z = 30 m, however, the temporal variability is larger in the CMAQ simulation than in the CFD simulation because of the mobile emission influence that is less variable in time. The differences in NO_2 and O_3 concentrations at different model levels are

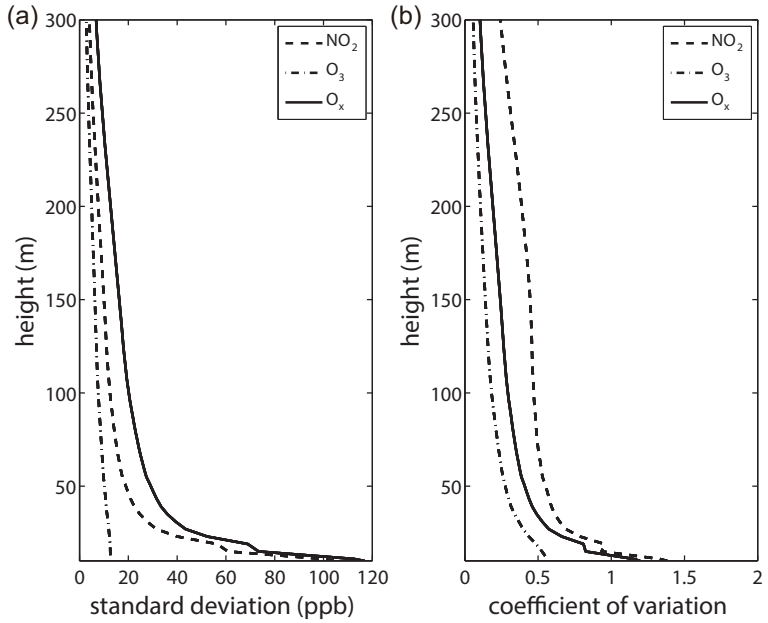

Figure 8.11. Vertical profiles of (a) standard deviation and (b) coefficient of variation (CV) of 4-h averaged NO_2, O_3, and O_x concentrations from 1200 to 1600 LT over the 1 km × 1 km area.

much larger in the CFD simulation than in the CMAQ simulation, implying the large spatial variability influenced by urban surface characteristics.

The spatial variability of pollutant concentrations can be quantitatively represented by calculating the standard deviation and further by introducing the coefficient of variation (CV). The CV defined as the normalized standard deviation (σ) by the mean concentration (μ) is calculated by

$$\mathrm{CV} = \frac{\sigma}{\mu}. \tag{8.1}$$

Figure 8.11 shows the vertical profiles of standard deviation and CV of 4-h averaged NO_2, O_3, and O_x concentrations from 1200 to 1600 LT over the 1 km × 1 km area. The standard deviation and CV of NO_2, O_3, and O_x concentrations decrease with height. The standard deviation is the largest for the O_x concentration (43.4 ppb at z = 30 m), whereas the CV is the largest for the NO_2 concentration (0.69 at z = 30 m). The O_3 concentration has the smallest standard deviation (12.0 ppb at z = 30 m) and CV (0.40 at z = 30 m) among them. This implies that the local influences have greater impacts on the spatial variability of NO_2 concentration rather than on that of the O_3 concentration. The CFD simulation results are consistent with previous observation results showing

the larger CV for primary pollutants than for secondary pollutants (Vardoulakis et al., 2011; Matte et al., 2013), while their magnitudes of the CFD simulation results are larger than those of previous observation results (smaller than 1 even for primary pollutants).

8.5 Sensitivity simulations

From the discussion above, it is concluded that the heterogeneities of building geometry and mobile emission strongly affect not only the spatial variability of air quality but also the representative air quality. To quantify the impacts of heterogeneities, three additional CFD simulations (i.e., the ROAD+GRD, LYR+BLD, and LYR+GRD simulations) are performed, which are combinations of two different experimental setups: ROAD/LYR and BLD/GRD. Here, the simulations with the homogeneous pollutant emission distributed in the layer from surfaces to z = 50 m are referred to as 'LYR'. The total pollutant emission in the layer over the entire 1.6 km × 1.6 km area is the same as the total pollutant emission on roads over the entire 1.6 km × 1.6 km area in the control CFD simulation (the ROAD+BLD simulation). The simulations with the topographical height data removing building height from the surface height data are referred to as 'GRD'.

The vertical profiles of time- and area-averaged NO_2, O_3, and O_x concentrations in four different CFD simulations are compared in Figure 8.12. Note that the concentrations are averaged over the 1.6 km x 1.6 km area to take the same pollutant emission into account in the analysis. While the NO_2 concentration decreases with height, the decreasing rate of NO_2 concentration with height is smaller near surfaces in the ROAD+BLD simulation than in the ROAD+GRD simulation. Therefore, the increasing rate of O_3 concentration with height is also smaller near surfaces in the ROAD+BLD simulation than in the ROAD+GRD simulation. In the presence of buildings, the NO_2 concentrations increase by 7.4 ppb (15%) and 4.1 ppb (15%) at z = 30 and 74 m, respectively, and the O_3 concentrations decrease by 5.9 ppb (21%) and 3.7 ppb (9%) at z = 30 and 74 m, respectively. It is noteworthy that the impact of building geometry on the O_x concentration is insignificant because O_x is independent of the NO titration of O_3. The comparison of vertical concentration profiles between the ROAD+BLD and ROAD+GRD simulations confirms that the heterogeneity of building geometry promotes the vertical transport of NO_x emitted on roads followed by the enhanced NO titration of O_3. The emitted pollutants in the LYR+BLD simulation are artificially well-mixed near surfaces by the experimental setup of pollutant emission. Therefore, the NO_2 concentration in the LYR+BLD simulation is higher by 5.2 ppb (11%) and 1.4 ppb (5%) at z = 30

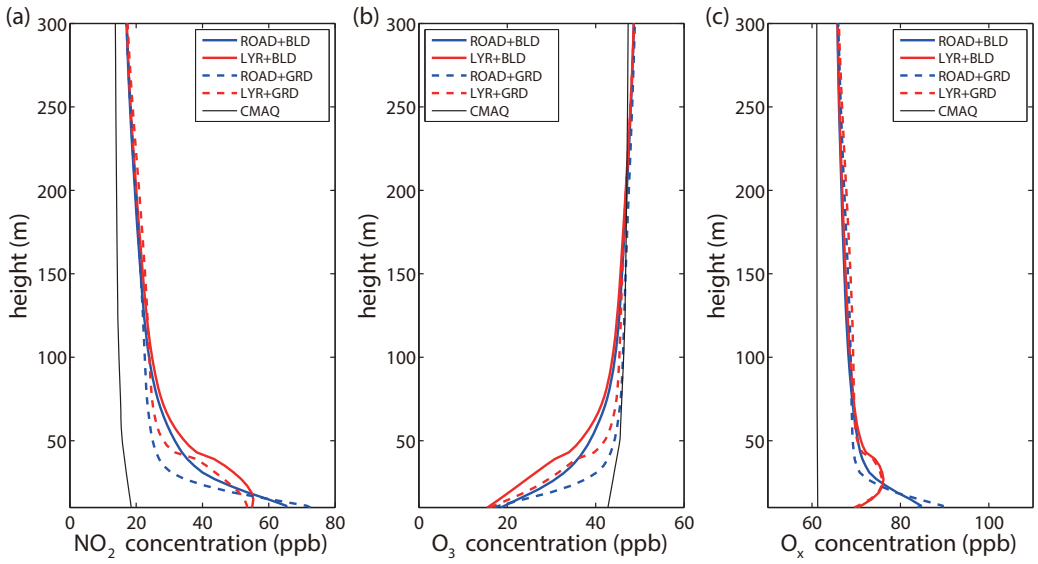

Figure 8.12. Vertical profiles of area- and time-averaged (a) NO_2, (b) O_3, and (c) O_x concentrations in the ROAD+BLD, LYR+BLD, ROAD+GRD, and LYR+GRD simulations. Vertical profiles of area averages over the 1.6 km × 1.6 km area and vertical profiles in the CMAQ simulation are averaged for 4 h from 1200 to 1600 LT.

and 74 m, respectively, than that in the ROAD+BLD simulation. As the NO titration of O_3 becomes efficient, the O_3 concentration in the LYR+BLD simulation is lower by 6.0 ppb (21%) and 1.0 ppb (2%) at z = 30 and 74 m, respectively, than that in the ROAD+BLD simulation. The comparison of vertical concentration profiles between the ROAD+BLD and LYR+BLD simulations confirms that the heterogeneity of mobile emission realistically distributed on roads confines the emitted pollutants near surfaces, resulting in the weakened NO titration of O_3.

The impacts of high-rise buildings and mobile emission are elaborated by the segregation effects (Auger and Legras, 2007; Zhong et al., 2014). In the previous studies, the segregation effects become significant as the pollutant mixing becomes less efficient, resulting in the higher O_3 concentration due to the weakened NO titration of O_3. In this study, the impacts of heterogeneities of building geometry and mobile emission on the vertical pollutant mixing and the NO titration of O_3 are compensated by each other. The NO_2 and O_3 concentration differences between the ROAD+BLD and LYR+GRD simulations are relatively small, which are 0.5 ppb (1%) and 1.6 ppb (6%), respectively, at z = 30 m. In addition, the impacts are less significant above the top height of high-rise buildings. The NO_2 and O_3 concentration differences at z = 162 m are at most 0.6 ppb (3%) and 0.7 ppb (2%), respectively.

9 Summary

Microscale (a horizontal scale smaller than about 3 km, a vertical scale smaller than a doubled building height, and a time scale shorter than about 1 hour) flow, gas-phase chemistry, and dispersion in urban areas are investigated by means of numerical modeling. This study covers the developments of a computational fluid dynamics (CFD) model with essential physical and chemical components and the understandings of flow, gas-phase chemistry, and dispersion in urban areas. Especially, urban street canyons were considered as basic geometries representing microscale morphologies.

A CFD model which includes an urban surface and radiation model was developed to investigate the diurnal variation of street canyon flow. The coupled model predicts surface and substrate temperatures of roof, walls, and road. When compared to field measurements in summertime, the coupled model well reproduces the diurnal variations of surface temperatures. Flows in a north-south oriented street canyon with $H/W = 1$ were investigated. Two flow regimes in a street canyon are identified by vortex configuration. Flow regime I characterized by a primary vortex appears for most of the day. Flow regime II characterized by two counter-rotating vortices appears when the downwind building wall is strongly heated in the morning. The street canyon flow alters canyon air

temperature field. The region of cool/warm air appears along the downwind/upwind building wall in flow regime I, whereas it appears in the region of the upper/lower vortex in flow regime II. The influence of the ambient wind speed on street canyon flow is different in the two flow regimes. The extent of the upper/lower vortex in flow regime II expands/shrinks with increasing ambient wind speed and changes the extent of the region of cool/warm air accordingly. On the other hand, the shape of the primary vortex in flow regime I is relatively invariant to the ambient wind speed. Different relationships between mean canyon wind speed and ambient wind speed were found in the two flow regimes. For weak ambient winds, the mean canyon wind speed is relatively small in flow regime II but relatively large in flow regime I. Following the dependency of turbulent kinetic energy on the ambient wind speed near the heated wall, the dependency of surface sensible heat flux on the ambient wind speed is high in flow regime II but low in flow regime I.

A CFD model that includes the carbon bond mechanism Ⅳ (CBM–Ⅳ) was developed and used to investigate the dispersion of reactive species in and above a street canyon with a canyon aspect ratio of 1. A total of 14 emission scenarios of NO_x (= NO + NO_2) and volatile organic compound (VOC) were analyzed. The model was validated against the field measurement data for NO_2 and NO_x concentrations, showing that the simulated concentrations are in good

agreement with the measured concentrations. Three dispersion types were identified: NO-type, NO_2-type, and O_3-type dispersion that exhibit concentration maxima at the street bottom, near the center of the street canyon, and above the street canyon, respectively. For the base emission scenario, the number of reactive species is 9 in the NO-type dispersion, 10 in the NO_2-type dispersion, and 15 in the O_3-type dispersion. The dispersion type of any species except for the NO-type dispersion was shown to be dependent on the NO_x and VOC emission levels. As the NO_x emission level increases, the concentrations of species in the NO_2-type and O_3-type dispersion generally become more reduced in the street canyon than above it. In contrast, as the VOC emission level increases, the concentrations of species in the NO_2-type and O_3-type dispersion generally become more increased in the street canyon than above it. As a consequence of these concentration changes in the street canyon, species in the O_3-type dispersion generally tends to be shifted to the NO_2-type dispersion when the VOC-to-NO_x emission ratio increases. It was found that the OH concentration increases as the VOC emission level increases but decreases as the NO_x emission level decreases, which means the OH concentration tends to increase with the VOC-to-NO_x emission ratio. In this way, OH plays a key role in controlling the dispersion type of reactive species through the radical chain including HO_2, RO, and RO_2. Among the VOCs involved in this process, XYL

and OLE are responsible for more than a half of the OH + RH reaction because of their high OH reactivities. Because the NO-to-NO_2 ratio is high in the street canyon, the O_3 sensitivity to the NO_x and VOC emissions in the street canyon differs from that for broad-scale urban areas where the NO-to-NO_2 ratio is relatively low. The high NO-to-NO_2 ratio in the street canyon makes the NO titration of O_3 be more pronounced than the NO_2 photolysis. In the street canyon, the O_3 concentration is negatively correlated with the NO_x emission level but weakly correlated with the VOC emission level. Therefore, in contrast with the general finding that an urban area is generally a VOC-sensitive regime, the street canyon is a negatively NO_x-sensitive regime.

A CFD model coupled with the CBM–Ⅳ was used to investigate the reactive pollutant dispersion in urban street canyon with canyon aspect ratios of 1 and 2. Various environmental conditions are considered to examine the sensitivities of the O_3 chemical characteristics. O_3 dispersion shows the distinct separation between the lower and upper regions of the $H/W = 2$ street canyon. O_3 is shown to be chemically produced in the upper region of the street canyon, whereas O_3 chemical depletion is pronounced in the lower region of the street canyon. Other reactive pollutants such as NO, NO_2, TOL, XYL, and OH also show differences in chemical characteristics between the lower and upper regions of the street canyon. Additional simulations for the sensitivity of O_3

chemical characteristics to environmental conditions such as NO_x and VOC emission rates, photolysis rate, and ambient wind speed are performed. The results show increasing O_3 concentration with decreasing NO_x emission rate and increasing VOC emission rate and photolysis rate. O_3 chemical production is favored when NO_x emission rate is low and VOC emission rate and photolysis rate are high. The effect of ambient wind speed on O_3 concentration appears within a few ppb.

The CFD model coupled with the urban surface and radiation model and the CBM–Ⅳ is used to investigate the diurnal variation of NO_x and O_3 exchange between a street canyon and the overlying air. Flow regime I and II appear in the presence of upwind building wall heating in the afternoon and in the presence of downwind building wall heating in the morning, respectively. Both mean and turbulent processes of NO_x removal and O_3 entrainment are active in the vicinity of the downwind building wall in flow regime II. In flow regime I, the mean process is broadly active in the upwind building side, whereas the turbulent process is active in the vicinity of the upwind building wall. In the diurnal variation of NO_x and O_3 exchange, the turbulent process is the dominant mechanism. However, the mean process can be responsible for more than a half of NO_x removal and O_3 entrainment at about 1500 LST in flow regime I. The NO_x and O_3 exchange velocities were individually estimated. The NO_x and O_3

exchange velocities are similar to each other in the early morning. However, the O_3 exchange velocity is significantly lower than the NO_x exchange velocity around noon and in the afternoon. The larger diurnal variation of O_3 exchange velocity than that of NO_x exchange velocity indicates the dependency of exchange velocity on photochemistry as well as flow in the street canyon. The estimation of exchange velocity for reactive pollutants provides us a basis for quantifying the exchange process regardless of dry deposition process.

Urban air quality simulation is performed using the CFD model coupled with mesoscale meteorological (WRF) and chemistry-transport (CMAQ) models. One-way coupling of WRF and CMAQ models to the CFD model is introduced as a comprehensive tool for microscale air quality study. As initial and time-varying boundary conditions, wind speed and direction, air temperature, turbulent kinetic energy, pollutant concentrations, photolysis rates, and mobile emission rates are interpolated in time and height into the CFD model domain in the microscale simulation. A high-rise building area of Seoul, Republic of Korea, is selected for simulating flow and reactive pollutant dispersion. The NO_2 and O_3 dispersion shows the strong influences of building geometry and mobile emission. The emitted NO_2 can rapidly be transported up to the rooftop of high-rise buildings, which can contribute the local heterogeneity of pollutants. The local contributions are shown to be large near the surface by calculating the

coefficient of variation in NO_2 and O_3 concentrations. The sensitivity simulations without building geometry and/or with homogenous pollutant emission in a layer are performed to quantify the impacts of local influences on the representative urban air quality. The heterogeneity of building geometry enhances the vertical pollutant transport, while the emission distribution on roads confines the emitted pollutants near surfaces. As a result, the O_3 concentration is oppositely affected by the heterogeneities of building geometry and mobile emission through the NO titration of O_3. It is concluded that the integrated urban air quality modeling system realistically simulates the spatial variability due to the local influences of building geometry and mobile emission.

References

Aikawa, M., T. Hiraki, and M. Tamaki, 2005. Estimation of the amount of dry deposition in an urban area (Kobe city, Japan) by the inferential method. *Environ. Chem. Let.,* **3**, 62–65.

Allwine, K.J., M.J. Leach, L.W. Stockham, J.S. Shinn, R.P. Hosker, J.F. Bowers, and J.C. Pace, 2004: Overview of Joint urban 2003 – an atmospheric dispersion study in Oklahoma City. In: Proceedings of the AMS symposium on planning, nowcasting, and forecasting in the urban zone, January 11–15, Seattle, Washington, USA.

Arnold, S.J., H. ApSimon, J. Barlow, S. Belcher, M. Bell, J.W. Boddy, R. Britter, H. Cheng, R. Clark, R.N. Colvile, S. Dimitroulopoulou, A. Dobre, B. Greally, S. Kaur, A. Knights, T. Lawton, A. Makepeace, D. Martin, M. Neophytou, S. Neville, M. Nieuwenhuijsen, G. Nickless, C. Price, A. Robins, D. Shallcross, P. Simmonds, R.J. Smalley, J. Tate, A.S. Tomlin, H. Wang, and P. Walsh, 2004: Introduction to the DAPPLE air pollution project. *Sci. Total Environ.*, **332**, 139–153.

Auger, L., B. Legras, 2007: Chemical segregation by heterogeneous emissions. *Atmos. Environ.*, **41**, 2303–2318.

Baik, J.-J., Y.-S. Kang, and J.-J. Kim, 2007: Modeling reactive pollutant dispersion in an urban street canyon. *Atmos. Environ.*, **41**, 934–949.

Baik, J.-J., and J.-J. Kim, 1999: A numerical study of flow and pollutant dispersion characteristics in urban street canyons. *J. Appl. Meteor*., **38**, 1576–1589.

Baik, J.-J., and J.J. Kim, 2002: On the escape of pollutants from urban street canyons. *Atmos. Environ*., **36**, 527–536.

Baik, J.-J., S.-B. Park, and J.-J. Kim, 2009: Urban flow and dispersion simulation using a CFD model coupled to a mesoscale model. *J. Appl. Meteor. Climatol*., **48**, 1667-1681.

Baker, J., H.L. Walker, and X. Cai, 2004: A study of the dispersion and transport of reactive pollutants in and above street canyons – a large eddy simulation. *Atmos. Environ.*, **38**, 6883–6892.

Barlow, J.F., and S.E. Belcher, 2002. A wind tunnel model for quantifying fluxes in the urban boundary layer. *Bound.-Lay. Meteorol*., **104**, 131–150.

Barlow, J.F., I.N. Harman, and S.E. Belcher, 2004. Scalar fluxes from urban street canyons. Part I: laboratory simulation. *Bound.-Lay. Meteorol*., **113**, 369–385.

Bentham, T., and R. Britter, 2003. Spatially averaged flow within obstacle arrays. *Atmos. Environ.*, **37**, 2037–2043.

Bossioli, E., M. Tombrou, and C. Pilinis, 2002: Adapting the speciation of the VOCs emission inventory in the greater Athens area. *Water, Air, and Soil Pollut.: Focus 2*, 141–153.

Byun, D., and K.L. Schere, 2006: Review of the governing equations, computational algorithms, and other components of the models-3 Community Multiscale Air Quality (CMAQ) modeling system. *Appl. Mech. Rev.*, **59**, 51–77.

Cai, X.-M., J.F. Barlow, and S.E. Belcher, 2008: Dispersion and transfer of passive scalars in and above street canyons—Large-eddy simulations. *Atmos. Environ.*, **42**, 5885–5895.

Cai, X., 2012. Effects of differential wall heating in street canyons on dispersion and ventilation characteristics of a passive scalar. *Atmos. Environ.*, **51**, 268–277.

Carpentieri, M., P. Hayden, and A.G. Robins, 2012: Wind tunnel measurements of pollutant turbulent fluxes in urban intersections. *Atmos. Environ.*, **46**, 669–674.

Carter, W.P.L, 1996: Condensed atmospheric photooxidation mechanisms for isoprene. *Atmos. Environ.*, **30**, 4275–4290.

Carter, W.P.L., 2000. Documentation of the SAPRC-99 chemical mechanism for VOC reactivity assessment. Final Report to California Air Resources Board,

Contract No. 92–329 and 95–308.

Chan, T.L., G. Dong, C.S. Cheung, C.W. Leung, C.P. Wong, and W.T. Hung, 2001: Monte Carlo simulation of nitrogen oxides dispersion from a vehicular exhaust plume and its sensitivity studies. *Atmos. Environ.*, **35**, 6117–6127.

Chan, T.L., G. Dong, C.W. Leung, C.S. Cheung, and W.T. Hung, 2002: Validation of a two-dimensional pollutant dispersion model in an isolated street canyon. *Atmos. Environ.*, **36**, 861–872.

Chen, H., R. Ooka, K. Harayama, S. Kato, and X. Li 2004: Study on outdoor thermal environment of apartment block in Shenzhen, China with coupled simulation of convection, radiation and conduction: *Energy Build.*, **36**, 1247–1258.

Cheng, W.C., and C.-H. Liu, 2011. Large-eddy simulation of flow and pollutant transports in and above two-dimensional idealized street canyons. *Bound.-Lay. Meteorol.*, **139**, 411–437.

Cheng, W.C., C.-H. Liu, and D.Y.C. Leung, 2008: Computational formulation for the evaluation of street canon ventilation and pollutant removal performance. *Atmos. Environ.*, **42**, 9041–9051.

Cheng, W.C., C.-H. Liu, and D.Y.C. Leung, 2009: On the correlation of air and pollutant exchange for street canyons in combined wind-buoyancy-driven flow. *Atmos. Environ.*, **43**, 3682–3690.

Clements, A.L., Y. Jia, A. Denbleyker, E. McDonald-Buller, M.P. Fraser, D.T. Allen, D.R. Collins, E. Michel, J. Pudota, D. Sullivan, and Y. Zhu, 2009: Air pollutant concentrations near three Texas roadways, part Ⅱ: Chemical characterization and transformation of pollutants. *Atmos. Environ.*, **43**, 4523–4534.

Deguillaume, L., M. Beekmann, and C. Derognat, 2008: Uncertainty evaluation of ozone production and its sensitivity to emission changes over the Ile-de-France region during summer periods. *J. Geophys. Res.*, **113**, doi:10.1029/2007JD009081.

Doraiswamy, P., C. Hogrefe, W. Hao, R.F. Henry, K. Civerolo, J.-Y. Ku, G. Sistla, J.J. Schwab, and K.L. Demerjian, 2009: A diagnostic comparison of measured and model-predicted speciated VOC concentrations: *Atmos. Environ.*, **43**, 5759–5770.

Eliasson, I., B. Offerle, C.S.B. Grimmond, and S. Lindqvist, 2006: Wind fields and turbulence statistics in an urban street canyon. *Atmos. Environ.*, **40**, 1–16.

Flaherty, J.E., D. Stock, and B. Lamb, 2007: Computational fluid dynamics simulations of plume dispersion in urban Oklahoma City. *J. Appl. Meteor. Climatol*., **46**, 2110–2126.

Foley, K.M., S.J. Roselle, K.W. Appel, P.V. Bhave, J.E. Pleim, T.L. Otte, R. Mathur, G. Sarwar, J.O. Young, R.C. Gilliam, C.G. Nolte, J.T. Kelly, A.B. Gilliland, J.O. Bash, 2010: Incremental testing of the Community Multiscale Air Quality (CMAQ) modeling system version 4.7. *Geosci. Model Dev.*, **3**, 205–226.

Garmory, A., I.S. Kim, R.E. Britter, and E. Mastorakos, 2009: Simulations of the dispersion of reactive pollutants in a street canyon, considering different chemical mechanisms and micromixing. *Atmos. Environ*., **43**, 4670–4680.

Gery, M., G. Witten, J. Killus, and M. Dodge, 1989: A photochemical kinetics mechanism for urban and regional scale computer modeling. *J. Geophys. Res*., **94 (D10)**, 12925–12956.

Grawe, D., X.-M. Cai, and R.M. Harrison, 2007: Large eddy simulation of shading effects on NO_2 and O_3 concentrations within an idealized street canyon. *Atmos. Environ*., **41**, 7304–7314.

Grimmond, C.S.B., 2006: Progress in measuring and observing the urban atmosphere. *Theor*. *Appl*. *Climatol*., **84**, 3–22.

Grøntoft, T., and M.R. Raychaudhuri, 2004. Compilation of tables of surface

deposition velocities for O_3, NO_2 and SO_2 to a range of indoor surfaces. *Atmos. Environ.*, **38**, 533–544.

Guenther, A., T. Karl, P. Harley, C. Wiedinmyer, P.I. Palmer, and C. Geron, 2006: Estimates of global terrestrial isoprene emissions using MEGAN (Model of Emissions of Gases and Aerosols from Nature). *Atmos. Chem. Phys.*, **6**, 3181–3210.

Hadavand, M., M. Yaghoubi, and H. Emdad, 2008: Thermal analysis of vaulted roof. *Energy Build.*, **40**, 265–275.

Hanna, S.R., and E. Baja, 2009: A simple urban dispersion model tested with tracer data from Oklahoma City and Manhattan. *Atmos. Environ.*, **43**, 778–786.

Harman, I.N., and S.E. Belcher, 2006: The surface energy balance and boundary layer over urban street canyons. *Q. J. Roy. Meteor. Soc.*, **132**, 2749–2768.

Hertel, O., R. Berkowicz, and J. Christensen, 1993: Test of two numerical schemes for use in atmospheric transport-chemistry models. *Atmos. Environ.*, **27A**, 2591–2611.

Houyoux, M.R., J.M. Vukovich, C.J. Coats Jr., N.J.M. Wheeler, and P.S. Kasibhatla, 2000: Emission inventory development and processing for the Seasonal Model for Regional Air Quality (SMRAQ) project. *J. Geophys. Res.*, **105**, 9079–9090.

Huang, H., Y. Akutsu, M. Arai, and M. Tamura, 2000: A two-dimensional air quality model in an urban street canyon: evaluation and sensitivity analysis. *Atmos. Environ.*, **34**, 689–698.

Huang, Y., X. Hu, and N. Zeng, 2009: Impact of wedge-shaped roofs on airflow and pollutant dispersion inside urban street canyons. *Build. Environ.*, **44**, 2335–2347.

Idczak, M., D. Groleau, P. Mestayer, J.M. Rosant, and J.F. Sini, 2010: An application of the thermo-radiative model SOLENE for the evaluation of street canyon energy balance. *Build. Environ.*, **45**, 1262–1275.

Idczak, M., P. Mestayer, J.M. Rosant, J.F. Sini, and M.V. Violleau, 2007: Micrometeorological measurements in a street canyon during the joint ATREUS-PICADA experiment. *Bound.-Layer Meteor.*, **124**, 25–41.

Jacobson, M.Z., 2005: Fundamentals of atmospheric modeling. Cambridge, 2nd ed., 813pp.

Janjić, Z.I., 1994: The step-mountain eta coordinate model: further development of the convection, viscous sublayer, and turbulence closure schemes. *Mon. Weather Rev.*, **122**, 927–945.

Jenkin, M.E., and K.C. Clemitshaw, 2000: Ozone and other secondary photochemical pollutants: chemical processes governing their formation in the planetary boundary layer. *Atmos. Envion.*, **34**, 2499–2527.

Kang, Y.-S., J.-J. Baik, and J.-J. Kim, 2008: Further studies of flow and reactive pollutant dispersion in a street canyon with bottom heating. *Atmos. Environ.*, **42**, 4964–4975.

Kim, D.-Y., J.-J. Kim, J.-H. Oh, and P. Sen, 2008: A case study on emission management for reducing photochemical pollution over the Osaka bay area. *Asia-Pacific J. Atmos. Sci.*, **44(4)**, 341–349.

Kim, J.-J, and J.-J. Baik, 1999: A numerical study of thermal effects on flow and pollutant dispersion in urban street canyons. *J. Appl. Meteor.*, **38**, 1249–1261.

Kim, J.-J, and J.-J. Baik, 2001: Urban street-canyon flows with bottom heating. *Atmos. Environ.*, **35**, 3395–3404.

Kim, J.-J., and J.-J. Baik, 2004: A numerical study of the effects of ambient wind direction on flow and dispersion in urban street canyons using the RNG k–ε turbulence model. *Atmos. Environ.*, **38**, 3039–3048.

Kim, M.J., R.J. Park, and J.-J. Kim, 2012. Urban air quality modeling with full O_3–NO_x–VOC chemistry: implications for O_3 and PM air quality in a street canyon. *Atmos. Environ.*, **47**, 330–340.

Klein, P., B. Leitl, and M. Schatzmann, 2011: Concentration fluctuations in a downtown urban area. Part Ⅱ: analysis of Joint Urban 2003 wind-tunnel measurements. *Environ. Fluid Mech.*, **11**, 43–60.

Kovar-Panskus, A., L. Moulinneuf, E. Savory, A. Abdelqari, J.F. Sini, J.M. Rosant, A. Robins, N. Toy, 2002: A wind tunnel investigation of the influence of solar-induced wall-heating on the flow regime within a simulated urban street canyon. *Water Air Soil Pollut., Focus 2*, 555–571.

Kwak, K.-H., J.-J. Baik, S.-H. Lee, and Y.-H. Ryu, 2011: Computational fluid dynamics modelling of the diurnal variation of flow in a street canyon. *Bound.-Layer Meteor.*, **141**, 77–92.

Kwak, K.-H., and J.-J. Baik, 2012: A CFD modeling study of the impacts of NO_x and VOC emissions on reactive pollutant dispersion in and above a street canyon. *Atmos. Environ.*, **46**, 71–80.

Lee, S.-H., and S.-U. Park, 2008: A vegetated urban canopy model for meteorological and environmental modeling. *Bound.-Layer Meteor*., **126**, 73–102.

Lee, S.-H., C.-K. Song, J.-J. Baik, and S.-U. Park, 2009: Estimation of anthropogenic heat emission in the Gyeong-In region of Korea. *Theor. Appl. Climatol*., **96**, 291–303.

Lei, W., B. Foy, M. Zavala, R. Volkamer, and L.T. Molina, 2007: Characterizing ozone production in the Mexico City metropolitan area: a case study using a chemical transport model. *Atmos. Chem. Phys*., **7**, 1347–1366.

Li, X.-X., C.-H. Liu, D.Y.C. Leung, and K.M. Lam, 2006: Recent progress in CFD modeling of wind field and pollutant transport in street canyons. *Atmos. Environ.*, **40**, 5640–5658.

Li, X.-X., R.E. Britter, L.K. Norford, T.-Y. Koh, and D. Entekhabi, 2012: Flow and pollutant transport in urban street canyons of different aspect ratios with ground heating: Large-eddy simulation. *Bound.-Layer Meteor.*, **142**, 289–304.

Liu, C.-H., and M.C. Barth, 2002: Large-eddy simulation of flow and scalar transport in a modeled street canyon. *J. Appl. Meteor.,* **41**, 660–673.

Liu, C.-H., M.C. Barth, and D.Y.C. Leung, 2004: Large-eddy simulation of flow and pollutant transport in street canyons of different building-height-to-street-width ratios. *J. Appl. Meteor.*, **43**, 1410–1424.

Liu, C.-H., and D.Y.C. Leung, 2008: Numerical study on the ozone formation inside street canyons using a chemistry box model. *J. Environ. Sci.*, **20**, 832–837.

Liu, C.-H., D.Y.C. Leung, and M.C. Barth, 2005: On the prediction of air and pollutant exchange rates in street canyons of different aspect ratios using large-eddy simulation. *Atmos. Environ.*, **39**, 1567–1574.

Louka, P., G. Vachon, J.F. Sini, P.G. Mestayer, and J.M. Rosant, 2002: Thermal effects on the flow in a street canyon – Nantes'99 experimental results and model simulations. *Water Air Soil Pollut. Focus 2*, 351–364.

Martins, L.D., and M.F. Andrade, 2008: Ozone formation potentials of volatile organic compounds and ozone sensitivity to their emission in the megacity of São Paulo, Brazil. *Water Air Soil Pollut.*, **195**, 201–213.

Matte, T.D., Z. Ross, I. Kheirbek, H. Eisl, S. Johnson, J.E. Gorczynski, D. Kass, S. Markowitz, G. Pezeshki, and J.E. Clougherty, 2013: Monitoring intraurban spatial patterns of multiple combustion air pollutants in New York City: Design and implementation. *J. Expo. Sci. Environ. Epid.*, **23**, 223–231.

Mellor, G.L., T. Yamada, 1982: Development of a turbulence closure model for geophysical fluid problems. *Rev. Geophys. Space Phys.*, **20**, 851–875.

Moon, N., S. Kim, D.W. Byun, and Y. Joe, 2006: Air Quality Modeling System 1 – Development of Emissions Preparation System with the CAPSS, KEP Rep. 2006-RE-11, Korea Environment Institute, Seoul, 95 pp..

Nakamura, Y., and T.R. Oke, 1988: Wind, temperature and stability conditions in an east-west oriented urban canyon. *Atmos. Environ.*, **22**, 2691–2700.

Offerle, B., I. Eliasson, C.S.B. Grimmond, and B. Holmer, 2007: Surface heating in relation to air temperature, wind and turbulence in an urban street canyon. *Bound.-Layer Meteor*., **122**, 273–292.

Oke, T.R., 1988: Street design and urban canopy layer climate. *Energy Build*., **11**, 103–113.

Panão, M.J.N., H.J.P. Gonçalves, and P.M.C. Ferrão, 2007: A matrix approach coupled with Monte Carlo Techniques for solving the net radiative balance of the urban block. *Bound.-Layer Meteor*., **122**, 217–241.

Peng, Y.P., K.S. Chen, C.H. Lai, P.J. Lu, and J.H. Kao, 2006: Concentrations of H_2O_2 and HNO_3 and O_3–VOC–NO_x sensitivity in ambient air in southern Taiwan. *Atmos. Environ*., **40**, 6741–6751.

Pugh, T.A.M., A.R. MacKenzie, J.D. Whyatt, and C.N. Hewitt, 2012. Effectiveness of green infrastructure for improvement of air quality in urban street canyons. *Environ. Sci. Technol.*, **46**, 7692–7699.

Ryu, Y.-H., J.-J. Baik, and S.-H. Lee, 2011: A new single-layer urban canopy model for use in mesoscale atmospheric models. *J. Appl. Meteor. Climatol*., **50**, 1773–1794.

Ryu, Y.-H., J.-J. Baik, K.-H. Kwak, S. Kim, and N. Moon, 2012: Impacts of urban land-surface forcing on air quality in the Seoul metropolitan area. *Atmos. Chem. Phys. Discuss.*, **12**, 25791–25832.

Ryu, Y.-H., J.-J. Baik, K.-H. Kwak, S. Kim, and N. Moon, 2013: Impacts of urban land-surface forcing on ozone air quality in the Seoul metropolitan area. *Atmos. Chem. Phys.*, **13**, 2177–2194.

Santamouris, M., N. Papanikolaou, I. Koronakis, I. Livada, and D. Asimakopoulos, 1999: Thermal and air flow characteristics in a deep pedestrian canyon under hot weather conditions. *Atmos. Environ.*, **33**, 4503–4521.

Shon, Z.-H., K.-H. Kim, and S.-K. Song, 2011: Long-term trend in NO_2 and NO_x levels and their emission ratio in relation to road traffic activities in East Asia. *Atmos. Environ.*, **45**, 3120–3131.

Sillman, S., 1999: The relation between ozone, NO_x and hydrocarbons in urban and polluted rural environments. *Atmos. Environ.*, **33**, 1821–1845.

Sillman, S., and J.J. West, 2009: Reactive nitrogen in Mexico City and its relation to ozone-precursor sensitivity: results from photochemical models. *Atmos. Chem. Phys.*, **9**, 3477–3489.

Sini, J.F., S. Anquetin, and P.G. Mestayer, 1996: Pollutant dispersion and thermal effects in urban street canyons. *Atmos. Environ.*, **30**, 2659–2677.

Skamarock, W.C., J.B. Klemp, J. Dudhia, D.O. Gill, D.M. Barker, M.G. Duda, X.-Y. Huang, W. Wang, and J.G. Powers, 2008. A description of advanced research WRF version 3. NCAR Technical Note NCAR/TN–475+STR.

Smylie, M., J.L. Fieber, T.C. Myers, and S. Burton, 1991: A preliminary examination of the impact on emissions and ozone air quality in Athens, Greece from various hypothetical motor vehicle control strategies. European Conference on New Fuels and Clean Air, 19 June 1991, Antwerp, Belgium.

Solazzo, E., and R.E. Britter, 2007. Transfer processes in a simulated urban street canyon. *Bound.-Lay. Meteorol.*, **124**, 43–60.

Song, J., W. Lei, N. Bei, M. Zavala, B. Foy, R. Volkamer, B. Cardenas, J. Zheng, R. Zhang, and L.T. Molina, 2010: Ozone response to emission changes: a modeling study during the MCMA-2006/MILAGRO campaign. *Atmos. Chem. Phys.*, **10**, 3827–3846.

Swinbank, W.C., 1963: Long-wave radiation from clear skies. *Q. J. Roy. Meteor. Soc.*, **89**, 339–348.

Tsai, M.Y., K.S. Chen, and C.H. Wu, 2005: Three-dimensional modeling of air flow and pollutant dispersion in an urban street canyon with thermal effects. *J. Air Waste Manag. Assoc.*, **55**, 1178–1189.

Uehara, K., S. Murakami, S. Oikawa, and S. Wakanatsu, 2000: Wind tunnel experiments on how thermal stratification affects flow in and above urban street canyons. *Atmos. Environ.*, **34**, 1553–1562.

Vardoulakis, S., B.E.A. Fisher, K. Pericleous, and N. Gonzalez-Flesca, 2003: Modelling air quality in street canyons: a review. *Atmos. Environ.*, **37**, 155–182.

Vardoulakis, S., E. Solazzo, and J. Lumbreras, 2011: Intra-urban and street scale variability of BTEX, NO_2, and O_3 in Birmingham, UK: Implications for exposure assessment. *Atmos. Environ.*, **45**, 5069–5078.

Versteeg, H.K., and W. Malalasekera, 1995: An introduction to computational fluid dynamics: The finite volume method. Longman, Malaysia, 272 pp.

Wang, Y.J., A. DenBleyker, E. McDonald-Buller, D. Allen, and K.M. Zhang, 2011: Modeling the chemical evolution of nitrogen oxides near roadways. *Atmos. Environ.*, **45**, 43–52.

Xie, X., Z. Huang, J. Wang, and Z. Xie, 2005: The impact of solar radiation and street layout on pollutant dispersion in street canyon. *Build. Environ.*, **40**, 201–212.

Xie, X., C.-H. Liu, and D.Y.C. Leung, 2007: Impact of building facades and ground heating on wind flow and pollutant transport in street canyons. *Atmos. Environ.*, **41**, 9030–9049.

Xie, Z.-T., and I.P. Castro, 2009: Large-eddy simulation for flow and dispersion in urban streets. *Atmos. Environ.*, **43**, 2174–2185.

Yassin, M.F., R. Kellnerová, and Z. Jaňour, 2008: Impact of street intersections

on air quality in an urban environment. *Atmos. Environ*., **42**, 4948–4963.

Zavala, M., W. Lei, M.J. Molina, and L.T. Molina, 2009: Modeled and observed ozone sensitivity to mobile-source emissions in Mexico City. *Atmos. Chem. Phys*., **9**, 39–55.

Zhong, J., X.-M. Cai, W.J. Bloss, 2014: Modelling segregation effects of heterogeneous emissions on ozone levels in idealised urban street canyons: Using photochemical box models. *Environ. Pollut.*, **188**, 132–143.

Zhu, Y., J. Pudota, D. Collins, D. Allen, A. Clements, A. DenBleyker, M. Fraser, Y. Jia, E. McDonald-Buller, and E. Michel, 2009: Air pollutant concentrations near three Texas roadways, Part Ⅰ: Ultrafine particles. *Atmos. Environ*., **43**, 4513–4522.

초 록

도시 지역의 흐름, 기체상 화학 및 분산은 주로 미규모이며, 지표상 인공적인 구조와 피복 상태에 따라 달라진다. 이러한 현상들은 서로 영향을 주고 받는 관계에 있기 때문에 하나의 체계 안에서 연구되어야 한다. 본 연구는 핵심적인 물리 및 화학 요소를 결합한 계산 유체 역학 모형을 개발하였다. 첫째로, 도시 지표 및 복사 모형을 계산 유체 역학 모형에 접목시켜 외관비가 1 인 도로 협곡 내 흐름의 일변화를 연구하였다. 만 하루를 대상으로 다양한 주변 풍속을 고려한 실험에서 도로 협곡 내 소용돌이 형태에 따라 두 가지 흐름 영역이 정의되었다. 흐름 영역 I 과 II 는 각각 하나의 주요 소용돌이와 두 개의 마주 도는 소용돌이로 특징지어 진다. 주변 바람이 약한 경우, 지표 현열속의 주변 풍속에 대한 의존성이 협곡 풍속과 주변 풍속 간 관계를 결정짓는 데 주요한 역할을 하는 것으로 밝혀졌다. 둘째로, 탄소 결합 메커니즘(CBM-Ⅳ)을 계산 유체 역학 모형에 접목시켜 외관비가 1 인 도로 협곡 내부와 외부의 반응성 오염 물질 분산을 연구하였다. 14 가지의 배출 시나리오에 대한 실험에서 오염 물질의 분산 유형은 NO 형 분산, NO_2 형 분산, O_3 형 분산으로 분류되었다. OH 가 HO_2, RO,

RO_2를 포함하는 라디칼 사슬(radical chain)을 통해 분산 유형의 전이 과정에서 주요 역할을 하면서, VOC 와 NO_x 의 배출비가 분산 유형의 전이를 결정하는 주요 요인으로 밝혀졌다. O_3 민감도 조사에서 O_3 농도는 NO_x 배출 정도와 음의 상관 관계를 보였으며, VOC 배출 정도와 약한 양의 상관 관계를 보였다. 따라서, 도로 협곡은 음의 NO_x 민감도 영역(negatively NO_x-sensitive regime)이다. 외관비가 2 인 도로 협곡에서는 O_3 이 화학적으로 생성되는 상부 영역과 O_3 이 화학적으로 소멸되는 하부 영역이 서로 대조를 이루었다. 셋째로, 도시 지표 및 복사 모형과 탄소 결합 메커니즘을 계산 유체 역학 모형에 함께 접목하여 도로 협곡과 그 위의 공기 사이에서 일어나는 NO_x 와 O_3 교환의 일변화를 연구하였다. 도로 협곡의 옥상 고도를 가로지르는 NO_x 제거(NO_x removal)와 O_3 유입(O_3 entrainment)의 시공간적 분포는 전적으로 흐름 영역에 의존하였다. 일반적으로 난류에 의한 NO_x 제거와 O_3 유입이 주요 메커니즘인 한편, 풍상측 건물 벽이 강하게 가열되는 오후 시간대에는 평균류에 의한 NO_x 제거와 O_3 유입이 주요하였다. 계산된 NO_x 와 O_3 교환 속도는 흐름 영역뿐만 아니라 광화학에도 의존하였다. 마지막으로, 중규모 기상 모형(WRF 모형)과 화학 수송 모형(CMAQ 모형)을 결합한 계산 유체 역학 모형(통합 도시 대기질 모델링 시스템)을

이용하여 고층 건물 밀집 지역에 대한 도시 대기질 모의를 수행하였다. 모의된 NO_2와 O_3 농도를 도로변 대기질 측정소에서 측정된 자료에 대해 평가해본 결과, CMAQ 모의 값과 비교하여 현저한 개선을 보였다. 고층 건물 밀집 지역에서 NO_2와 O_3 농도의 큰 공간 변동성은 건물 구조와 자동차 오염물질 배출의 불균질성에 기인하였다. 결론적으로, 통합 도시 대기질 모델링 시스템은 도시 지역의 대기질에 미치는 다중규모 영향을 아우르는 독보적인 기법이다.

주요어: 반응성 오염 물질 분산, NO_x−VOC−O_3 화학, 계산 유체 역학 모형, 도시 지역, 도로 협곡, 오염 물질 배출

학번: 2007−20376